UNIVERSITY OF READING

Department of Meteorology

Surface Effects in Quasi-Geostrophic Dynamics

BENJAMIN J HARVEY

A thesis submitted for the degree of Doctor of Philosophy

March 2011

DECLARATION

I confirm that this is my own work and the use of all material from other sources has been properly and fully acknowledged.

Ben Harvey

ABSTRACT

The topic of this thesis is the wave dynamics of surface quasi-geostrophic (surface QG) flows. The surface QG equation set is a simple model of large-scale atmospheric and oceanic flows near horizontal boundaries such as low-level atmospheric weather systems, upper-ocean currents and also undulations of the tropopause. Recent renewed interest in the model has been prompted by the realisation that it is consistent with several previously unexplained phenomena such as the observed energy spectra of atmospheric motions near the tropopause, as well as the dynamical structure of upper ocean eddies.

The approach taken here is to study the system from a theoretical viewpoint in order to understand some of the general observed and simulated features of the dynamics. As well as this analytic study a numerical code is used to verify and illustrate the theoretical results.

There are three main directions of research. One is to understand a peculiar feature of surface QG simulations - not exhibited by other simple atmospheric models - whereby small scale instabilities very readily develop on filamentary vorticity structures. This instability is in fact a common feature of satellite water vapour imagery which, in the extra-tropics, often shows high potential vorticity stratospheric intrusions (i.e., tropopause undulations) 'rolling-up' into upper-air mesoscale vortices. The linear dynamics of this instability is investigated with some remarkable results, such as the scaling behaviour of the vortices formed. Another part of the work has been to study the behaviour and stability of vortices in the surface QG system (such as those formed as a result of the filament instability). This, again, has taken the form of an analytic study backed-up by numerical results. Together with the first study, the results provide a fairly comprehensive picture of various features of surface-enhanced flows as well as abstract surface QG turbulence simulations.

In the final chapter of the thesis we move away from pure surface QG dynamics to apply the theory developed for the study of surface QG vortices to a new simple analytic model of atmospheric baroclinic instability. Unlike previous similar models, this model has the advantage that the non-linear development of the instability is quite realistic and, further, appears to exhibit both major types of wave breaking commonly observed in the atmosphere. The linear theory is fully developed and the results of some numerical integrations presented.

ACKNOWLEDGEMENTS

I would like to thank Maarten Ambaum for his encouragement and supervision throughout the course of this project. His input of ideas and corrections, as well as his continued willingness to give his time, are greatly appreciated. I would also like to thank all members of the Dynamical Processes group, whose discussions over the past three years have been invaluable.

Thanks to my friends and office mates for making my time in Reading an enjoyable one, and also my family for their interest and support. I am especially grateful to Natalie for her unending patience and encouragement.

Finally, I would like to thank my examiners, David Dritschel and John Methven for reading my thesis and giving me very helpful feedback and the Natural Environment Research Council for funding this project.

Contents

Chapter 1:

INTRODUCTION

1.1 General introduction and a brief description of the thesis

The theory of quasi-geostrophic (QG) dynamics (see Pedlosky (1987), Holton (2004) or Vallis (2006)) has been used extensively in mid-latitude meteorology and oceanography for over half a century (Charney, 1948). Its appeal lies in the fact that it has both broad theoretical and practical applications. Despite its wide use, however, there is one aspect which perhaps does not receive enough interest in the literature and that is the influence of horizontal boundaries on the dynamics. The main aim of this thesis is to better understand the effects that such horizontal boundaries have on the quasi-geostrophic dynamics of the atmosphere and oceans. We approach the problem using the so-called surface quasi-geostrophic (surface QG) equation set.

That horizontal boundaries play an important role in geophysical fluid systems is so prominent it barely needs mentioning. Taking the lower boundary of the atmosphere as an example, dominant factors include frictional effects as well as fluxes of heat, water and other atmospheric constituents. The upper surface of the ocean, on the other hand, affects the large-scale dynamics through wind stresses and salinity fluxes. The most important factor in both systems, from a synoptic-scale, quasi-geostrophic dynamics point of view, however, is the inhibition of vertical motion.

Day-to-day experience in an extra-tropical location gives conspicuous illustrations of this: atmospheric weather fronts. Fronts (by which we just mean regions of strong horizontal temperature gradient) form preferentially at the surface in the atmosphere and this is because of the inhibition of vertical motion there. To understand this, consider the thought experiment illustrated by Figure 1. Panel (a) shows a cross section of a smooth baroclinic zone where the surface is cold on the left and warmer on the right.

Panel (b) shows the situation after a large-scale deformation is applied that thins the frontal region. Horizontal temperature gradients in any fluid are typically sharpened by the presence of large-scale horizontal deformation fields, simply because any such flow pushes regions of different temperature together. This process occurs throughout the depth of the atmosphere; however, away from the surface vertical motions usually occur that to some extent oppose the sharpening of the temperature gradient. The vertical acceleration of air parcels is caused by buoyancy forces, or put more simply, the air parcels simply rise or fall to follow the isentropic surfaces. In contrast, near to the surface vertical motions are inhibited by the rigid boundary and this process cannot occur. Instead, the regions of differing temperature are pushed closer and closer together.

Under the approximations of quasi-geostrophic theory, which are discussed later, a simple analytic result can be obtained to illustrate this point. The calculation was first performed by Williams & Plotkin (1968) and it involves solving for the steady-state long-time limit case illustrated by panel (b). The solution indeed exhibits an interior vertical velocity which acts to keep the interior temperature profile smooth, whilst the temperature at the surface exhibits a discontinuity. The geostrophic velocity field has a low level jet in the vicinity of the temperature discontinuity, which is in fact logarithmically singular. Fronts in real fluids of course do not have this velocity singularity due to the presence of viscous and boundary layer processes. The grey arrow in panel (b) indicates the presence of an ageostrophic component of the horizontal velocity field around the front location, as there must be to close the circulation in the vertical plane (and, via the

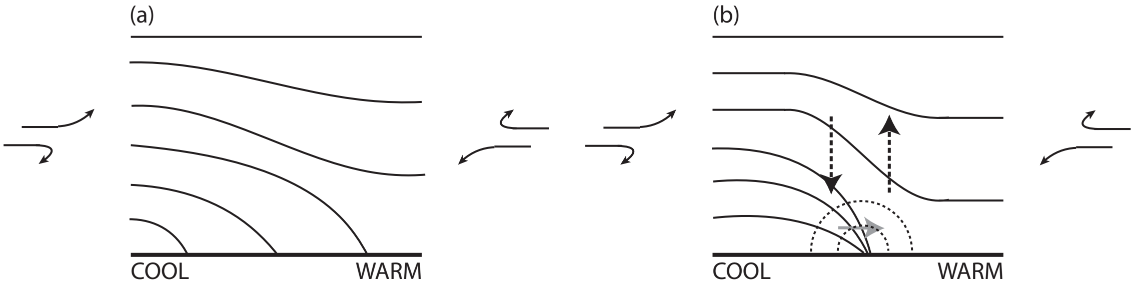

Figure 1.1 A sketch illustrating the effect of straining on a baroclinic region. The lines represent isentropic surfaces. Panel (a) shows an initial setup with a smooth temperature distribution and panel (b) shows the situation after some time. The isentropes are steepened by the straining everywhere, but away from the surface the ageostrophic vertical circulation (represented by the black arrows) opposes this tendency. The semicircles represent the along-front geostrophic flow and the grey arrow indicates the ageostrophic horizontal velocity near the surface.

Coriolis force, accelerate fluid parcels which converge into the low level jet). Under the quasi-geostrophic assumptions of this solution, however, the horizontal ageostrophic velocity component is fairly benign in that it does not advect the temperature field: it is assumed to be much smaller than the geostrophic velocity components and therefore not important.

This analysis can be improved by including the additional ageostrophic advection term, which must be important close to the location of the front because the geostrophic meridional velocity vanishes there. The result is the so-called semi-geostrophic equations which have been used extensively to analyse the formation of fronts under strain in the literature (see the review by Hoskins (1982)). As suggested by Figure 1.1, this extra advection component is in fact directed so as to accelerate the rate of the gradient increase, so much so that a front forms in finite time, rather then in the long-time limit of the pure QG case. In this thesis we only consider the less accurate, but more mathematically tractable, pure QG equations which neglect the additional ageostrophic advection terms. The question of whether it is possible for fronts to form in finite time in the pure QG case is still an open question and will be discussed further below (see, e.g., Constantin et al. (1998)).

This discussion points towards the fact that the inhibition of vertical motion at boundaries in rotating stratified fluids is closely related to the presence of temperature (or density in the ocean) gradients along the boundaries and vice versa. In fact, as far as quasi-geostrophic theory is concerned the two are directly related. This is most clearly seen from the quasi-geostrophic potential vorticity viewpoint (introduced fully in Section 1.2). In that set-up the dynamics split neatly into two components, an interior potential vorticity component and a surface temperature component (Bretherton, 1966a). The surface QG equations, which are the subject of the majority of this thesis, result from taking just the surface component in isolation of the interior component. That is, they model the dynamics of surface temperature features in the absence of any interior potential vorticity anomalies.

This surface component of QG dynamics is important from a theoretical point of view, not least because the formation of temperature fronts is a mechanism by which energy can be transferred to small scales in the atmosphere. Charney (1971) showed that the QG equations exhibit an energy cascade to large scales when there are no horizontal boundaries present, or when the temperature is uniform on all boundaries which are present. Down scale energy transfers do occur, however, when there are temperature variations on the boundaries, as described in detail by Blumen (1978). This is precisely because of the energy (both kinetic and available potential) associated with sloping isentropes near the regions of strong surface temperature gradients (see Figure 1.1 again). More recently, arguments have been made (Tulloch & Smith, 2006) that suggest this energy cascade is in fact the dominant energy transfer process in the upper troposphere on scales in the range 10-500 km, giving an explanation for the shallowing of the observed atmospheric energy spectrum in that range (Nastrom & Gage, 1985).

Application of the surface QG equations has been made, with varying degrees of success, directly to each of the three boundaries mentioned above: the lower boundary of the atmosphere, the tropopause and the upper surface of the ocean. It is for this reason, the ubiquity of the key ingredients of surface QG theory in geophysical fluid systems, tied together with a growing interest in the topic generally in the community that this thesis has been written.

There are three main problems that we tackle. The first, presented in Chapter 2, is to understand the behaviour of vortices in surface QG dynamics. Vortices which form in this system correspond to regions of anomalous surface temperature and are often called 'surface enhanced' vortices, since the velocity field is strongest near the surface and decays with height. Vortices commonly form in all of the physical situations to which surface QG dynamics has been applied, so an understanding of their behaviour is of strong interest. We approach the problem analytically using vortices with piecewise constant temperature profiles. There are two main reasons for doing this; it allows for the first time an analytic treatment of the problem of surface QG vortex stability and it also provides an insight into the dynamics of waves at temperature discontinuities, a subtle feature of surface QG dynamics that is interesting in its own right. It also allows a direct comparison to previous studies of vortices in the more familiar 2-d Euler equations.

The second, presented in Chapter 3, concerns the most striking feature of numerical surface QG simulations: the instability of small scale temperature filaments. As with other two-dimensional fluid models, filamentary structures regularly form as a result of vortex stripping-like behaviour (Legras & Dritschel, 1993). Unlike most other two-dimensional fluid flows, however, filaments in the surface QG model have a very strong tendency to become unstable and 'roll-up' into smaller scale vortices (see Section 1.3.4 as well as Pierrehumbert et al. (1994) and Held et al. (1995)). We study this problem in detail and present a new conceptual model of the instability process, explaining why the surface QG model shows this roll-up of filaments.

Finally, we consider the simplest extension to the surface QG model that allows baroclinic instability to occur. The extended model, which is governed by the temperature distributions on two horizontal boundaries representing the surface and tropopause respectively, is the subject of Chapter 4. As a corollary to the work of Chapter 2 we develop a new analytic model of baroclinic instability, similar in many ways to the well-known Eady model but with several interesting modifications. The model consists of temperature jumps at the bounding surfaces, rather than the uniform gradient in the Eady model, and it is also posed in circular symmetry which allows both the removal of the Eady model constraint whereby the upper and lower surfaces are symmetric and also the potential for more realistic nonlinear development.

Since the surface QG equations are not widely familiar, we use most of this Introduction to review some background theory. The purpose of this is to motivate the key scientific questions posed in Section 1.4. The equations are derived in Section 1.2 starting from a standard form for quasi-geostrophic theory and Section 1.3 then introduces some basic results from the literature.

1.2 Quasi-geostrophic dynamics and the surface QG model

We start from the standard form of the quasi-geostrophic potential vorticity equation for anelastic f-plane dynamics in height coordinates:

$$q = f + \nabla_h^2 \psi + \frac{f^2}{\rho_0(z)} \frac{\partial}{\partial z} \left(\frac{\rho_0(z)}{N^2(z)} \frac{\partial \psi}{\partial z} \right). \tag{1.1}$$

The reader is directed to one of several text books for a derivation of quasi-geostrophic theory, in particular: Pedlosky (1987), Holton (2004) or Vallis (2006). Following convention, we call q the quasi-geostrophic potential vorticity (QGPV) although as pointed out by Hoskins et al. (1985) amongst others, a more accurate title would be the ‘quasi-geostrophic pseudo–potential vorticity’ since it is not directly related to the Ertel potential vorticity. Rather, it is a modified version of it which is conserved under adiabatic and frictionless QG conditions following the geostrophic wind. That is,

$$\frac{Dq}{Dt} \equiv \left(\frac{\partial}{\partial t} + \mathbf{u}_g \cdot \nabla \right) q = 0. \tag{1.2}$$

The symbols in (1.1) and (1.2) have standards definitions: f is the component of the planetary vorticity which is locally vertical (we take this to be a constant), $\rho_0(z)$ and $N(z)$ represent reference state density and buoyancy frequency profiles about which the equations have been linearised and ψ represents the streamfunction which is related to the geostrophic wind via

$$(u_g, v_g) = \left(-\frac{\partial\psi}{\partial y}, \frac{\partial\psi}{\partial x}\right). \tag{1.3}$$

Note that we use D/Dt to denote the Lagrangian derivative following the geostrophic wind field.

The reference state density and buoyancy frequency profiles are taken to correspond to a stably stratified motionless atmosphere in hydrostatic balance and are therefore related to the pressure and potential temperature fields $p_0(z)$ and $\theta_0(z)$ via

$$\frac{\mathrm{d}p_0}{\mathrm{d}z} = -\rho_0 g \quad \text{and} \quad \frac{\mathrm{d}\theta_0}{\mathrm{d}z} = \frac{\theta_{00} N^2}{g} \tag{1.4}$$

where θ_{00} is a typical value of $\theta_0(z)$. The full fields are then written as

$$p = p_0(z) + p' \tag{1.5}$$

and

$$\theta = \theta_0(z) + \theta' \tag{1.6}$$

and the perturbation quantities are, under QG conditions, directly related to the streamfunction via geostrophic and hydrostatic balance respectively:

$$p' = \rho_0 f \psi \tag{1.7}$$

and

$$\theta' = \frac{\theta_{00} f}{g} \frac{\partial\psi}{\partial z}. \tag{1.8}$$

The QG conditions in question are precisely that these two equations approximately hold. Geostrophic balance requires a small Rossby number ($Ro = U/fL$) and hydrostatic balance requires a relatively strong stratification: the Froude number ($Fr = U/NH$) should be small even compared to $\sqrt{Ro}$.

Since we are considering a stably stratified reference state, $N^2(z)$ is positive and the right hand side of (1.1) is an elliptic operator on ψ. Given a distribution of q, then, the streamfunction can be calculated uniquely provided suitable boundary conditions are specified for ψ on all boundaries. Together with (1.2) we therefore have a closed system specified by one variable, the quasi-geostrophic potential vorticity.

Boundary conditions. At any rigid boundary the suitable condition is that the normal component of the velocity field vanishes. For vertical boundaries, that is, walls at the edges of the domain, this is equivalent to imposing that ψ be constant on the walls: vertical walls correspond to a Dirichlet type of boundary condition. An alternative to this is to use a doubly-periodic horizontal domain in which case no lateral boundary conditions are required.

For horizontal boundaries, such as the lower boundary of the atmosphere, the upper boundary of the ocean and also the upper boundary of the atmosphere if a rigid lid condition is imposed, the boundary condition is more subtle. This is because the vertical velocity is not locally related to the geostrophic wind (the two are only related globally via the omega equation) so there is no direct relationship between the normal velocity field and the streamfunction. However, a convenient condition on ψ which ensures that the boundary condition is satisfied can be obtained from the quasi-geostrophic thermodynamic equation:

$$\frac{D\theta'}{Dt} = -\frac{\theta_{00}N^2}{g}w. \tag{1.9}$$

This equation represents the adiabatic advection of the full potential temperature field in the atmosphere approximated to quasi-geostrophic accuracy: the wind field is replaced by its geostrophic component (D/Dt represents the geostrophic Lagrangian derivative as before) except where it multiplies a reference state quantity. This means the vertical advection of potential temperature is not negligible, instead it is accounted for by the term on the right hand side.

Equation (1.9) indicates that imposing the condition of zero vertical velocity at flat horizontal boundaries is equivalent to requiring θ' to be conserved by the geostrophic wind there. Recall from (1.8) that the potential temperature anomaly is proportional to the vertical derivative of ψ so that specifying the surface temperature field is equivalent to applying a Neumann boundary condition on the streamfunction and is therefore sufficient information to obtain a unique solution to (1.1) (apart from an irrelevant constant). The result of this observation is that the complete closed system is in fact specified by two variables, the quasi-geostrophic potential vorticity throughout the domain interior and the potential temperature anomaly at any horizontal surfaces. Both of these are conserved following the geostrophic component of the wind, a field which together they uniquely specify.

This boundary condition is central to the work of this thesis. However, there are several reservations on using this boundary condition for the QG equations, which we briefly note. Firstly, as illustrated above in Figure 1.1, regions of strong temperature gradient readily form on the horizontal boundaries. The associated jet structures and steeply sloped isentropes violate the QG scaling. Therefore, the QG system with rigid horizontal boundaries tends to evolve to situations that are outside of the regime of validity of its derivation. However, it is still a relevant model since the non-QG effects are generally confined to the regions of these small scale frontal features without influencing strongly the large scale flow.

Other problems are specific to each particular application. At the surface of the atmosphere boundary layer and topographic effects can be important. However, both of these effects can be accounted for by simple modifications. In the presence of topography with height $z = \eta_b(x, y)$, the condition of zero vertical velocity at the surface can be replaced, to the accuracy of QG theory, by the condition

$$w = \mathbf{u}_g \cdot \nabla \eta_b \quad \text{at} \quad z = 0 \tag{1.10}$$

(see Vallis (2006)). The potential temperature anomaly of an air parcel at the surface is no longer conserved. Instead it evolves as the parcel is advected across isentropic surfaces of the reference state. Substitution into (1.9) shows that the alternative quantity $\theta' + (\theta_{00} N^2 / g)\eta_b$ is conserved in this case. The leading order effect of boundary layer friction on the atmosphere is that of Ekman pumping. In this case the vertical velocity takes the form

$$w = r \nabla_{\mathrm{h}}^2 \psi \tag{1.11}$$

at the lower boundary where r is a constant proportional to the Ekman layer depth (Vallis, 2006). That is, the vertical velocity is proportional to the relative vorticity at the surface.

The application of the boundary condition to the tropopause can be simply considered accurate to the extent that the tropopause acts as a rigid lid on the troposphere below, as is the case for instance in the standard form of the famous Eady model of baroclinic instability (Vallis, 2006). However, a series of studies including Juckes (1994) and Juckes (1999) have suggested that the accuracy of this can be improved by assuming that the tropopause is in fact flexible and marks the boundary between two regions, the troposphere and stratosphere, of constant N. The papers show that if undulations of this surface are small then the associated tropospheric circulation is the same, again to the accuracy of QG theory, as that given by a temperature anomaly on a rigid upper boundary. The temperature anomaly in question is proportional to the vertical displacement of the tropopause surface and inversely proportional to the harmonic mean of the two N values. This formulation reduces to the rigid lid case when the stratospheric static stability is much larger than the tropospheric static stability.

Finally, the application of this boundary condition to the upper surface of the ocean has been explored recently in the literature, in particular by Lapeyre & Klein (2006) and

Klein et al. (2008). This is perhaps the simplest situation to justify since boundary layer effects are less dominant in the upper layers of the ocean than at the surface of the atmosphere.

The surface QG equations. The surface QG model results from considering the surface temperature component of the dynamics in isolation. We present the equations for the lower boundary of the atmosphere, but the system has also been applied to both of the other two horizontal boundaries mentioned above.

The isolation is achieved by considering an atmosphere which is unbounded above and by requiring q to be uniform and equal to f. Since q is conserved it will remain uniform and equal to f for all time. We further assume that ρ_0 and N are constants, a simplification which is rather restrictive for the atmosphere. Under these assumptions the quasi-geostrophic potential vorticity equation (1.1) reduces to

$$\nabla_h^2 \psi + \frac{f^2}{N^2}\frac{\partial^2 \psi}{\partial^2 z} = 0 \quad \text{in} \quad z > 0 \tag{1.12}$$

which is in effect a Laplace equation for ψ, and the lower boundary condition is given by

$$\frac{\partial \psi}{\partial z} = \frac{g}{\theta_{00} f}\theta' \tag{1.13}$$

with

$$\frac{D\theta'}{Dt} = 0 \quad \text{at} \quad z = 0 \tag{1.14}$$

To close the system we further assume that all fields decay at large z. Equations (1.12)-(1.14) along with this far field condition are called the surface QG equations.

In summary, the key ingredients of surface QG dynamics are (i) quasi-geostrophic dynamics, (ii) the presence of a flat horizontal boundary, and (iii) negligible interior potential vorticity. The system is two-dimensional (despite modelling a three-dimensional atmosphere) since it is determined fully by the surface temperature field. The structure of the equations are in fact very similar to those of the 2-d Euler equations, which is something we discuss in detail below. Further to these three ingredients, it is also assumed here that ρ_0 and N are both constant throughout the atmosphere, which is quite a restrictive assumption for atmospheric purposes. In Chapter 4 we discuss a simple extension which has been explored in the literature whereby the background density profile is taken instead to be $\rho_0 \propto e^{-z/H}$ where H is a suitable height scale.

It is standard practice to scale z and θ' in (1.12)-(1.14) to remove the dimensional constants from the equations. Slightly ambiguously, it is also standard practice to call the scaled temperature variable θ, and this is a convention we follow:

$$z \mapsto \frac{f}{N} z \tag{1.15}$$

$$\theta' \mapsto \frac{\theta_{00} N}{g} \theta. \tag{1.16}$$

From now on θ will stand for this scaled potential temperature anomaly, unless otherwise specified. Note that it has the dimension of a velocity field. The scaled versions of the equations are given by

$$\nabla^2 \psi = 0 \quad \text{in} \quad z > 0 \tag{1.17}$$

with

$$\frac{D\theta}{Dt} = 0 \quad \text{at} \quad z = 0 \tag{1.18}$$

and the balanced variables are recovered via

$$(u, v, \theta) = \left(\frac{\partial}{\partial y}, -\frac{\partial}{\partial x}, \frac{\partial}{\partial z} \right) \psi. \tag{1.19}$$

As before we close the system by requiring all fields to decay at large z. This is the form of the equations studied in Chapters 2 and 3 of this thesis.

Typical extra-tropical atmosphere values for the quantities in (1.15) are given by Ambaum (2010) as $f = 10^{-4}\,\mathrm{s}^{-1}$ and $N = 10^{-2}\,\mathrm{s}^{-1}$ so that $N/f \approx 100$. This represents the typical aspect ratio of a streamfunction (i.e. pressure) anomaly associated with an isolated potential vorticity anomaly. A typical value for potential temperature is $\theta_{00} = 300\,\mathrm{K}$ so that $\theta_{00} N/g \approx 0.3\,\mathrm{K}(\mathrm{ms}^{-1})^{-1}$ in (1.16). Using these values gives the interpretation that if one θ unit represents one degree Kelvin then one velocity unit represents about $3.3\,\mathrm{ms}^{-1}$.

Capped surface QG dynamics and the uniform potential vorticity model. The surface QG model works well at the surface of the atmosphere, but its application is severely limited by assuming the atmosphere to be unbounded above. Taking an extra-tropical tropopause height of 10 km along with the above estimate of $N/f = 100$ as a typical horizontal/vertical aspect ratio of streamfunction anomalies leads to a maximum horizontal scale of around 1000 km at which the inversion of surface temperature anomalies will be altered by the strong increase in N above the tropopause. Put another way, the wind and temperature fields which are in balance with a given surface temperature distribution will be significantly different to those obtained via the surface QG inversion. Perhaps more significantly, when the surface QG model is applied as a model of tropopause undulations, the opposing boundary is then the rigid surface of the Earth.

To obtain a more accurate model in these cases, without complicating the mathematical structure significantly, Tulloch & Smith (2006) introduced a new setup which we will call capped surface QG dynamics. The model is a variant of surface QG dynamics which captures the finite-depth nature of the troposphere by imposing a rigid iso-thermal upper boundary at tropopause level. The assumed lack of temperature variations on this boundary means it does not explicitly contribute to the dynamics. Instead it just modifies the dynamics of the larger-scale temperature anomalies on the lower surface which 'feel' its presence.

The boundary conditions for the QGPV inversion in capped surface QG dynamics are therefore the third component of (1.19) applied at $z = 0$ complimented by the condition

$$\frac{\partial \psi}{\partial z} = 0 \quad \text{at} \quad z = H \tag{1.20}$$

where H is the depth of the troposphere. As we discuss below, this condition makes large scale features behave more like 2-d Euler dynamics than surface QG.

The final model we discuss here is the next logical extension to this. It is to allow temperature variations on both bounding surfaces. The result is a two component model which is determined entirely by the combined effects of the potential temperature distributions at the upper and lower boundaries. This is the framework in which the famous Eady model is posed. Blumen (1978) calls the model uniform potential vorticity dynamics, although of course both surface QG and capped surface QG have uniform potential vorticity as well. In the absence of any other consistent name in the literature, however, we will retain this term for the model. We use both capped surface QG and uniform potential vorticity dynamics in Chapter 4.

1.3 Aspects of surface QG dynamics

This section contains some background theory which is scattered throughout the literature. We have brought together the most relevant topics in order to both outline the boundaries of current knowledge and provide motivation for the key scientific questions discussed in the next section.

1.3.1 Inversion operators and the Bretherton interpretation

As mentioned above, the surface QG system is closely related to that of 2-d Euler dynamics. Both are examples of 2-d advected-scalar flows whereby the scalars - the surface temperature field in surface QG dynamics and the vorticity in the 2-d Euler case - are 'active' in the sense that they completely determine the flow field, and in particular the velocity field by which they are advected. The only difference between the systems, apart from physical interpretation, is in the relation between the advected scalar field and the streamfunction. Here we note down some expressions for the inversion operators of each system for later reference and then present an insightful physical interpretation of the two systems as simple limiting cases of quasi-geostrophic potential vorticity dynamics.

For ease of reading, we suppress the z-dependence of all variables and consider only their surface values. The inversion (1.17)-(1.19) of a surface temperature distribution $\theta(\mathbf{x})$, where $\mathbf{x} = (x, y)$, can then be written as

$$\psi(\mathbf{x}) = -\frac{1}{2\pi} \iint \frac{\theta(\mathbf{x}')}{|\mathbf{x} - \mathbf{x}'|} \, d^2\mathbf{x}', \tag{1.21}$$

so that the Green's function for the inversion is given by

$$\mathrm{G}(|\mathbf{x}|) = -\frac{1}{2\pi|\mathbf{x}|} \tag{1.22}$$

which is related to the full three-dimensional QGPV Green's function as we show below. For a one-dimensional surface temperature profile $\theta = \theta(y)$ the inversion simplifies slightly. After differentiating (1.22) in the $y-$direction and then performing the x' integration, the resultant surface velocity field takes the form of a Hilbert transform,

$$u(y) = -\mathcal{H}[\theta] \equiv -\frac{1}{\pi} \int_{-\infty}^{\infty} \frac{\theta(y')}{y - y'} \, dy', \quad v = 0 \tag{1.23}$$

where the integral is a principal value integral. The Hilbert transform has the special property that it is the negative of its inverse: $\mathcal{H}[\mathcal{H}[f]] = -f$ for any function f (Ambaum & Athanasiadis (2007)), meaning there is an interesting symmetry between the surface velocity and temperature fields for one-dimensional profiles. It also has the property that if the function f tends to finite limits at $\pm\infty$ then $\mathcal{H}[f]$ only exists if

$$\lim_{y \to -\infty} f(y) = \lim_{y \to +\infty} f(y). \tag{1.24}$$

This means that there are no solutions to the surface QG inversion that decay at $z \to \infty$ when this condition is not met by the surface temperature field. The condition (1.24) is clear from (1.23) since the integral of $1/x$ is divergent. This is an important result; it shows that the simple two-dimensional profile of a Heaviside step function, or any other simple frontal structure, is not a possible basic state in surface QG dynamics. It does not, however, rule out the possibility of basic states which do not tend to finite limits at ±∞, for instance perturbations on a uniform temperature gradient. See Section 1.3.3 for further discussion on the implications of (1.24).

Equation (1.21) can be derived by considering the Fourier transform of the full three-dimensional system as follows. We define the two-dimensional Fourier transform of the surface temperature $\hat{\theta}(\mathbf{k})$ such that

$$\theta(\mathbf{x}) = \iint \hat{\theta}(\mathbf{k}) e^{i\mathbf{k}\cdot\mathbf{x}} \, d^2\mathbf{k}. \tag{1.25}$$

Then, since θ is harmonic in the fluid interior, the full three-dimensional temperature field is recovered when the integrand is multiplied by $e^{-|\mathbf{k}|z}$. Therefore from (1.19) the surface streamfunction is related to the surface temperature field in Fourier space via the expression

$$\hat{\psi}(\mathbf{k}) = -\frac{\hat{\theta}(\mathbf{k})}{|\mathbf{k}|}. \tag{1.26}$$

The real-space expression (1.21) is then recovered using the convolution theorem for Fourier transforms along with the standard result that the Fourier transform of $1/|\mathbf{x}|$ is given by $1/|\mathbf{k}|$.

For comparison we also note down the corresponding results for the analogous 2-d Euler system, which we write as

$$\frac{Dq}{Dt} = 0 \quad \text{with} \quad q = \nabla_h^2 \psi \tag{1.27}$$

where ∇_h^2 is the two-dimensional horizontal Laplacian operator. It is clear that this is formally the same as the quasi-geostrophic potential vorticity equation (1.1) if there are no vertical variations present. In this respect 2-d Euler dynamics can be thought of as the dynamics of infinitely tall potential vorticity anomalies either in the absence of any horizontal boundaries or with horizontal boundaries present but with no temperature variations along them.

The 2-d Euler Green's function and its Fourier space representation are given by (see, e.g., Saffman (1995))

$$G(|\mathbf{x}|) = -\frac{\log|\mathbf{x}|}{2\pi} \quad \text{and} \quad \hat{\psi}(\mathbf{k}) = -\frac{\hat{q}(\mathbf{k})}{|\mathbf{k}|^2} \tag{1.28}$$

which result in a more non-local dynamics compared to the surface QG system. In physical space this is clear since the form of the Green's functions imply that velocity fields associated with a localised 2-d Euler vorticity distribution will decay like $1/r$, whereas those associated with a localised surface QG temperature distribution will decay faster, like $1/r^2$. Consistently, in spectral space the vorticity inversion damps high wavenumbers more strongly than the temperature inversion.

Bretherton (1966b) noted that surface temperature anomalies are in fact equivalent to singular contributions to the quasi-geostrophic potential vorticity field at the surface. To see this, consider the sketch of Figure 1.2. The shaded region represents a volume of uniform potential vorticity q_0 in an unbounded atmosphere otherwise at rest. The volume is thin in the vertical direction, confined by the region $-ch(x,y)/2 < z < ch(x,y)/2$ where c is a small length scale and h an order one function of horizontal position. The faint lines in the sketch represent isentropes which, as is typical of a positive PV anomaly, are 'pulled' down above it and 'drawn up' below it (see Hoskins et al. (1985)).

Taking the limit $c \rightarrow 0$ leads to no motion; however, if we also require q_0 to increase such that cq_0 remains fixed then a limit with finite motion is achieved. The potential vorticity becomes a δ-function in this limit and the corresponding (constant ρ_0 and N) quasi-geostrophic potential vorticity equation reduces to

$$\nabla_h^2 \psi + \frac{gf}{\theta_{00} N^2} \frac{\partial \theta'}{\partial z} = cq_0 h(x,y) \delta(z). \tag{1.29}$$

Integrating this in the vertical from $z = 0^-$ to $z = 0^+$ leads to the expression

$$\frac{gf}{\theta_{00} N^2} \Delta^{\pm} \theta' = cq_0 h(x,y) \tag{1.30}$$

which means there is a temperature jump of magnitude $\Delta^{\pm}\theta = cq_0 h(x,y)$ in the scaled variables across the plane $z = 0$: some isentropes are pulled completely together in this limit.

The final step in relating this setup to surface QG dynamics is to replace the only unaltered isentrope (dashed in the diagram) by a rigid boundary. Through symmetry the temperature and wind fields in the half space $z > 0$ are unchanged and the boundary condition is given by the temperature there which is $\theta = cq_0 h(x,y)/2$. In summary, then,

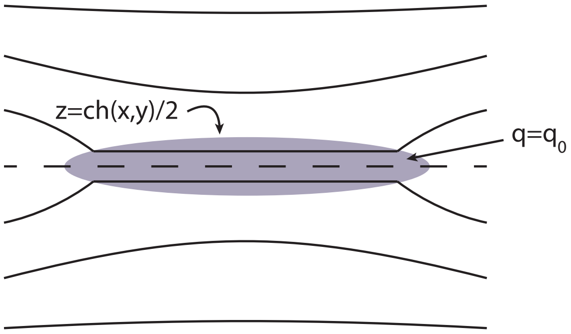

Figure 1.2 A sketch illustrating the Bretherton (1966b) interpretation of surface temperature anomalies. The lines are isentropic surfaces and the shaded region represents an isolated QGPV anomaly of strength $q = q_0$.

the surface temperature field can be incorporated into the quasi-geostrophic potential vorticity field as a δ-function term in the vertical and then the boundary conditions taken to be homogeneous.

As a final comment which is relevant to both the physical interpretation of the two systems mentioned above and the form of the inversion operators, we note the difference in the dimensions of vorticity and temperature. Vorticity has the dimension of a frequency, indeed it represents half the local angular rotation rate of fluid particles, whereas the scaled temperature anomaly we are using has the dimension of a velocity field. The extra length scale changes qualitatively many aspects of the dynamics.

1.3.2 Conserved quantities

A direct consequence of the similarity between the surface QG and 2-d Euler inversion operators is that they share similar integral constraints. The integral constraints of the 2-d Euler system have well understood implications regarding turbulence scaling arguments and the same is true for surface QG dynamics (see Pierrehumbert et al. (1994), Held et al. (1995) and Capet et al. (2008)). Here we briefly present the conserved quantities for later reference. We also comment on their relation to the full three-dimensional QG dynamics.

Energy. First, consider the expression

$$E = -\frac{1}{2}\int \psi\theta \, \mathrm{d}A. \tag{1.31}$$

This is conserved in time and has the dimension of an energy variable integrated over a volume. It is in fact the total energy (KE + APE) of the full three-dimensional flow field. To see this, we write the total energy in QG theory as

$$E = \frac{1}{2}\int (\nabla\psi)^2 \, \mathrm{d}V \tag{1.32}$$

where $(\nabla\psi)^2 = u^2 + v^2 + \theta^2$ is the sum of the local kinetic and the available potential energies (Vallis (2006)). To find the contribution of the boundary (using the usual semi-infinite surface QG domain), note that $(\nabla\psi)^2 = \nabla\cdot(\psi\nabla\psi) - \psi\nabla^2\psi$, so that we can apply Gauss's theorem to give (noting that $\nabla^2\psi = q$ is the QGPV)

$$\int (\nabla\psi)^2 \, \mathrm{d}V = -\int \psi\theta \, \mathrm{d}A - \int \psi q \, \mathrm{d}V \tag{1.33}$$

provided the streamfunction decays rapidly enough at large r. Therefore the expression (1.31) does indeed represent the total energy of the full three-dimensional flow field when the interior QGPV is zero.

Momentum. Next, we consider the conservation of momentum. The same calculation can be done for linear and angular momentum; we just present the angular case for brevity. In QG theory the angular momentum

$$J = \int r u_\varphi \, \mathrm{d}V, \tag{1.34}$$

where $u_\varphi = \partial\psi/\partial r$ is the azimuthal velocity field, is conserved. Again we look to write this in terms of separate q and θ contributions. This time we note that

$$\begin{aligned} 2ru_\varphi &= \nabla\psi \cdot \nabla r^2 && (1.35) \\ &= \nabla \cdot (r^2 \nabla\psi) - r^2 \nabla^2 \psi && (1.36) \end{aligned}$$

and therefore, again applying Gauss's theorem to the divergence term, J can be expressed as

$$J = -\frac{1}{2} \int r^2 \theta \, \mathrm{d}A - \frac{1}{2} \int r^2 q \, \mathrm{d}V \tag{1.37}$$

provided the streamfunction decays rapidly enough at large r. As for the energy, then, the angular momentum of the full three-dimensional flow field reduces to a simple surface integral when the interior QGPV is zero.

Enstrophy. The enstrophy in three-dimensional QG dynamics can be defined layer-wise or else as a volume integral over the full domain. The surface component can be thought of as one of the layer-wise components, although it cannot be written naturally as a contribution to the full domain enstrophy since it has a different dimension to the interior enstrophy:

$$Z_{\mathrm{sfc}} = \int \theta^2 \, \mathrm{d}A \qquad Z_{\mathrm{int}} = \int q^2 \, \mathrm{d}V. \tag{1.38}$$

The enstrophy constraint is slightly different to the energy and momentum constraints of (1.33) and (1.37) since the surface and interior components are each conserved individually. In particular, the surface integral of θ^2 is conserved whether there is interior potential vorticity anomalies or not.

One point which sometimes causes confusion in surface QG dynamics is that the integral of the surface kinetic energy is, by (1.26) and Parseval's theorem, equal to this surface QG enstrophy:

$$\int |\mathbf{u}|^2 \, \mathrm{d}A = \int |\hat{\boldsymbol{u}}|^2 \, \mathrm{d}^2\mathbf{k} = \int |\hat{\theta}|^2 \, \mathrm{d}^2\mathbf{k} = \int \theta^2 \, \mathrm{d}A. \tag{1.39}$$

This quantity is therefore conserved, but it is an enstrophy variable. The integral of the kinetic energy in the 2-d Euler system is also conserved, but that is analogous to the total energy of surface QG dynamics discussed above.

Two final remarks. Part of the reason for writing out these expressions is to complete the comparison made earlier between surface QG and 2-d Euler dynamics in terms of QGPV anomalies. Each of the expressions (1.33), (1.37) and (1.38) clearly reduce to the surface QG versions under the assumption of $q = 0$. They also reduce the to familiar 2-d Euler expressions under the assumption of no z-dependence. To make the integrals finite (and the dimensions match) q must be interpreted as a depth-average QGPV value.

The other remark concerns the energy spectra of surface QG turbulence. It is a standard derivation (e.g., Pierrehumbert et al. (1994)) to take these expressions for energy and enstrophy and derive an expression for the energy spectra, $e(k)$, of well-developed forced-dissipative turbulence. First one must show that typically enstrophy is transferred to small scales, which, for instance, necessarily occurs if the variance of the energy spectra increases. Then, on the assumption that the enstrophy at small scales is dissipated at a constant rate η, the following two scaling laws are obtained for the surface QG and 2-d Euler systems respectively:

$$e^{2dE}(k) \propto \eta^{2/3}k^{-3} \quad \text{and} \quad e^{SQG}(k) \propto \eta^{2/3}k^{-8/3}. \tag{1.40}$$

These are often compared directly. However, we would like to place a more physical emphasis on the expressions by briefly noting why they are different. There are two contributions to the difference. The first is that the difference between the inversion operators (1.26) and (1.28) mean that there should be an extra factor of k in the surface QG expression. This is a purely kinematic effect. The second is that the dynamical evolutions of the vorticity and temperature fields are qualitatively different, leading to different spectra of the statistically steady states. To see this more clearly, we note from the above expressions that a vorticity field which gives the energy spectra of (1.40) must have a spectrum of the form

$$\tilde{q}(k) \propto k^{-1} \tag{1.41}$$

whereas a temperature field which gives the surface QG energy spectra must have a spectrum of the form

$$\tilde{\theta}(k) \propto k^{-4/3}. \tag{1.42}$$

The evolution of surface QG turbulence simulations is therefore qualitatively different such that the spectrum of the temperature field is steeper than the spectra of 2-d Euler vorticity distributions by a factor of one third. It is one manifestation of this difference that we study in Chapter 3 when we investigate the stability of filaments, and we return to this point at the end of that chapter.

1.3.3 The dynamics of temperature discontinuities

One particularly interesting feature of surface QG dynamics is the behaviour of discontinuities in the advected scalar field. Such temperature discontinuities induce singular velocity fields. To see this, we present the analysis of Held et al. (1995).

Consider a single patch of uniform temperature $\theta = \theta_0$ bounded by a smooth closed curve $\mathcal{C}$. The contour dynamics formula (see Dritschel (1988a) or Pullin (1992)) gives the velocity field at any point $\mathbf{x}$ as

$$\begin{pmatrix} u_x(\mathbf{x}) \\ u_y(\mathbf{x}) \end{pmatrix} = \theta_0 \oint_{\mathcal{C}} \mathrm{G}(|\mathbf{x} - \mathbf{x}'|) \begin{pmatrix} \mathrm{d}x' \\ \mathrm{d}y' \end{pmatrix} \tag{1.43}$$

where G is the surface QG Green's function given by (1.22). Suppose that at the point $\mathbf{x} = 0$ the patch boundary is parallel to the x-axis so locally it can be written as $y = bx^2/2$. Then, substituting into (1.43) the local contribution to the integrals become

$$\tilde{u}_x = \theta_0 \int_{\tilde{\mathcal{C}}} \frac{\mathrm{d}x'}{|x'|} \quad \text{and} \quad \tilde{u}_y = \theta_0 \int_{\tilde{\mathcal{C}}} \frac{bx'\mathrm{d}x'}{|x'|} \tag{1.44}$$

where $\tilde{\mathcal{C}}$ is the portion of the boundary near to $\mathbf{x} = 0$. Clearly this contribution to the tangential (i.e. along-front) velocity u_x is logarithmically singular at the boundary, whereas the local contribution to the perpendicular component u_y vanishes at leading order, meaning the advection of the boundary can be regular despite the infinite velocity there. This observation forms a central theme of this thesis. We consider the dynamics of several piecewise uniform temperature profiles and the result that the evolution of such profiles is regular, despite the singularity in the velocity field, is crucial.

Given that such a temperature front evolves 'slowly', the next logical step is to try and find a linear wave-like solution for perturbations to it. This is a problem we tackle in Chapter 2. Unfortunately, as noted above, the most obvious basic state of a one-dimensional step function:

$$\theta(y) = \theta_0 \mathrm{H}(y) \tag{1.45}$$

is not a possible basic state for the surface QG equations because it does not meet the condition of (1.24). To understand this more thoroughly, we note that there are solutions of the Laplace equation[1] which satisfy (1.45) as a lower boundary condition, the simplest given by

$$\theta(y,z) = \theta_0 \left(\frac{1}{2} + \frac{1}{\pi} \tan^{-1}(x/z) \right), \tag{1.46}$$

---

[1] Recall that ψ is harmonic, and therefore $\theta = \psi_z$ is as well

which has the corresponding velocity field

$$u(y,z) = \frac{\theta_0}{2\pi}\left(\log(y^2+z^2)+C\right) \tag{1.47}$$

where C is an integration constant. Even though θ decays as z increases, the velocity field does not tend to zero and therefore the large z boundary condition of the surface QG system is not met.

Instead of using the straight one-dimensional front of (1.45), we solve an alternative problem of the evolution of waves on a circular temperature front, or Rankine vortex, in Chapter 2. The main technical difficulty in this calculation comes from the singularity in the along-front velocity field discussed above: material flows along the boundary at an infinite speed. However, the work of Juckes (1995) has already solved this problem. In that study (which is discussed in detail in Section 3.2) the stability of a temperature filament with a top-hat profile is investigated analytically. The problem is solved by carefully linearising the equations about small material displacements of the frontal contour rather than small variations in the velocity or temperature fields. An isolated temperature filament clearly does satisfy the constraint of (1.24) and, further, each filament edge is a temperature discontinuity which supports wave-like disturbances. The paper only presents the evolution equations for the full stability problem in which perturbations on each edge propagate along the fronts as well as interacting with the opposing edge. However, implicit in the equations is the dispersion relation for each edge wave, which can be written as

$$c_{\mathrm{p}} = \theta_0 \log k + C \tag{1.48}$$

where c_{p} is the phase speed of disturbances of wavenumber k, θ_0 is the temperature anomaly of the filament and C a constant. Note that the position of the wavenumber k within the logarithm means that its dimension (1/length) must be balanced by a length scale. For the filament problem this is provided by the width of the filament which enters (1.48) as a $\log L$ term in the constant C. Clearly in the simple Heaviside step function case of (1.45) there are no length scales imposed, so the lack of a solution is consistent with this observation.

Finally we note the calculation presented in Appendix A of Juckes (1995). Crucially, it is shown there that despite the velocity singularity the wave propagation characteristics of a slightly smoothed discontinuity are regular in the limit of sharp edges, at least for wavenumbers $k \ll \delta L$ where δL is the width of the smoothing. This observation is crucial since, as noted above, the assumptions behind quasi-geostrophic theory break down in regions of strong horizontal temperature gradients. The hope is that the behaviour displayed in the sharp edge limit carries over to the smooth case where the theory still holds.

1.3.4 A turbulence snapshot

As a final part of this short survey we present in Figures 1.3-1.6 some snapshots of freely decaying turbulence in the surface QG and 2-d Euler models. The purpose is to illustrate further motivation for the work of this thesis.

The code used to make the plots was developed specifically for this thesis and is used in Chapters 2 and 4. As such a description of the numerics as well as results from some basic tests are presented in Appendix A. As a summary, the code integrates either system using a semi-Lagrangian method where the inversion is performed in spectral space using the spectral form of the Green's functions. The semi-Lagrangian advection scheme uses a bi-cubic interpolation method which is shown in the appendix to have similar dissipative effects as adding a biharmonic diffusion term ($\propto \nabla^4\theta$) to the right hand side of (1.18).

Both simulations were run on a doubly periodic domain with the same quasi-random initial temperature/vorticity distributions which has spectral coefficients significantly non-zero only in the range of wavenumbers 2-6 (the domain width is 1), with a peak at wavenumber 4. The initial temperature and vorticity fields were normalised such that the integral of their square over the domain is equal to unity. The times of the snapshots shown were chosen so as to allow a qualitative comparison between the two systems; the times of the surface QG snapshots are roughly $1/16^{\text{th}}$ that of the 2-d Euler snapshots. This is because the initial velocity field of the surface QG simulation is typically about 16 times larger than that of the 2-d Euler case.

To see why this is the case, recall that the velocity field induced by a surface QG temperature anomaly is independent of the size of the anomaly whereas that induced by a vorticity anomaly in 2-d Euler dynamics is proportional to the size of the anomaly. In the case of Figures 1.3-1.6 the typical radii of the anomalies in the initial condition are about 1/16th the width of the domain and therefore the velocity field in the 2-d Euler case has 1/16th the magnitude of the velocity induced by an anomaly of size $O(1)$. The surface QG velocity field however has the same magnitude as that induced by a temperature anomaly of size $O(1)$. To see that smooth anomalies of size $O(1)$ would induce velocities of similar magnitudes in the two systems we note that the circulation at a distance r around a circularly symmetric vorticity anomaly $q(r)$ is given by

$$2\pi r u_{\mathrm{r}} = 2\pi \int_0^r q(r) r \, \mathrm{d}r, \tag{1.49}$$

where u_{r} is the azimuthal velocity field, whereas in the surface QG system this reduces to the expression

$$2\pi r u_{\mathrm{r}} = -2\pi \int_0^r \theta_z(r) r \, \mathrm{d}r \tag{1.50}$$

because the condition of zero interior QGPV requires $q = -\theta_z$. Therefore, the circulations near the edge of a smooth vortex of size r and typical vorticity q_0 in the 2-d Euler case and temperature θ_0 in the surface QG case will scale as

$$u_{\mathrm{r}}^{\mathrm{2dE}} \sim \frac{r}{2} q_0 \quad \text{and} \quad u_{\mathrm{r}}^{\mathrm{SQG}} \sim \frac{1}{2}\theta_0. \tag{1.51}$$

Both systems will therefore have velocities of similar magnitudes when $r = 1$. Note that this argument requires the profiles to be smooth, otherwise θ_z will not scale as θ_0/r which is assumed in (1.51); when there are sharp temperature gradients present the surface QG case induces large velocities as discussed above.

An alternative viewpoint to this discussion is to consider instead typical eddy turnover times τ in each system. The eddy turn-over time is the time taken for the fluid in a vortex to rotate by a full circle and is given by the expression

$$\tau = \frac{2\pi r}{u_{\mathrm{r}}}. \tag{1.52}$$

Therefore the eddy turnover times in the 2-d Euler case are independent of the eddy size whereas they decrease with decreasing eddy size in the surface QG system.

Returning now to discuss the plots of Figures 1.3-1.6, we note that the two systems show several notable similarities. There is a tendency to form large coherent vortices whilst simultaneously producing a complicated small scale structure, features which are well known to be consistent with the combined constraints of energy and enstrophy conservation (see Section 1.3.2). The nature of the small scale structure, however, is remarkably different between the two. The enlarged pictures of Figures 1.4 and 1.6 show this most clearly. In 2-d Euler dynamics filaments of vorticity are constantly formed due to vortex stripping and the stretching out of weak vorticity anomalies by larger scale straining. In surface QG the same process occurs but the filaments appear to be unstable because there are very few coherent filaments in the snapshot. Instead there are many smaller vortices resulting from the instability of the filaments. We study this instability process in detail in Chapter 3.

1.4 Outline of the thesis

The original work in this thesis is split naturally into three chapters, Chapters 2–4. The subject matter of each chapter is fairly distinct and as such each chapter includes its own introduction section, a section reviewing previous work on the subject and a short discussion section. There is also a final Discussion chapter, Chapter 5 which attempts to link together the three earlier chapters.

So far three papers have been published based on the work of this thesis, two from Chapter 2 and one from Chapter 3. We plan to write up the work of Chapter 4 for publication at a later date.

1.4.1 Key scientific questions

There are four key scientific questions that this thesis sets out to answer. The first illustrates a broad theme for the whole thesis whereas each of the others are taken up individually by the three work chapters.

1. What are the main qualitative differences between surface QG dynamics and 2-d Euler? This simple question forms a main overriding theme of this thesis. The viewpoint taken is that the 2-d Euler system has been comprehensively studied for a long time and is well understood. It therefore provides a useful reference with which results from the surface QG system can be compared. The problems studied in Chapters 2 and 3 in particular give insight into the important differences between the systems. Chapter 4 illustrates the importance of understanding the properties of both systems when thinking about large scale dynamics of the atmosphere.

2. What are the properties of waves propagating on surface QG temperature fronts? The discussion above points towards the intriguing nature of waves on temperature fronts in surface QG dynamics. The question is again relevant to each chapter, but is most closely examined in Chapter 2 where we derive a new dispersion relation for an important example of such waves.

3. What controls the small scale instability in surface QG simulations? This question is tackled in Chapter 3. We present a linear stability analysis of filamentary temperature structures which leads to a simple scaling argument for the distribution of vortices in surface QG turbulence.

4. What is the behaviour of baroclinically unstable frontal setups in the uniform PV dynamics model? In the final work chapter a new simple analytic model of baroclinic instability is described and investigated. The new model has similar conceptual simplicity as the well-known Eady model, but importantly confines the baroclinic zone into a frontal structure. This question is aimed at understanding the instability that develops in the system.

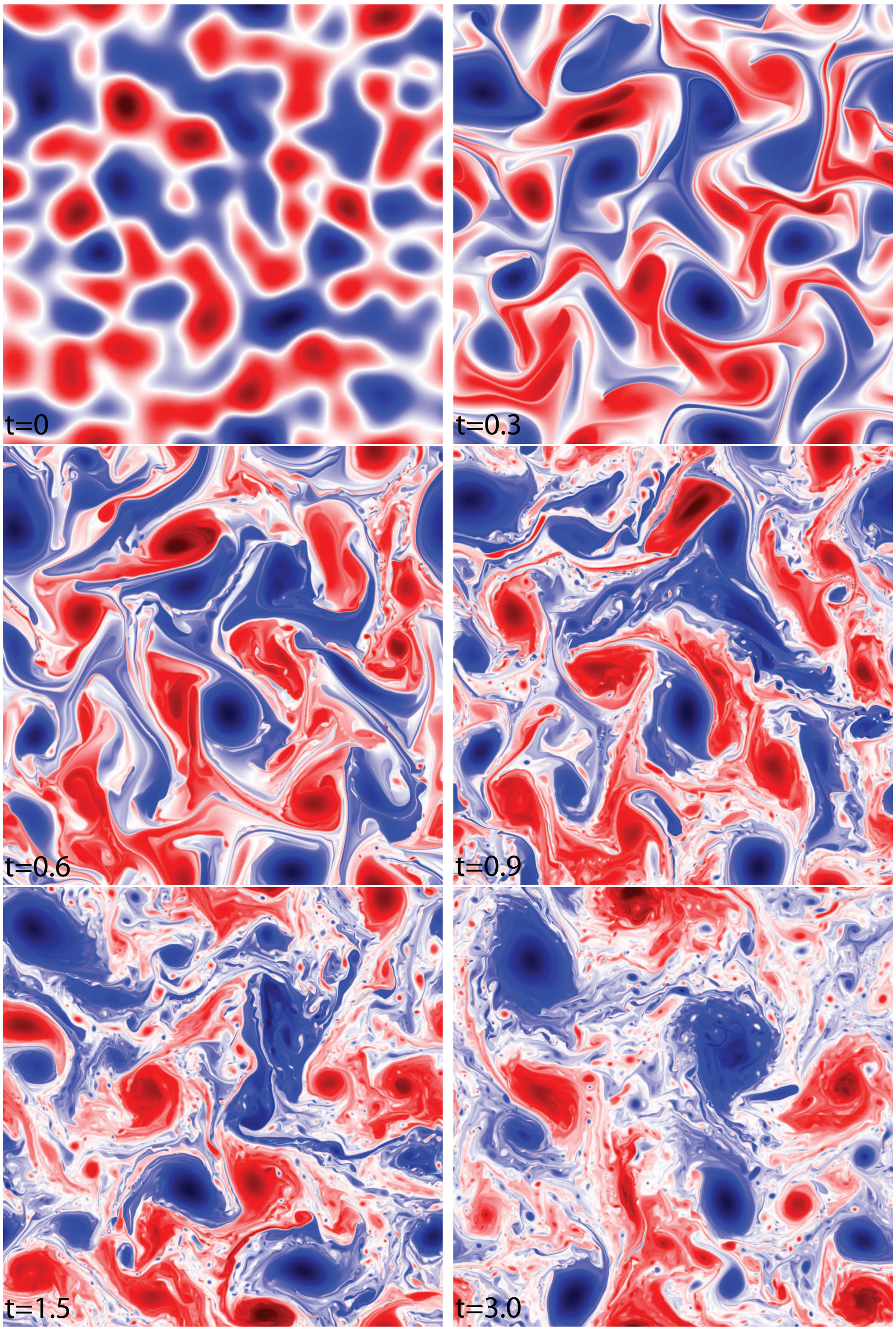

Figure 1.3 A time series of snapshots from a freely decaying surface QG simulation. Colours represent the surface temperature field with warm anomalies red and cool anomalies blue. The times of the snapshots are $t = 0, 0.3, 0.6, 0.9, 1.5$ and 3 as indicated. The numerical model, which was run at resolution $n = 2048$ grid points in each direction for this simulation, is described in the text and Appendix A. The initial temperature field was generated by randomly selecting the locations and amplitudes of n^2 Fourier coefficients and then modulating the amplitudes by the factor $\mathrm{e}^{-(k-4)^2/20}$ to localise the distribution around wavenumber $k = 4$ (the domain is a unit square). This initial temperature distribution was then normalised so that $\int \theta^2 \, \mathrm{d}A = 1$.

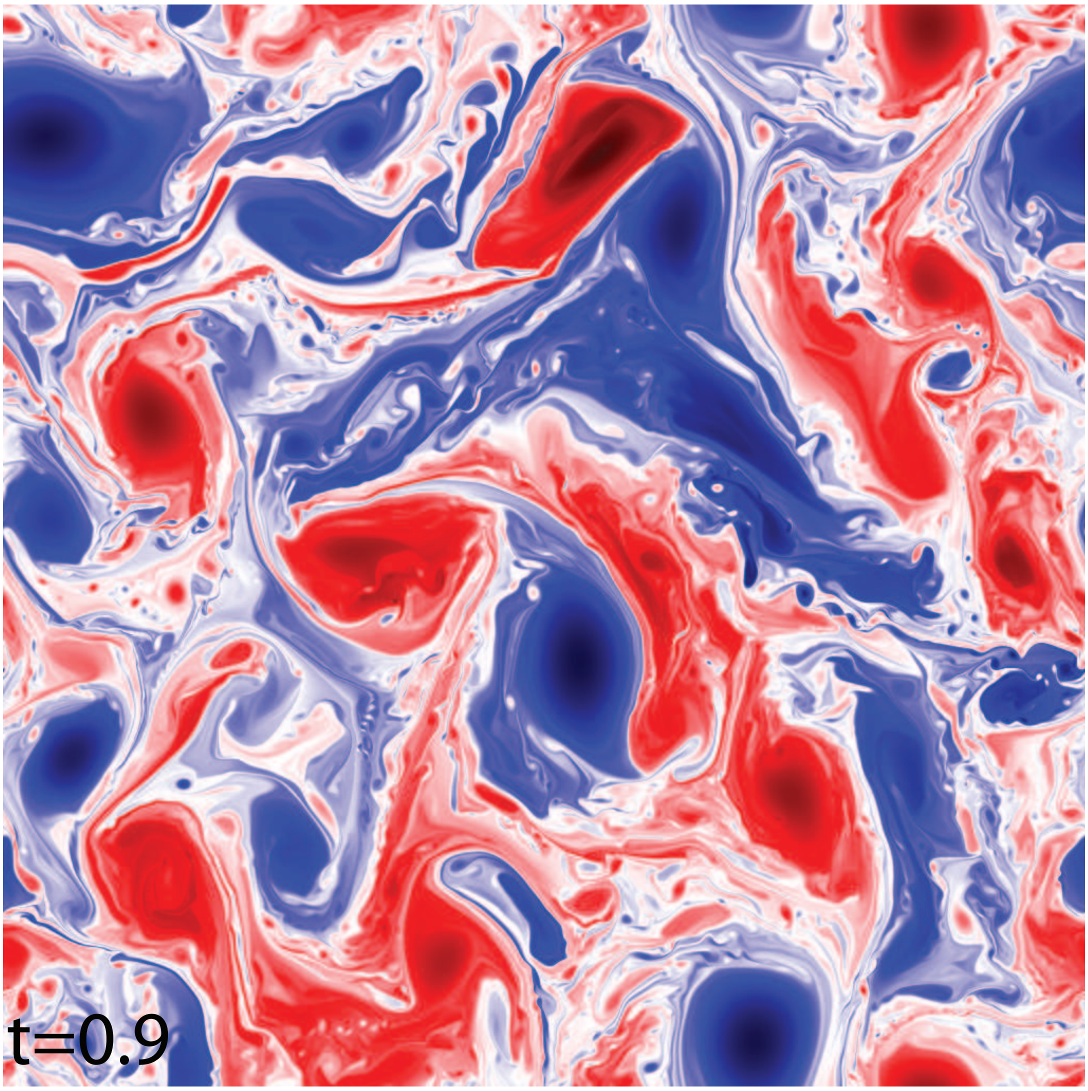

Figure 1.4 An enlarged version of the $t = 0.9$ plot from Figure 1.3.

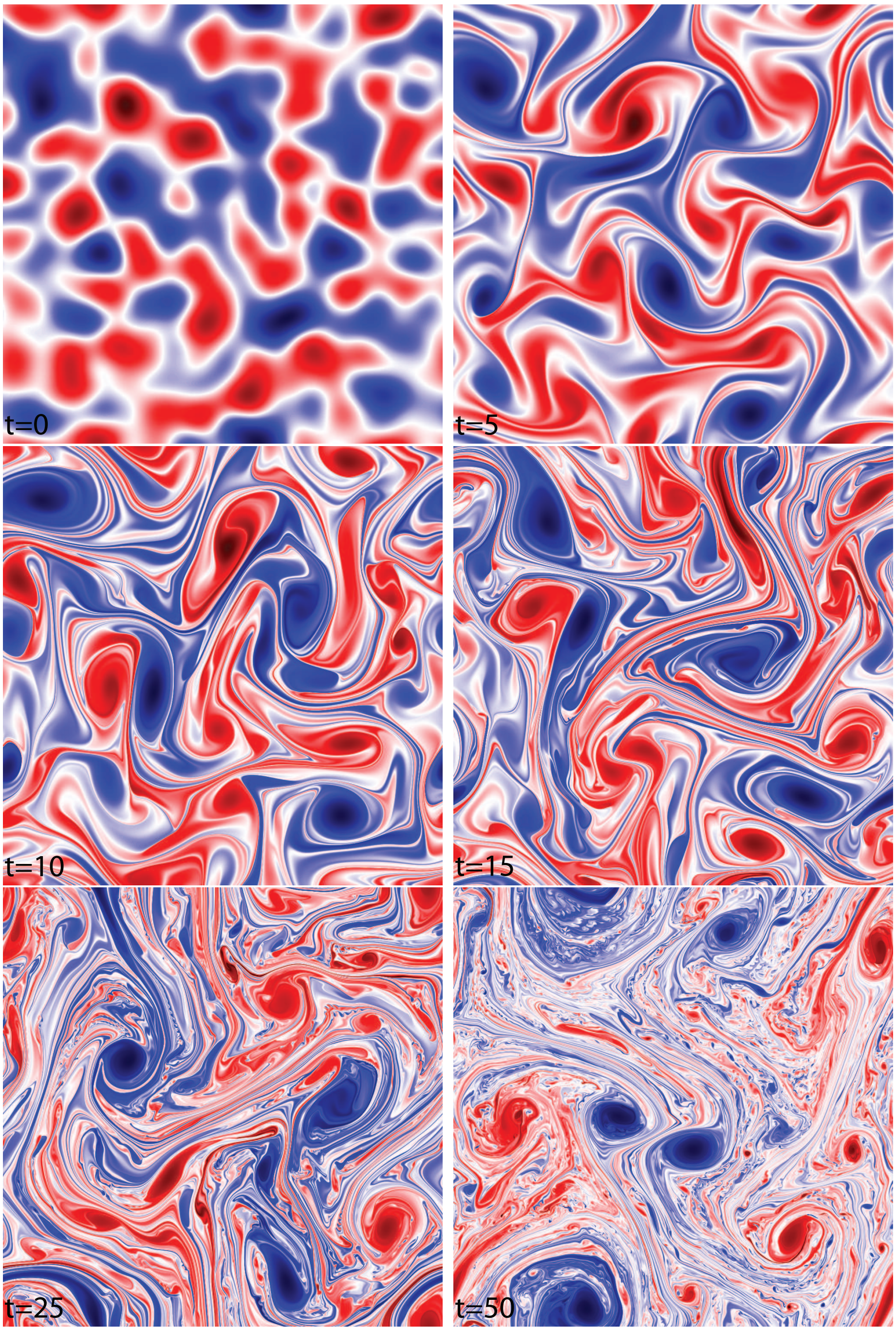

Figure 1.5 A time series of snapshots from a freely decaying 2-d Euler simulation. Colours represent the vorticity field with cyclonic anomalies red and anticyclonic anomalies blue. The times of the snapshots are $t = 0, 5, 10, 15, 25$ and 50 as indicated. These have been chosen to correspond roughly to the plots of Figure 1.3 as described in the text. The numerical model is the same as that used for Figure 1.3, except that the 2-d Euler Green's function has been used instead of the surface QG version. The initial vorticity field is the same as the initial temperature field of Figure 1.3.

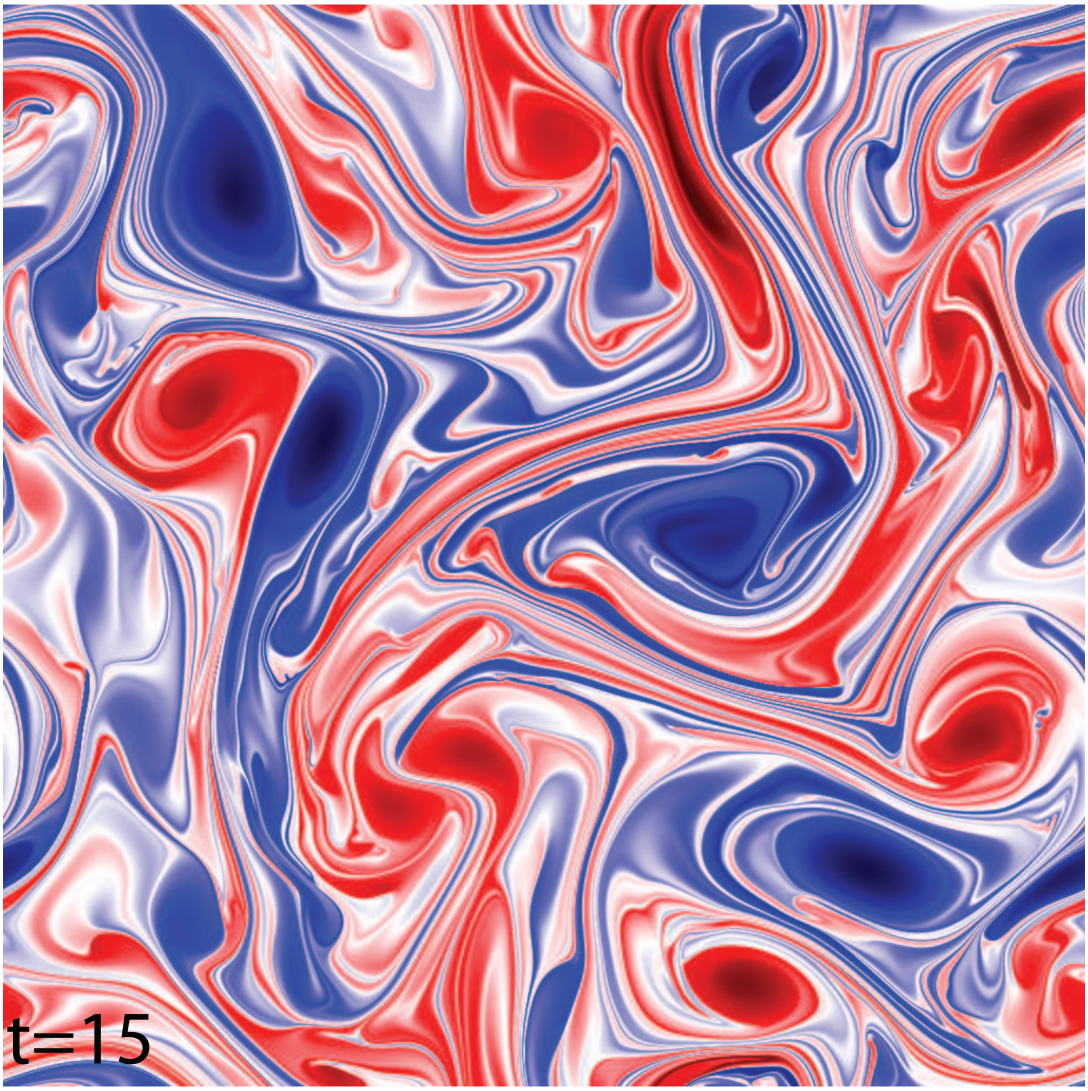

Figure 1.6 An enlarged version of the $t = 15$ plot from Figure 1.5.

Chapter 2:

SURFACE QG VORTICES

2.1 Introduction

This chapter contains a study of vortices in the surface QG system. By the term vortex we mean a localised region of strongly rotational flow, or the associated surface temperature anomaly. The full 3-dimensional velocity field induced by such a temperature distribution will be strongest near the surface and decay roughly exponentially with height, so surface QG vortices (more accurately, their real-world, non-QG counterparts) are sometimes referred to as 'surface enhanced' vortices when they occur in the atmosphere.

Our motivation for studying surface QG vortices is two-fold. Firstly, vortices commonly form in all of the physical situations to which the equations have been applied so an understanding of their behaviour is of strong interest. Secondly, the concept of vortices forms a fundamental building block of understanding in non-linear fluid dynamical systems, and surface QG is no exception. Here we investigate some fundamental properties of surface QG vortices and compare them to their 2-d Euler counterparts; this field of study proves a fruitful source of interesting comparisons, thereby making good progress on the first key question of the Introduction: what are the key differences between surface QG dynamics and 2-d Euler?

To set the scene, and outline the boundaries of current knowledge, we briefly discuss two recent papers on the subject of surface QG vortices in Section 2.2. In fact, before the work of this chapter was published, these were the only two published papers on the subject and they both consider vortices with smooth temperature profiles. The bulk of the original work in this chapter (Sections 2.3 and 2.4), in contrast, concerns vortices with piecewise uniform temperature profiles. That is, vortices formed by summing together circular patches of uniform temperature. This is the first time this approach has been used. It turns out to be very useful because it allows for the first time an analytic treatment of the problem of surface QG vortex stability.

The central result is that of Section 2.3 where we derive the dispersion relation for disturbances to a single 'surface Rankine vortex', by which we mean, a circular patch of uniform temperature. The surface Rankine vortex is analogous to the Rankine vortex of 2-d Euler dynamics which consists of a circular patch of uniform vorticity (see Saffman (1995)). The dispersion relation is important because it provides a global example of wave propagation on a temperature front in surface QG dynamics, something which is not possible on a straight temperature front (as discussed previously, see Section 1.3.3), and therefore helps answer the second question posed in the Introduction chapter: what are the properties of waves propagating on surface temperature fronts? It is also the direct analogue of a famous 2-d Euler result, the propagation of disturbances on the 2-d Euler Rankine vortex. Finally, the simple result of this section provides a basic building block for analysing the stability of more complicated vortices constructed from multiple superimposed patches. In Section 2.4, we present an analytic treatment of the stability of 'shielded surface Rankine vortices', that is, two superposed surface Rankine vortices – the simplest possible unstable surface QG vortex. The results are then compared directly to the previous vortex studies.

First we include two short subsections introducing surface QG dynamics in cylindrical polar coordinates. The first derives expressions for the surface QG inversion operator in cylindrical polar coordinates. The other presents novel proofs of stability conditions for circular vortices which are referred to later in the chapter.

2.1.1 Surface QG inversion in polar coordinates

To express the surface QG inversion operator in cylindrical polar coordinates we expand the temperature field in terms of Bessel functions of the first kind, that is, we use a Hankel transform. The Bessel functions of the first kind, denoted J_n, form separable solutions to the three-dimensional Laplace equation with cylindrical symmetry since they satisfy

$$\nabla^2(\mathrm{J}_n(kr)\mathrm{e}^{in\varphi-kz}) = 0, \tag{2.1}$$

where (r, φ, z) are the usual cylindrical coordinates, k is a positive real number representing the radial wavenumber and n is an integer label of the azimuthal modes. Therefore, if the surface temperature field is written as

$$\theta(r, \varphi) = \sum_{n=-\infty}^{\infty} \int_0^\infty \hat{\theta}(k, n)\mathrm{J}_n(kr)\mathrm{e}^{in\varphi}k\,dk, \tag{2.2}$$

then the full three-dimensional temperature field is recovered by multiplying the integrand by e^{-kz}. From the fact that $\theta = \psi_z$, the corresponding surface streamfunction therefore has the form

$$\psi(r,\varphi) = \sum_{n=-\infty}^{\infty} \int_0^{\infty} \left(\frac{-\hat{\theta}(k,n)}{k} \right) \mathrm{J}_n(kr) \mathrm{e}^{\mathrm{i}n\varphi} k\, dk. \tag{2.3}$$

Comparing (2.2) and (2.3) we see that the inversion has the familiar form of the spectral space surface QG inversion (see (1.26)), $\hat{\psi} = -\hat{\theta}/k$. The inverse of the transform in (2.2) is given by

$$\hat{\theta}(k,n) = \frac{1}{2\pi} \int_0^{\infty} \int_0^{2\pi} \theta(s,\varphi') \mathrm{J}_n(ks) \mathrm{e}^{-\mathrm{i}n\varphi'} s\, d\varphi'\, ds, \tag{2.4}$$

as can be checked using the Bessel function orthogonality relation $\int_0^{\infty} \mathrm{J}_n(ks)\mathrm{J}_n(kr) k\, dk = \delta(r-s)/r$ (Gradshteyn & Ryzhic (2000)).

From (2.2) and (2.3) we see that the special case of a radially symmetric temperature profile (i.e. a circular vortex) has inversion given by

$$\psi(r) = -\int_0^{\infty} \int_0^{\infty} \theta(s) \mathrm{J}_0(ks) \mathrm{J}_0(kr) s\, \mathrm{d}s\, \mathrm{d}k, \tag{2.5}$$

or, in terms of the azimuthal velocity field $u = \partial\psi/\partial r$,

$$u(r) = \int_0^{\infty} \int_0^{\infty} \theta(s) \mathrm{J}_0(ks) \mathrm{J}_1(kr) ks\, \mathrm{d}s\, \mathrm{d}k, \tag{2.6}$$

where the relation $\mathrm{J}_0'(\kappa) = -\mathrm{J}_1(\kappa)$ has been used. This, then, is arguably a radial analogue of the Hilbert transform (which was introduced in Section 1.3.1), a comparison which can be made more direct by writing (2.6) in the form

$$u(r) = \int_0^{\infty} \theta(s) \mathrm{F}(r/s) \frac{\mathrm{d}s}{s} \tag{2.7}$$

where the function $\mathrm{F}(r/s) = \int_0^{\infty} \mathrm{J}_0(\kappa)\mathrm{J}_1(\kappa r/s)\kappa\, \mathrm{d}\kappa$ replaces $|1 - y/y'|^{-1}$ in the standard Hilbert transform of (1.23).

2.1.2 Stability conditions

This second short introductory subsection presents a novel derivation for the surface QG analogue of the Rayleigh condition which we use later in the chapter. We also briefly comment on the use of the Fjortoft condition in surface QG dynamics.

The Rayleigh condition. The most basic vortex stability theorem, the radial Rayleigh condition, carries over straightforwardly from 2-d Euler to surface QG: a circular vortex with temperature profile

$$\theta = \Theta(r) \tag{2.8}$$

is stable to linear perturbations if $\mathrm{d}\Theta/\mathrm{d}r$ takes only one sign throughout the domain. This result was derived by Carton (2009) by linearising the advection equation about small temperature perturbations, a process which assumes a smooth background temperature distribution. In this chapter we apply the condition to discontinuous temperature profiles so we present here a more general derivation applicable to the discontinuous case.

Instead of linearising about small temperature variations we linearise about small displacements of material contours. The method follows closely that of Dritschel (1988b) who considers the corresponding 2-d Euler problem. We start by recalling that the following quantity is conserved by the surface QG equations,

$$J = \frac{1}{2} \iint r^2 \theta \,\mathrm{d}A \tag{2.9}$$

Physically, J is the angular momentum of the full 3-dimensional flow field. From a Hamiltonian dynamics point of view (see Shepherd (2003)), conserved quantities are related to symmetries (Noether's theorem) and then also to stability theorems for basic states which share the same symmetry property. The angular momentum constraint is associated with rotational symmetry, and then also the Rayleigh stability condition for circular vortices.

With this observation in mind, we prove the Rayleigh condition directly from the constraint of (2.9). Consider the setup of Figure 2.1(a). That is, a vortex constructed from

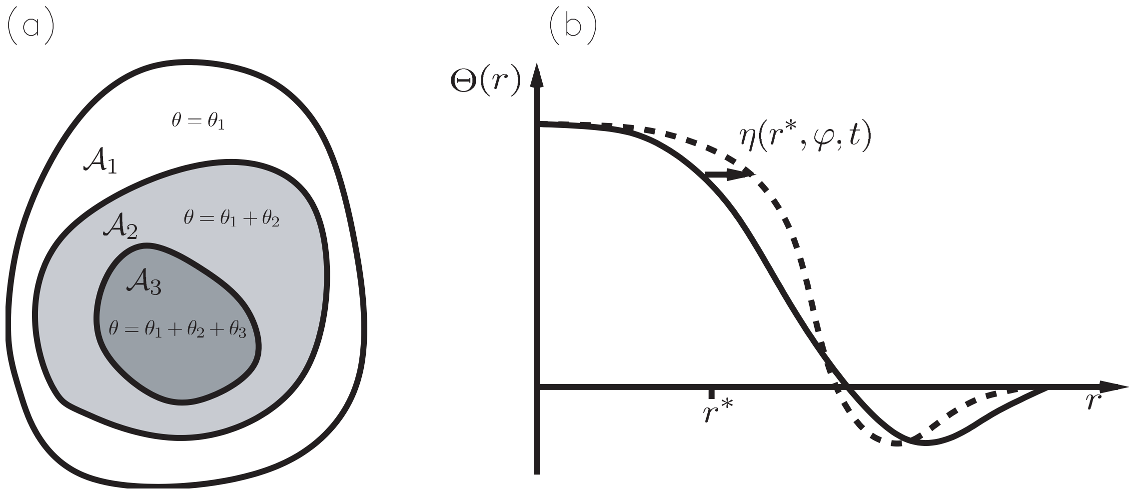

Figure 2.1 (a) Sketch of a piecewise uniform vortex (b) Sketch of a smooth vortex with perturbation.

concentric patches of uniform temperature,

$$\theta = \sum_i \mathcal{H}(\mathcal{A}_i)\theta_i, \tag{2.10}$$

where

$$\mathcal{H}(\mathcal{A}_i) = \begin{cases} 1 & \text{inside } \mathcal{A}_i \\ 0 & \text{outside } \mathcal{A}_i \end{cases} \tag{2.11}$$

is like the Heaviside step function, being equal to one within the region $\mathcal{A}_i$ and zero elsewhere. The angular momentum of (2.9) then reduces to

$$J = \frac{1}{2}\sum_i \left[\theta_i \iint_{\mathcal{A}_i} r^2 \,\mathrm{d}A\right], \tag{2.12}$$

and on assuming each region to be near-circular, by writing the boundaries of $\mathcal{A}_i$ as $r = a_i + \eta_i(\varphi, t)$, the integrals in (2.12) become

$$\begin{aligned} \iint_{\mathcal{A}_i} r^2 \,\mathrm{d}A &= \int_0^{2\pi}\int_0^{a_i+\eta_i} r^3 \,\mathrm{d}r\,\mathrm{d}\varphi & (2.13)\\ &= \int_0^{2\pi} \frac{(a_i+\eta_i)^4}{4}\,\mathrm{d}\varphi. & (2.14) \end{aligned}$$

We also require the condition of area conservation for each patch. That is, the constraint that

$$\begin{aligned} A_i &= \int_0^{2\pi}\int_0^{a_i+\eta_i} \mathrm{d}A & (2.15)\\ &= \pi a_i^2 + a_i\int_0^{2\pi}\eta_i\,\mathrm{d}\varphi + \frac{1}{2}\int_0^{2\pi}\eta_i^2\,\mathrm{d}\varphi & (2.16) \end{aligned}$$

must remain equal to πa_i^2. Therefore, the integral of η_i around the patch boundary is in fact $\mathcal{O}(\eta_i^2)$:

$$\int_0^{2\pi}\eta_i\,\mathrm{d}\varphi = -\frac{1}{2a_i}\int_0^{2\pi}\eta_i^2\,\mathrm{d}\varphi. \tag{2.17}$$

Expanding (2.14) and using this relation gives

$$\begin{aligned} J &= \frac{1}{2}\sum_i\theta_i\int_0^{2\pi}\left(\frac{a_i^4}{4} + a_i^3\eta_i + \frac{3}{2}a_i^2\eta_i^2 + a_i\eta_i^3 + \frac{\eta_i^4}{4}\right)\mathrm{d}\varphi & (2.18)\\ &= \frac{\pi}{4}\sum_i\theta_i a_i^4 + \sum_i\theta_i a_i^2\int_0^{2\pi}\eta_i^2\left(1 + \frac{\eta_i}{a_i} + \frac{\eta_i^2}{4a_i^2}\right)\mathrm{d}\varphi & (2.19)\\ &= \frac{\pi}{4}\sum_i\theta_i a_i^4 + \sum_i\theta_i a_i^2\int_0^{2\pi}\eta_i^2\left(1 + \frac{\eta_i}{2a_i}\right)^2\mathrm{d}\varphi. & (2.20) \end{aligned}$$

The first term of (2.20) is just the angular momentum of the basic state. The second term is the perturbation component; because J is a constant of motion (2.20) provides a constraint on the evolution of the perturbation. We note in passing that (2.20) is equivalent to the result of Dritschel (1988b) who instead uses an area-like perturbation quantity.

In that case, the term in parentheses in (2.20) reduces to unity, and the constraint is simply quadratic in the perturbation quantity. The fact that all of the integrals are positive means that the constraint is stronger if the θ_i all take the same sign since then each integral is bounded:

$$\int_0^{2\pi} \eta_j^2 \left(1 + \frac{\eta_j}{2a_j}\right)^2 \mathrm{d}\varphi \leq \frac{J - \frac{\pi}{2}\sum_i \theta_i a_i^4}{\theta_j a_j^2} \tag{2.21}$$

for all j. To interpret this bound, note from (2.20) that each patch contributes separately to the angular momentum J (as expected, it is a linear functional of the temperature field), but that angular momentum can also be transferred between the different perturbations. The bounding value in (2.21) is achieved when all of the disturbance angular momentum is moved into the j-th perturbation.

A more intuitive, but less stringent, bound follows from (2.21). Since, by definition, $\eta_i > -a_i$ for all i, the term in parentheses is bounded below by $1/2$ so we can write

$$\int_0^{2\pi} \eta_j^2 \,\mathrm{d}\varphi < 4\frac{J - \frac{\pi}{2}\sum_i \theta_i a_i^4}{\theta_j a_j^2}. \tag{2.22}$$

Clearly there can be no exponentially growing normal modes in the linear dynamics which satisfy this constraint. We therefore arrive at the Rayleigh condition: a piecewise uniform circular vortex is stable to linear perturbations if all of the temperature jumps are of the same sign.

For completeness, we also derive the condition for smooth temperature profiles using the same method. For the 2-d Euler case Dritschel (1988b) simply states that a smooth profile is equivalent to the limit of summing many weak vorticity patches and so the result follows immediately. This inference is not as obvious in the surface QG case since the velocity field induced by a temperature discontinuity is always singular, no matter how weak the patch is. Therefore we derive the result directly.

Consider a smooth radially symmetric basic state $\theta = \Theta(r)$ (see Figure 2.1(b) for an example profile). Now consider applying a perturbation to the vortex such that the contour $r = r^*$ is moved to the new position

$$r = r^* + \eta(r^*, \varphi, t) \tag{2.23}$$

(note that the discrete subscript i from above has become the continuous variable r^* here), and the new temperature distribution is given by

$$\theta = \Theta(r^*). \tag{2.24}$$

On substituting both of these expressions into (2.9) we obtain

$$\begin{aligned} J &= \frac{1}{2}\int_0^{2\pi}\int_0^{\infty}(r^*+\eta(r^*))^3\Theta(r^*)\left(1+\frac{\partial\eta}{\partial r}(r^*)\right)\mathrm{d}r^*\,\mathrm{d}\varphi && (2.25)\\ &= -\frac{1}{2}\int_0^{2\pi}\int_0^{\infty}\frac{(r^*+\eta(r^*))^4}{4}\frac{\mathrm{d}\Theta}{\mathrm{d}r}(r^*)\,\mathrm{d}r^* && (2.26)\end{aligned}$$

where we have integrated by parts and omitted the φ and t dependence of η for ease of reading. This can be expanded, as in (2.18), and the $\mathcal{O}(\eta)$ term converted to an $\mathcal{O}(\eta^2)$ term, as in (2.19), resulting in the following exact expression for J:

$$J = \frac{1}{2}\iint r^2\Theta(r)\,\mathrm{d}A - \frac{1}{2}\int_0^{\infty} r^{*2}\frac{\mathrm{d}\Theta}{\mathrm{d}r}(r^*)\left(\int_0^{2\pi}\eta^2(r^*)\left(1+\frac{\eta(r^*)}{2r^*}\right)^2\mathrm{d}\varphi\right)\mathrm{d}r^*. \qquad (2.27)$$

This should be compared to (2.20). The minus sign here arises because a positive θ_i in the piecewise uniform case corresponds to a negative $\mathrm{d}\Theta/\mathrm{d}r$ here. Other than that the expressions are the same and we can draw the same conclusions as before.

The Fjortoft condition. The next most basic stability theorem, the Fjortoft condition, can also be applied to the surface QG system. However, it is only useful for smooth temperature profiles, as we discuss below. Carton (2009) provides a derivation for smooth profiles, the result being that a smooth temperature distribution $\theta = \Theta(r)$ is stable to linear perturbations if

$$(U(r)-\Omega r)\frac{\mathrm{d}\Theta}{\mathrm{d}r} > 0 \qquad (2.28)$$

throughout the domain, where $U(r)$ is the basic state azimuthal velocity field and Ωr an arbitrary solid body rotation field. As for the 2-d Euler case, an optimal choice is $\Omega_s = U(r_s)/r_s$ where r_s is the location of the stationary point required by the Rayleigh condition: $\mathrm{d}\Theta/\mathrm{d}r(r_s) = 0$. Note that in this form the condition is only a necessary condition for instability to be possible: a vortex must contain a point where, in the appropriate frame of reference, U is anti-correlated with Θ_r.

That this condition is not useful for discontinuous temperature profiles is clear from (2.28): any temperature discontinuity induces a singular velocity field in the direction which violates (2.28). Therefore the condition is not met for any finite value of Ω. In other words, this condition cannot ever rule out the possibility of instability. The inapplicability of the Fjortoft condition to discontinuous temperature profiles is an interesting qualitative difference between the surface QG and 2-d Euler systems which will be mentioned several times throughout the thesis.

We show later in Section 2.4 (see Figure 2.7) that there are indeed vortices that are stable despite not satisfying (2.28). Whether or not a more useful stability condition can be derived for discontinuous profiles is still an open question.

2.2 Previous studies

There are currently only two published studies examining the behaviour of vortices in the surface QG system[1]. Here we briefly review each in turn. In the first, Dritschel (2011), an exact steadily rotating vortex with an elliptical shape of non-uniform cross section is described. This solution is particularly interesting because the velocity field is linear within the vortex, like that of the 2-d Euler Kirchoff vortex. In the second, Carton (2009), the stability characteristics of a family of circular vortex profiles are obtained numerically. Recall from the previous section that unstable vortices must contain regions of opposing temperature gradients and indeed this is the case for the family of vortices considered.

The purpose of this section within the context of the thesis is primarily to outline the current boundaries of knowledge by exploring two recent papers on the subject, but in addition to this some results from each paper are referred to later in the chapter.

The ellipsoid solution. The main result of Dritschel (2011), the derivation of an exact steadily rotating solution to the surface QG equations, is presented by analogy to a well known result from unbounded 3-d QG dynamics. The result used is that an ellipsoid of uniform QGPV,

$$q = \begin{cases} q_0 & \text{for } \left(\frac{x}{a}\right)^2 + \left(\frac{y}{b}\right)^2 + \left(\frac{z}{c}\right)^2 < 1 \\ 0 & \text{otherwise,} \end{cases} \tag{2.29}$$

is itself a steadily rotating vortex (see Zhmur & Shchepetkin (1991) and Meacham (1992) as well as further references in Dritschel (2011)). Dritschel takes the limit $c \to 0$ whilst keeping cq_0 fixed which, in an analogous fashion to the description of Section 1.3.1, gives a solution to the surface QG equations. The resulting temperature distribution is not uniform, but instead takes the profile of a lens-shaped squashed ellipsoid:

$$\theta = \begin{cases} \theta_0 \sqrt{1 - (x/a)^2 - (y/b)^2} & \text{for } \left(\frac{x}{a}\right)^2 + \left(\frac{y}{b}\right)^2 < 1 \\ 0 & \text{otherwise,} \end{cases} \tag{2.30}$$

where $\theta_0 = 2cq_0$. The alternative limit discussed in Section 1.3.1 can also be performed to (2.29), $c \to \infty$ with q_0 fixed, and this results in a steadily rotating elliptic patch of uniform vorticity – the famous 2-d Euler Kirchoff vortex (see Lamb (1932) for a derivation in English). A remarkable feature of the original solution (2.29) is that the induced velocity field is linear within the boundary of the potential vorticity anomaly, and this result is preserved under both of these limits.

---

[1] Excluding the two papers resulting form the work of this chapter.

The precise form of the velocity field and the rotation rate for the surface QG vortex (2.30) is calculated analytically by Dritschel (2011) in terms of complete elliptic integrals. The details of the calculation are not needed here, but Figure 2.2 serves to illustrate the results. Shown in panel (a) are the rotation rates as a function of the vortex aspect ratios $\lambda = b/a$ for both the ellipsoid vortex, (2.30), and the 2-d Euler Kirchoff vortex. Shown in panel (b) are the azimuthal velocity fields for the circular cases (i.e. $\lambda = 1$). For λ close to one the ellipse shapes can be interpreted as mode 2 disturbances on a radially symmetric mean flow. The figure shows that for both vortices the disturbances rotate at a slower speed than individual fluid particles at the vortex boundary, indicating that the disturbances propagate against the mean flow, an effect which is more pronounced in the surface QG case. Panel (b) also illustrates the faster decay of the velocity field with r in the surface QG case, like $1/r^2$ compared to the $1/r$ decay in 2-d Euler.

Shielded vortices The study of Carton (2009) is of a different nature. The stability of the following family of circular temperature distributions is investigated numerically:

$$\theta = \Theta(r) \equiv \Theta_0 \left(1 - \frac{\alpha}{2}\left(\frac{r}{a}\right)^{\alpha}\right) e^{-(r/a)^{\alpha}}. \tag{2.31}$$

Here α is a positive parameter and Θ_0 a normalisation factor such that the induced velocity field $u(r)$ satisfies $\max(u) = u_0$. These vortices consist of a central region of positive temperature anomaly surrounded by an annulus of negative temperature anomaly. Some examples are plotted later in the chapter as Figure 2.10 which also shows that the larger α profiles have 'deeper' and narrower shielding annuli.

The presence of the annuli are important since they provide the regions of opposing temperature gradient required by the Rayleigh stability criterion of the previous section. The condition is only necessary for instability, not sufficient, and indeed the study shows that the vortices are stable for some α values.

Figure 2.3 is one of the main results of the study. Shown are numerically-obtained growth rates of wavenumber $n = 2, 3$ and 4 disturbances. It appears that the vortices are stable for $\alpha < 2$ with successively higher modes becoming unstable as α is increased above this value. In addition, as far as the data shows, the most unstable mode increases as α is increased.

The vortices used in this study, (2.31), are 'completely shielded' by which we mean $\int_0^\infty \theta r \, \mathrm{d}r = 0$. This constraint means the velocity field decays quickly at large r: like r^{-3} instead of the usual r^{-2} for not-completely-shielded surface QG vortices. The motivation for this approach comes from earlier studies in the 2-d Euler system. In that case, an

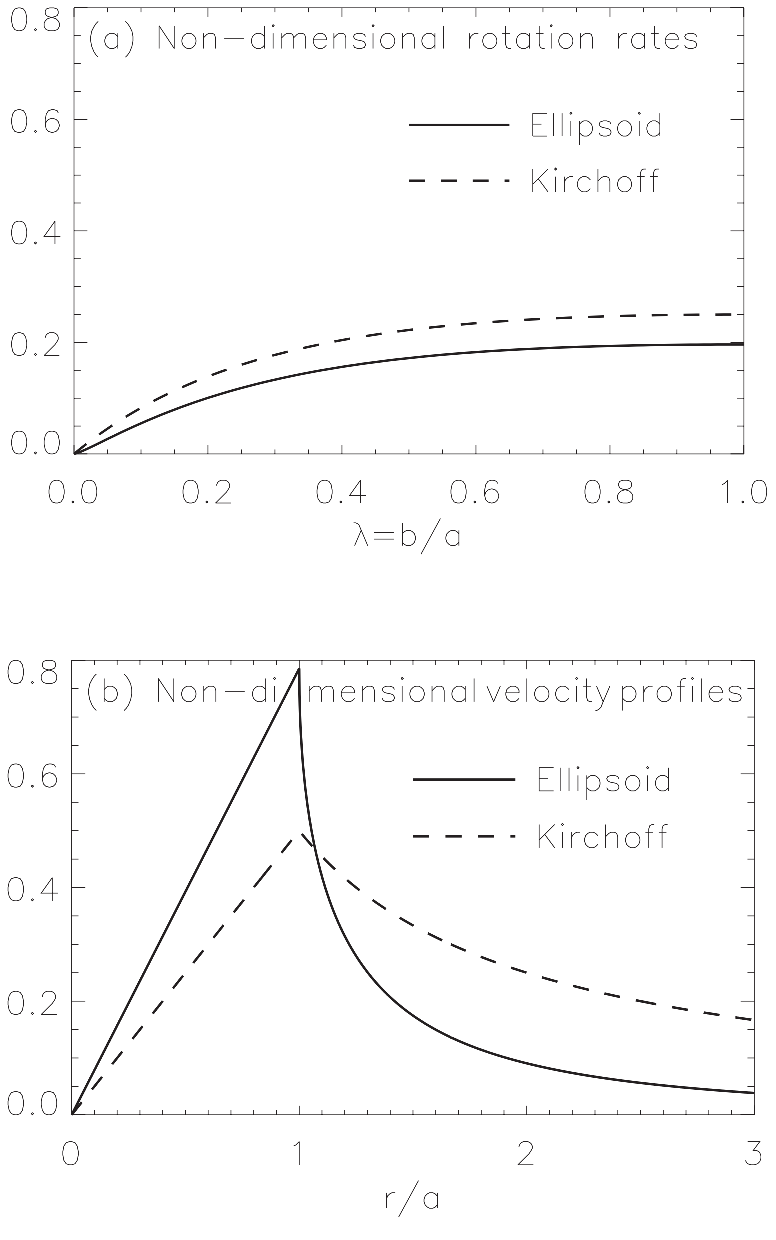

Figure 2.2 Panel (a): Rotation rates for the surface QG ellipsoid vortex (scaled by $\theta_0/\sqrt{ab}$) and 2-d Euler Kirchoff vortex (scaled by q_0) as a function of $\lambda = b/a$, a measure of the aspect ratio. Panel (b): Velocity profiles for the corresponding circular vortices with $b = a$.

isolated vortex which is not completely shielded induces a velocity field with infinite kinetic energy (the velocity decays as r^{-1} so $KE \propto \iint U^2\,\mathrm{d}A \sim \int r^{-1}\,\mathrm{d}r \sim \infty$) which is not physical. However, an unshielded surface QG vortex has finite energy (both full 3-dimensional total energy and surface-integrated kinetic energy) due to the more local Green's function, so this study has scope for extension to the not-completely-shielded regime.

Another comment on this study regards the choice of scaling used. As explained above, the growth rates of the instability are scaled by the peak basic state velocity value. Although this provides a straight forward way to compare different vortices it is perhaps not the most insightful. As we discuss later, peak velocity values in surface QG are not robust statistics with respect to wave propagation and instabilities.

2.3 The surface Rankine vortex[2]

In this section we derive analytically the dispersion relation for linear perturbations to a 'surface Rankine vortex'. That is, a circular patch of uniform temperature evolving under

---

[2] The work of this section is published in Harvey & Ambaum (2011)

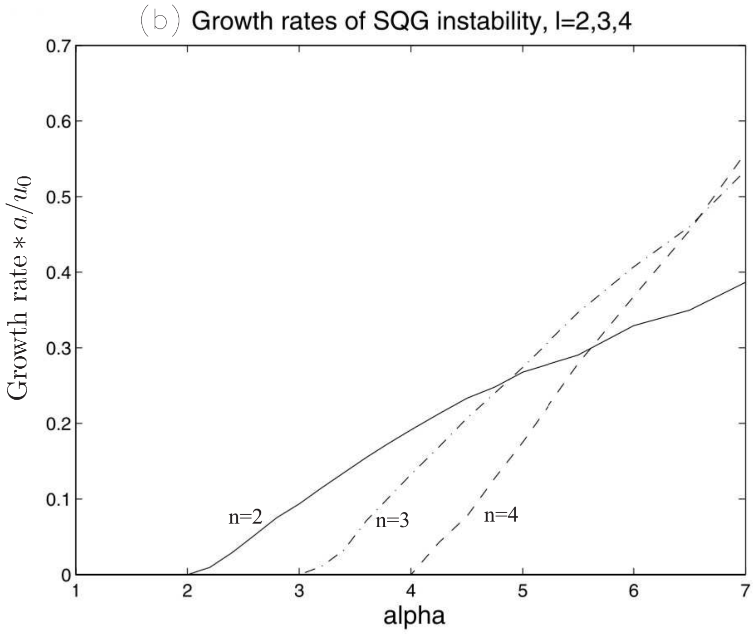

Figure 2.3 Numerically obtained growth rates as a function of α for the vortex profiles of (2.31). The disturbance wavenumbers are as shown (figure taken from Carton (2009)).

the surface QG equations. The dispersion relation is analysed in detail and compared to the more familiar dispersion relation for a perturbed 2-d Euler Rankine vortex. The dispersion relation is also successfully verified against numerical simulations of the full equations.

2.3.1 The basic state

We write the temperature distribution for the basic state as

$$\theta = \Theta(r) \equiv \begin{cases} \theta_0 & r < a \\ 0 & r > a \end{cases} \tag{2.32}$$

where r is the radial coordinate. That such a patch is stable, and therefore supports neutral perturbations, follows from the stability condition of (2.21): applied to a single patch, the condition reduces to the statement

$$\int_0^{2\pi} \eta^2 \left(1 + \frac{\eta}{2a}\right)^2 \mathrm{d}\varphi = \text{constant}. \tag{2.33}$$

We now use the polar coordinate form of the surface QG inversion operator described in Section 2.1.1 to invert the basic state (2.32). Substituting for Θ from (2.32) into (2.5) and using the relation $\kappa \mathrm{J}_0(\kappa) = (\kappa \mathrm{J}_1(\kappa))'$ gives the basic state streamfunction

$$\Psi(r) = -\theta_0 a \int_0^\infty \frac{\mathrm{J}_1(ka)}{k} \mathrm{J}_0(kr)\, dk, \tag{2.34}$$

and the corresponding basic state azimuthal velocity field, $U(r) = \partial\Psi/\partial r$, is

$$U(r) = \theta_0 \int_0^\infty \mathrm{J}_1(\kappa)\mathrm{J}_1(\kappa r/a)\, d\kappa, \tag{2.35}$$

where we have substituted $\kappa = ka$ and used a further relation, $\mathrm{J}_0'(\kappa) = -\mathrm{J}_1(\kappa)$. We now introduce the notation

$$\mathrm{E}_n(r/a) \equiv \int_0^\infty \mathrm{J}_n(\kappa)\mathrm{J}_n(\kappa r/a)\, d\kappa, \tag{2.36}$$

so that the function E_1 is proportional to the basic state azimuthal velocity field,

$$U(r) = \theta_0 \mathrm{E}_1(r/a). \tag{2.37}$$

The higher order E_n are used below to describe perturbation quantities. Figure 2.4(a) shows plots of the functions E_n for various n.

We derive some asymptotic results for the function E_1 in Appendix B. We show that the singularity in U at $r = a$ takes the form

$$U(r) \sim \frac{\theta_0}{\pi}(-\log|1 - (r/a)^2| + 4\log 2 - 2) \tag{2.38}$$

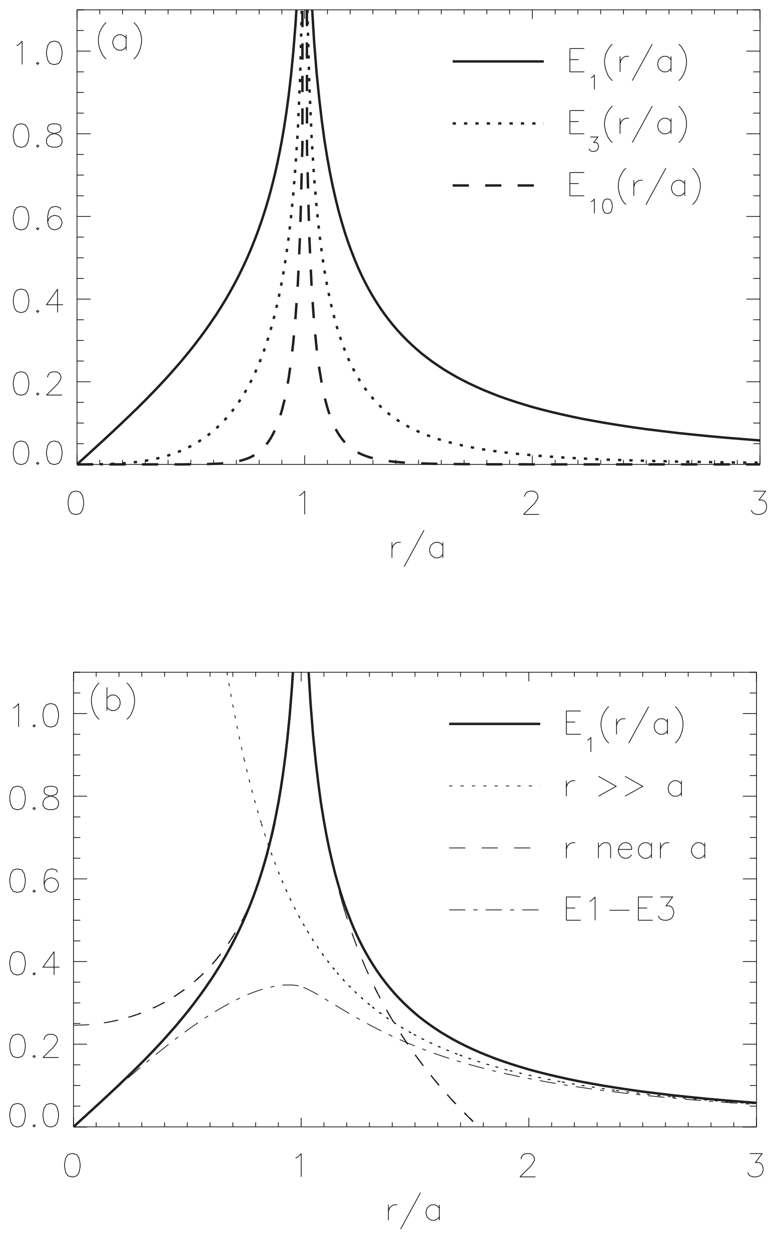

Figure 2.4 Panel (a): Examples of the functions E_n. The solid line, E_1, is proportional to the basic state velocity profile, see (2.35). The cases $n > 1$ are proportional to the perturbation streamfunction of a mode n disturbance, see (2.54). Panel (b): The dashed line is the asymptotic result for $|r/a - 1| \ll 1$ of (2.38) and the dotted line is the asymptotic result for $r \gg a$ of (2.39). Finally, the dot-dash line shows $E_1 - E_3$, see (2.56) and Appendix B, to illustrate that this combination if finite in the limit $r \to a$.

and this is consistent with the observation of Section 1.3.3 that θ discontinuities induce velocity fields with logarithmic singularities under surface QG inversion. We also show in Appendix B that for $r \gg a$,

$$U(r) \sim \frac{\theta_0 a^2}{2r^2} \tag{2.39}$$

which is consistent with the form of the surface QG Green's function, $G(\mathbf{x}) = -(2\pi|\mathbf{x}|)^{-1}$. Both of these asymptotic fits are plotted in Figure 2.4(b).

2.3.2 The dispersion relation

We now derive the dispersion relation for perturbations to the patch boundary using two different methods. The first, the contour dynamics method, provides an equation for the full nonlinear evolution of the patch which we then linearise. The second, which we call the direct method, involves linearising the system before applying the evolution equation. This second method is simpler to apply and we use it throughout the rest of the thesis. The first method is more comprehensive since it gives an equation for the full nonlinear evolution of the system.

Suppose the patch boundary is moved to the new position

$$r = r_1(\varphi, t) \equiv a + \eta(\varphi, t), \tag{2.40}$$

with $\eta \ll a$. We obtain the dispersion relation by considering the condition of material advection of this boundary, which is expressed formally as

$$\frac{Dr_1}{Dt} \equiv \frac{\partial r_1}{\partial t} + \frac{u_\varphi}{r_1}\frac{\partial r_1}{\partial \varphi} = u_r \tag{2.41}$$

where u_r and u_φ are the radial and azimuthal components of the velocity field evaluated at $r = r_1$. However, u_φ and u_r are both generally infinite at the boundary so (2.41) cannot be used directly. To get around this we apply it not to the contour $r = r_1$ but instead to the contour $r = r_1 + \epsilon$, that is, away from the boundary where each term is finite, and then take the limit $\epsilon \to 0$. The two advective terms become infinite but the combination in (2.41) remains finite leaving evolution of the boundary on finite time scales.

The contour dynamics method. The so-called 'contour dynamics' formula provides an integral representation of the velocity field for piecewise uniform temperature distributions. For the set-up of (2.40) a single patch defined by the closed boundary $\mathcal{C}$, the result is

$$\begin{pmatrix} u_x(\mathbf{x}) \\ u_y(\mathbf{x}) \end{pmatrix} = \theta_0 \oint_{\mathcal{C}} \mathrm{G}(|\mathbf{x} - \mathbf{x}'|) \begin{pmatrix} \mathrm{d}x' \\ \mathrm{d}y' \end{pmatrix} \tag{2.42}$$

with $G(|\mathbf{x}|) = -(2\pi|\mathbf{x}|)^{-1}$ the surface QG Green's function and u_x, u_y the velocity field in Cartesian coordinates (see Zabusky et al. (1979) or Pullin (1992) for a derivation of the contour dynamics formula). We will integrate around the contour $r' = a + \eta(\varphi')$ with $\mathbf{x}$ fixed at the arbitrary position (r, φ). With this in mind we write

$$\begin{pmatrix} \mathrm{d}x' \\ \mathrm{d}y' \end{pmatrix} = \frac{\partial}{\partial \varphi'} \left[(a + \eta(\varphi')) \begin{pmatrix} \cos\varphi' \\ \sin\varphi' \end{pmatrix} \right] \mathrm{d}\varphi' \tag{2.43}$$

and recall that $u_r = u_x \cos\varphi + u_y \sin\varphi$ and $u_\varphi = -u_x \sin\varphi + u_y \cos\varphi$. Therefore the polar coordinate form of the contour dynamics formula can be written

$$\begin{pmatrix} u_r(r,\varphi) \\ u_\varphi(r,\varphi) \end{pmatrix} = \theta_0 \int_0^{2\pi} G(|\mathbf{x} - \mathbf{x}'|) \frac{\partial}{\partial \varphi'} \left[(a + \eta(\varphi')) \begin{pmatrix} \cos(\varphi - \varphi') \\ -\sin(\varphi - \varphi') \end{pmatrix} \right] \mathrm{d}\varphi' \tag{2.44}$$

Note that both of these integrals are infinite if $\mathbf{x}$ lies on the patch boundary. As suggested above we instead take $\mathbf{x}$ to be given by $r = a + \eta(\varphi) + \epsilon$. Then, on substituting these expressions into the evolution equation (2.41), and then taking $\epsilon \to 0$ we obtain an expression for the full un-approximated evolution of the patch boundary:

$$\begin{aligned} \frac{\partial \eta}{\partial t} = -\frac{\theta_0}{2\pi} \int_0^{2\pi} \frac{1}{|\mathbf{x} - \mathbf{x}'|} \frac{\partial}{\partial \varphi'} \Big[(a + \eta(\varphi')) \Big(& \cos(\varphi - \varphi') \\ & + \frac{1}{a + \eta(\varphi)} \frac{\partial \eta}{\partial \varphi}(\varphi) \sin(\varphi - \varphi') \Big) \Big] \mathrm{d}\varphi'. \end{aligned} \tag{2.45}$$

To linearise this for small η / a note that

$$\begin{aligned} |\mathbf{x} - \mathbf{x}'|^2 &= r^2 + r'^2 - 2rr' \cos(\varphi - \varphi') & (2.46) \\ &= 4a^2 \left(1 + \frac{\eta(\varphi) + \eta(\varphi')}{a} \right) \sin^2\left(\frac{\varphi - \varphi'}{2} \right) + \mathcal{O}\left(\frac{\eta}{a} \right)^2 & (2.47) \end{aligned}$$

so

$$\frac{1}{|\mathbf{x} - \mathbf{x}'|} \sim \frac{1}{2a \left| \sin\left(\frac{\varphi - \varphi'}{2} \right) \right|} \left(1 - \frac{\eta(\varphi) + \eta(\varphi')}{2a} \right). \tag{2.48}$$

Substituting this into (2.45) and keeping only $\mathcal{O}(\eta/a)$ terms gives the linear evolution of the patch boundary:

$$\begin{aligned} \frac{\partial \eta}{\partial t} = -\frac{\theta_0}{4\pi a} \int_0^{2\pi} \frac{1}{\left| \sin\left(\frac{\varphi - \varphi'}{2} \right) \right|} \Big[& \left(\frac{\partial \eta}{\partial \varphi}(\varphi') - \frac{\partial \eta}{\partial \varphi}(\varphi) \right) \cos(\varphi' - \varphi) \\ & + \frac{1}{2} (\eta(\varphi') - \eta(\varphi)) \sin(\varphi - \varphi') \Big] \mathrm{d}\varphi'. \end{aligned} \tag{2.49}$$

The dispersion relation is obtained by substituting $\eta \propto e^{i(n\varphi - \omega_n t)}$ and evaluating the integral. However, this calculation is omitted here for brevity. A more elegant method is presented below, the result being given by (2.67).

The direct method. For the second method we jump straight to the linear version of the dynamics. This means we miss the nonlinear evolution equation that the contour dynamics method gives us (equation (2.45)), but the method is far simpler to apply and is what we use throughout the rest of the thesis in a number of different setups. The linear version of the evolution equation (2.41) is

$$\frac{\partial \eta}{\partial t} = \lim_{r \to a} \left(u_r' - \frac{U(r)}{a} \frac{\partial \eta}{\partial \varphi} \right), \tag{2.50}$$

where $U(r)$ is the basic state velocity of (2.37) and u_r' is the radial velocity field linearised about small η. This can be calculated by approximating the perturbation temperature distribution as a δ-function located at $r = a$. That is, by inverting

$$\theta(r, \varphi, t) = \Theta(r) + \theta_0 \eta(\varphi, t) \delta(r - a) \tag{2.51}$$

where $\Theta(r)$ is the basic state patch profile of (2.32).

We invert the perturbation part of (2.51) using the transform (2.2). For each azimuthal mode, that is $\eta = a\hat{\eta}(t)\mathrm{e}^{\mathrm{i}n\varphi}$, the transform of the final term in (2.51) takes the form

$$\eta(\varphi, t)\delta(r - a) = a\hat{\eta}(t)\mathrm{e}^{\mathrm{i}n\varphi} \int_0^\infty \hat{\delta}(k) \mathrm{J}_n(kr) k \, dk \tag{2.52}$$

where $\hat{\delta}(k)$ is given by (2.4)

$$\hat{\delta}(k) = \int_0^\infty \delta(s - a) \mathrm{J}_n(ks) s \, ds = a\mathrm{J}_n(ka). \tag{2.53}$$

The induced perturbation streamfunction is therefore

$$\psi(r, \varphi, t) = -\theta_0 a \hat{\eta}(t) e^{in\varphi} \int_0^\infty \mathrm{J}_n(\kappa) \mathrm{J}_n(\kappa r / a) \, d\kappa = -\theta_0 \hat{\eta}(t) e^{in\varphi} \mathrm{E}_n(r/a), \tag{2.54}$$

using the notation introduced in (2.36), and the corresponding perturbation radial velocity field, $u_r' = -r^{-1}\partial\psi/\partial\varphi$, is given by

$$u_r'(r, \varphi) = \frac{\mathrm{i}n}{r} \theta_0 a \hat{\eta}(t) \mathrm{E}_n(r/a) \mathrm{e}^{\mathrm{i}n\varphi}. \tag{2.55}$$

Finally, we substitute for U and u_r' in (2.50) and put $\hat{\eta}(t) \propto \mathrm{e}^{-\mathrm{i}\omega_n t}$ to give

$$\omega_n = \frac{\theta_0 n}{a} \lim_{r \to a} (\mathrm{E}_1(r/a) - \mathrm{E}_n(r/a)) \equiv \frac{\theta_0 n}{a} \alpha_n. \tag{2.56}$$

This then is the dispersion relation we are after. It takes the usual form for a dispersion relation since E_1 represents advection by the basic state velocity field and E_n represents the perturbation propagation, both of which are infinite here. The combined limit, however, is finite, as is illustrated in Figure 2.4(b) for the case $n = 3$. To evaluate α_n analytically we use the following two recursion relations for the Bessel functions $\mathrm{J}_n(\kappa)$ (see

Gradshteyn & Ryzhic (2000)):

$$\begin{aligned} n\mathrm{J}_n + \kappa \mathrm{J}_n' &= \kappa \mathrm{J}_{n-1} &(2.57)\\ \mathrm{J}_n &= \frac{n-1}{\kappa}\mathrm{J}_{n-1} - \mathrm{J}_{n-1}'. &(2.58)\end{aligned}$$

Multiplying these relations together gives

$$n\mathrm{J}_n^2 + \frac{1}{2}\kappa\left(\mathrm{J}_n^2\right)' = (n-1)\mathrm{J}_{n-1}^2 - \frac{1}{2}\kappa\left(\mathrm{J}_{n-1}^2\right)', \tag{2.59}$$

from which it follows that:

$$n\alpha_n = (n-1)\alpha_{n-1} + \int_0^\infty \left(\frac{1}{2}\kappa\left(\mathrm{J}_{n-1}^2\right)' + \frac{1}{2}\kappa\left(\mathrm{J}_n^2\right)'\right)\,\mathrm{d}\kappa + \int_0^\infty \mathrm{J}_1^2\,\mathrm{d}\kappa \tag{2.60}$$

or, on integrating by parts,

$$n\alpha_n = (n-1)\alpha_{n-1} - \frac{1}{2}\int_0^\infty \left(\mathrm{J}_{n-1}^2 + \mathrm{J}_n^2\right)\,\mathrm{d}\kappa + \frac{1}{2}\left[\kappa(\mathrm{J}_{n-1}^2 + \mathrm{J}_n^2)\right]_0^\infty + \int_0^\infty \mathrm{J}_1^2\,\mathrm{d}\kappa \tag{2.61}$$

which can be written as

$$n\alpha_n = (n-1)\alpha_{n-1} + \frac{1}{2}(\alpha_n + \alpha_{n-1}) + \frac{1}{2}\left[\kappa(\mathrm{J}_{n-1}^2 + \mathrm{J}_n^2)\right]_0^\infty. \tag{2.62}$$

The final term here can be evaluated using the following asymptotic results (Gradshteyn & Ryzhic (2000))

$$\begin{aligned} \mathrm{J}_n(\kappa) &\sim \frac{1}{n}\left(\frac{\kappa}{2}\right)^n \quad \text{for} \quad \kappa \ll \sqrt{n+1} &(2.63)\\ \mathrm{J}_n(\kappa) &\sim \sqrt{\frac{2}{\pi\kappa}}\cos\left(\kappa - (2n+1)\frac{\pi}{4}\right) \quad \text{for} \quad \kappa \gg n^2 - 1/4, &(2.64)\end{aligned}$$

to give $\left[\kappa(J_n^2 + J_{n-1}^2)\right]_0^\infty = 2/\pi$. Therefore,

$$\alpha_n = \alpha_{n-1} + \frac{1}{\pi}\frac{1}{(n-1/2)}, \tag{2.65}$$

or

$$\alpha_n = \frac{1}{\pi}\sum_{j=2}^{n}\frac{1}{j-1/2} \tag{2.66}$$

since $\alpha_1 = 0$ trivially. Therefore the dispersion relation (2.56) can be written as

$$\boxed{\omega_n = \frac{\theta_0 n}{a}\frac{1}{\pi}\sum_{j=2}^{n}\left(\frac{1}{j-1/2}\right)} \tag{2.67}$$

for $n \geq 2$. This dispersion relation is the main result of this section. Below we examine its properties in detail and then verify it via numerical simulations.

First, we note for comparison the corresponding result for linear perturbations to the 2-d Euler Rankine vortex. Taking q_0 as the uniform patch vorticity the dispersion relation is (see Saffman (1995))

$$\omega_n = \frac{q_0}{2}(n-1). \tag{2.68}$$

For both of these cases, (2.67) and (2.68), the corresponding phase and group speeds can be calculated as

$$c_{p,n} = \frac{a\omega_n}{n} \quad \text{and} \quad c_{g,n+1/2} = a(\omega_{n+1} - \omega_n) \tag{2.69}$$

respectively. Note that the surface QG phase speeds are independent of the patch radius whereas the barotropic phase speeds are proportional to the patch radius, a result which is obvious from dimensional grounds. Figure 2.5 shows plots of the phase and group speeds as functions of wavenumber, n. We have non-dimensionalised the speeds by θ_0 in the surface QG case and aq_0 in the 2-d Euler case.

To analyse the form of the surface QG dispersion relation (2.67) we note that for large n (see Gradshteyn & Ryzhic (2000)):

$$\sum_{j=2}^{n} \left(\frac{1}{j-1/2} \right) = \log n + \gamma + 2(\log 2 - 1) + \mathrm{O}(n^{-2}), \tag{2.70}$$

where $\gamma = 0.57721...$ is Euler's constant. The dispersion relation (2.67) therefore satisfies

$$\omega_n = \frac{\theta_0}{\pi a} n(\log n + \mu) + \mathrm{O}(n^{-1}), \tag{2.71}$$

where $\mu = \gamma + 2(\log 2 - 1) \approx -0.03649$. Truncating the $\mathrm{O}(n^{-1})$ terms gives a remarkably accurate approximation with fractional errors of only 1.5% for $n = 2$ and 0.4% for $n = 3$. The solid lines in Figure 2.5(a) show this accuracy visually for the corresponding phase and group speeds, group speed now defined as $c_g = a\partial\omega_n/\partial n$, and Table (2.1) shows the values numerically. It is intriguing that this truncated version of the dispersion relation has the same form as that of waves on straight θ discontinuities given by (1.48).

Finally we note that the dispersion relation for the surface QG Rankine vortex (2.67) satisfies a peculiar group speed–phase speed relation,

$$c_{g,n+1/2} = \frac{1}{2}(c_{p,n} + c_{p,n+1}) + \frac{\theta_0}{\pi}, \tag{2.72}$$

which is also satisfied exactly for waves on a straight θ discontinuity (1.48) in that

$$\frac{\partial\omega}{\partial k} = \frac{\omega}{k} + \frac{\Delta\theta}{\pi}. \tag{2.73}$$

This result is independent of any ambiguities associated with the basic state velocity profile and appears to be a robust property of perturbations at θ discontinuities.

2.3.3 Numerical verification

Here we verify the dispersion relation of (2.67) via numerical simulation of temperature patches using the surface QG model described in Section 1.3.4 and Appendix A.

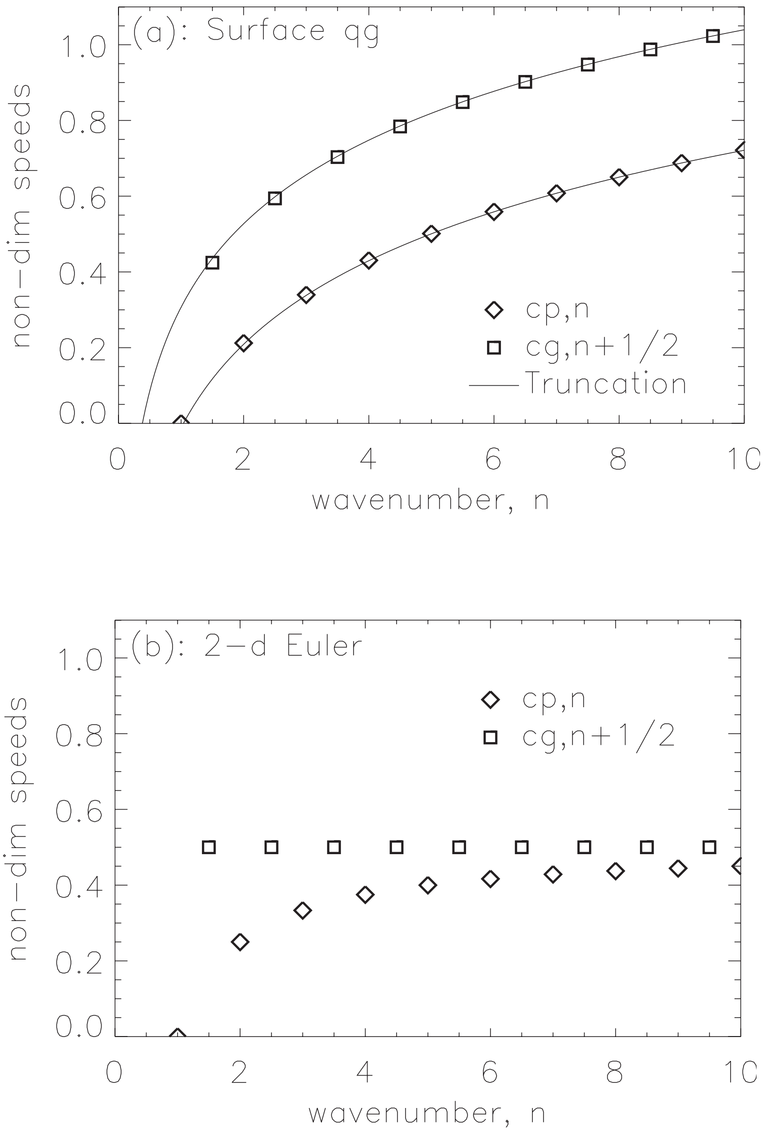

Figure 2.5 Panel (a): Non-dimensional phase and group speeds (c_p and c_g respectively) for the surface QG and, Panel (b): 2-d Euler, systems. Symbols mark the exact analytic results of (2.67) and (2.68). The lines in panel (a) show the corresponding quantities for the truncated version of the dispersion relation (2.71).

We specify the initial condition in the model as a circular patch of anomalous θ with a small amplitude, single wavenumber perturbation of its circumference and then sum, at each time step, the squared differences between the current and the initial states,

$$\sum_{\text{gridpoints}} (\theta(t) - \theta(0))^2 . \tag{2.74}$$

We find the location of the first minimum in this time series using a quadratic fitting technique and this corresponds to the time taken for the perturbation to rotate through an angle of $2\pi/n$, which we write as $\tilde{t}_n$ (we use the tilde to denote numerically obtained values). The corresponding non-dimensionalised phase speed is then given by $\tilde{c}_{p,n} = 2\pi a / n\tilde{t}_n\theta_0$.

Table 2.1 shows that the best estimate of the phase speeds achieved from the numerics is within a suitably defined error of the analytic result for a range of wavenumbers and this therefore verifies the result. However, our model in not ideally designed for this simulation[3] and several issues had to be carefully considered. We discuss these now.

Firstly, the sharp gradients in the basic state (2.32) cannot be accurately represented by any grid-based numerical scheme. We choose instead to simulate a smooth version

---

[3] A pure contour dynamics method (e.g. Zabusky et al. (1979), Pullin (1992)) appears to be the most natural choice, but this suffers from the logarithmic singularity in the along-front velocity field. Recent work by Rodrigo (2005) has made progress on this problem by removing the singular along-front component of the velocity field before advecting the contours. This is a promising line of research, but is not investigated here.

Wavenumber n	Analytic result $c_{p,n}$	Numerical result $\tilde{c}_{p,n}$	Fitting error σ_{fit}	Truncated formula $n(\log n + \mu)/\pi$
2	0.2122	0.2091	0.0012	0.2090
3	0.3395	0.3384	0.0020	0.3380
4	0.4305	0.4274	0.0025	0.4297
5	0.5012	0.4953	0.0022	0.5007
6	0.5591	0.5522	0.0032	0.5587
7	0.6081	0.5996	0.0040	0.6078
8	0.6505	0.6401	0.0046	0.6503

Table 2.1 Analytic and numerically obtained phase speed values, non-dimensionalised with θ_0. Also shown are the corresponding fitting error, see text, and numerical values from the truncated formula (2.71).

of the profile given by

$$\theta(r,\varphi) = \frac{1}{2}\left\{1 - \tanh\left[\frac{r - a(1+\epsilon\cos(n\varphi))}{\delta}\right]\right\}, \tag{2.75}$$

where δ and ϵ are measures of the edge steepness and perturbation amplitude respectively. This profile is well behaved numerically for a wide range of δ and by systematically varying δ and then extrapolating to $\delta = 0$ we can verify that the numerical results are consistent with the analytic result of Section 2.3.2. It is shown implicitly in Juckes (1995) that the leading order effect of a slight smoothing of width δ to a θ discontinuity is a reduction in the perturbation phase speeds of the form

$$c_p^{\text{smooth}} \sim c_p - B\delta^2 \log(\delta/\delta_0) \tag{2.76}$$

where B and δ_0 are constants depending on the form of the smoothing and the wavenumber of the perturbation. We use this form of the correction to extrapolate our numerical results to the limit of $\delta \to 0$. We plot in Figure 2.6(a) some numerically obtained phase speeds for the profile (2.75) for various values of δ and $n = 3$. Also plotted is the fit (2.76) where c_p, B and δ_0 are the fitting parameters. The variation of numerical phase speed with smoothing width is captured well by this fit.

We estimate an error in the extrapolated phase speed value based on resolution effects as follows. We first calculate the number of grid points covered by the smoothed patch-edge region along a cross section of the patch in each experiment. We then calculate the error estimate by comparing the variation of this number across the range of experiments performed with the variation of the corresponding phase speeds obtained and assume that the finite numerical resolution introduces an error in the effective smoothing width of $\pm 1/2$ grid size. We refer to this error estimate further below.

The other issue with the numerical scheme is the domain periodicity, that is, the effect of the surrounding vortices in the effective infinite array which is being simulated. We have repeated the above extrapolation process for a range of radius values to investigate the effect that periodicity has on the phase speeds since the strength of the interactions will decrease with patch radius, a.

Some results are shown in Figure 2.6(b), again for the case $n = 3$. Note that, since the fit (2.76) appears to be fairly robust we use fewer δ values here than in Figure 2.6(a) to save computation time. The effect of periodicity is not exactly azimuthally symmetric but tests have shown it to be very nearly symmetric for the radius values used here. As such, its only effect is to reduce the measured phase speeds. By extrapolating the results to the limit $a \to 0$ we can achieve our best estimate of the theoretical phase

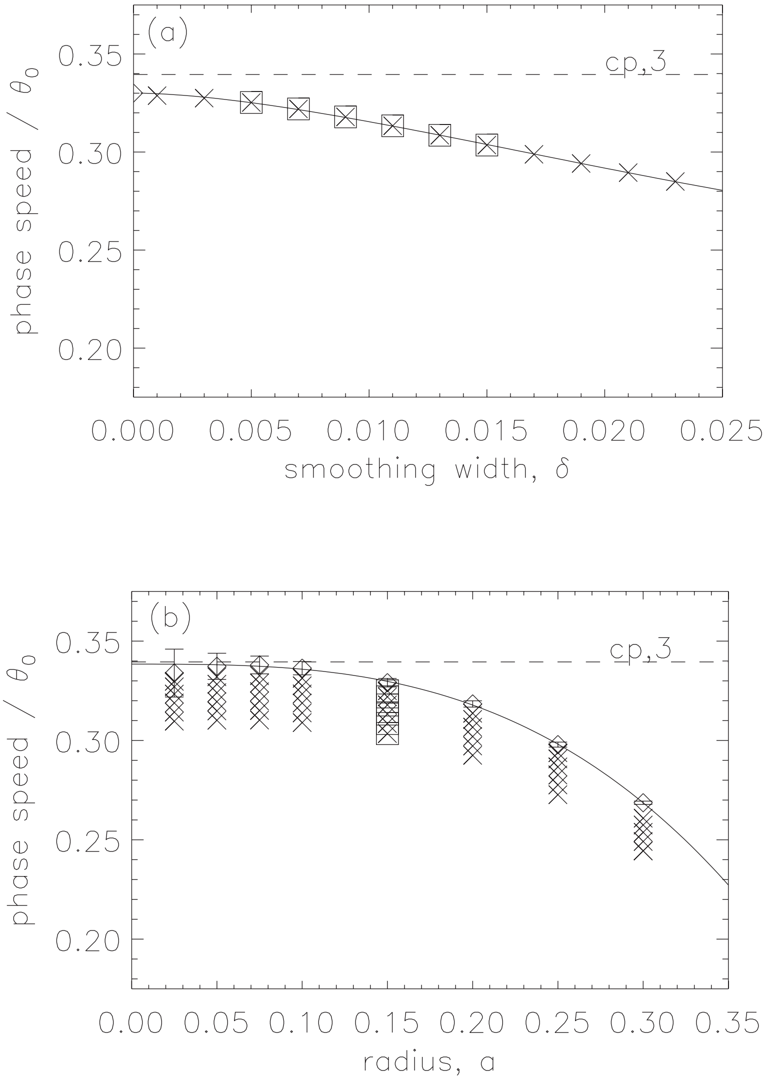

Figure 2.6 Panel (a): Numerically obtained phase speeds versus δ for the case $a = 0.15$, $\epsilon = 0.00667$ and $n = 3$; solid line is nonlinear fit of (2.76), dashed line is analytic result $c_{p,3}$ and squares show the values used for panel (b). Panel (b): Numerically obtained phase speeds versus a for the case $\epsilon = 0.00667$ and $n = 3$; diamonds are extrapolations to $\delta \rightarrow 0$ with associated error bar (see text), solid line is nonlinear fit for periodicity (see text) and dashed line is again $c_{p,3}$.

speed from the numerical simulations. The fit we have used to extrapolate to $a \to 0$ is based on a sum of the large r/a expansion of $U(r)$ given in (2.39) over many of the nearest neighbour patches. The data is weighted in the fit according to the resolution error described above at each radius value and the corresponding fitting error, σ_{fit}, of the best estimate phase speed is calculated and presented in Table 2.1. The analytic result of Section 2.3.2 lies within this error of the numerically obtained value.

In summary, by extrapolating to the double limit of δ, $a \to 0$ we have shown that, to within a calculated resolution error, the analytic result of Section 2.3.2 is correct for the case $n = 3$. We have repeated this process for a range of different wavenumbers and the results are also summarised in Table 2.1. In each case the numerical result lies within $2\sigma_{\text{fit}}$ of the analytic result. Noticeably, all numerically obtained phase speeds are slower than the analytic value and this suggests that other systematic errors are present which have not been taken into account. However, they appear to be not much larger than the resolution error. The most likely candidates are the accuracy of the back-trajectory calculation in the semi-Lagrangian scheme, the hyper-diffusion like effects associated with interpolation used in the semi-Lagrangian scheme and nonlinear amplitude effects on the wave propagation.

2.4 The surface shielded Rankine vortex [4]

Having derived the dispersion relation for disturbances to the surface Rankine vortex, the simplest possible surface QG vortex, we now proceed to extend the method to investigate the dynamics of more complicated vortices. In particular, we study the stability of the simplest potentially unstable surface QG vortex: the shielded surface Rankine vortex. That is, a temperature profile of the form

$$\theta(r) = \Theta(r) \equiv \begin{cases} \theta_0 & r < a \\ \theta_1 & a < r < b \\ 0 & r > b. \end{cases} \tag{2.77}$$

This profile represents a circular surface Rankine vortex of temperature θ_0 surrounded by an annulus of uniform temperature θ_1. Through linearity the corresponding basic state velocity field is simply a sum of two terms like (2.37)

$$U(r) = (\theta_0 - \theta_1)\mathrm{E}_1(r/a) + \theta_1 \mathrm{E}_1(r/b). \tag{2.78}$$

---

[4] The work of this section is published in Harvey et al. (2011)

The method we apply below could in principle be applied to a vortex consisting of any number of temperature jumps, but the basic result regarding instability is most easily seen in the two-step case.

2.4.1 The dispersion relation

To analyse the evolution of perturbations on this basic state we follow the 'direct method' from Section 2.3.2 except that here there are two boundaries which must be taken into account. Consider perturbing each boundary independently to the new positions

$$r = r_1(\varphi, t) \equiv a + \eta(\varphi, t) \quad \text{and} \quad r = r_2(\varphi, t) \equiv b + \nu(\varphi, t), \tag{2.79}$$

and linearising the equation for material advection of each boundary, for small η and ν. The result is a pair of equations analogous to (2.50),

$$\frac{\partial \eta}{\partial t} = \lim_{r \to a} \left(u_r' - \frac{U(r)}{a} \frac{\partial \eta}{\partial \varphi} \right) \tag{2.80}$$

$$\frac{\partial \nu}{\partial t} = \lim_{r \to b} \left(u_r' - \frac{U(r)}{b} \frac{\partial \nu}{\partial \varphi} \right), \tag{2.81}$$

where $U(r)$ is given by (2.78) and the perturbation radial velocity $u_r'(r, \varphi, t)$ is likewise a linear sum of contributions from each boundary of the form (2.55). Like before we restrict attention here to a single Fourier mode, $(\eta, \nu) = (a\hat{\eta}(t), b\hat{\nu}(t))e^{\mathrm{i}n\varphi}$:

$$u_r' = \frac{in}{r}\left(a\hat{\eta}(\theta_0 - \theta_1)\mathrm{E}_n(r/a) + b\hat{\nu}\theta_1\mathrm{E}_n(r/b)\right)e^{in\varphi}. \tag{2.82}$$

We now substitute for U and u_r' in (2.80) and (2.81) and write the system in matrix form for convenience. First we define the non-dimensional parameters

$$\lambda = b/a \quad \text{and} \quad \mu = \theta_1/\theta_0 \tag{2.83}$$

to simplify notation, and note from (2.36) that $\mathrm{E}_n(1/\lambda) = \lambda \mathrm{E}_n(\lambda)$. The system (2.80)-(2.81) can then be written

$$i\frac{\mathrm{d}}{\mathrm{d}t}\begin{pmatrix} \hat{\eta} \\ \hat{\nu} \end{pmatrix} = \frac{\theta_0 n}{a}\begin{pmatrix} (1-\mu)\alpha_n + \lambda\mu\mathrm{E}_1(\lambda) & -\lambda^2\mu\mathrm{E}_n(\lambda) \\ -\dfrac{(1-\mu)\mathrm{E}_n(\lambda)}{\lambda^2} & \dfrac{\mu\alpha_n}{\lambda} + \dfrac{(1-\mu)\mathrm{E}_1(\lambda)}{\lambda} \end{pmatrix}\begin{pmatrix} \hat{\eta} \\ \hat{\nu} \end{pmatrix} \tag{2.84}$$

$$\equiv \boldsymbol{F}\begin{pmatrix} \hat{\eta} \\ \hat{\nu} \end{pmatrix}, \tag{2.85}$$

where α_n is defined in (2.66). The matrix $\boldsymbol{F}$ contains all the information for the evolution of linear perturbations. The diagonal elements represent the propagation of the disturbances on each boundary whereas the off-diagonal elements represent the interaction between the boundaries. Here we have chosen θ_0/a as the dimensional scale for consistency with the study of Flierl (1988). That is, we imagine a central vortex of amplitude θ_0 and radius a and ask how the different 'shields' modify the vortex behaviour. An alternative, which we discuss further below, is to focus on the filament-like nature of the instability. That is, consider the outer annulus as a circular filament of width $b-a$, the instability of which is modified by the circular geometry and the presence of the central vortex.

The normal mode frequencies of the system are given by the eigenvalues of $\boldsymbol{F}$ which take the form

$$\Omega_n^{\pm} = \frac{\mathrm{tr}(\boldsymbol{F})}{2} \pm \sqrt{\left(\frac{\mathrm{tr}(\boldsymbol{F})}{2}\right)^2 - \det(\boldsymbol{F})}. \tag{2.86}$$

There are therefore unstable normal modes when $\mathrm{tr}(\boldsymbol{F})^2 < 4\det(\boldsymbol{F})$. This boundary of stability in (λ, μ)-space is shown in Figure 2.7(a) for several wavenumbers. To interpret the figure we note that the surface QG analogue of the Rayleigh theorem, see equation (2.21), requires a radial temperature profile to contain regions of opposing gradient for growing normal modes to exist. These are only present in (2.77) if $\mu > 1$ or $\mu < 0$ and the regions of normal mode growth in Figure 2.7(a) are indeed contained within these regions.

Figure 2.7(b) shows the corresponding 2-d Euler calculation for comparison, following Figure 2 of Flierl (1988). That is, the stability boundaries for a shielded Rankine vortex consisting of an inner circular patch with vorticity q_0 and an outer annulus with vorticity q_1. The two plots have many qualitative similarities, the main difference being that the $n = 2$ mode is stable for all $q = q_1/q_0 > 0$ in the 2-d Euler case whereas for the surface QG system there is a region of parameter space with $\mu > 0$ where the $n = 2$ mode is unstable. Another difference is that for the surface QG case the boundaries of stability do not all continue to large λ. For the 2-d Euler case the boundaries of stability all tend towards $q = (n-1)/(n-2)$ at large λ (see Flierl (1988)) whereas for the surface QG system modes $n = 2-4$ satisfy

$$\mu \sim 1 + \left(\frac{1}{2\alpha_n} - 1\right)\frac{1}{\lambda} \quad \text{for} \quad \lambda \gg 1, \tag{2.87}$$

but modes with $n \geq 5$ (for which $\alpha_n > 1/2$) are stable for all μ at λ larger than a critical value given by the solution to $\lambda_{\mathrm{c}}^2 \mathrm{E}_1(\lambda_{\mathrm{c}}) = \alpha_n$. This expression is found by noting that the stability boundary is given by the implicit equation $\mathrm{tr}(\boldsymbol{F})^2 = 4\det(\boldsymbol{F})$. Expanding this equation for $\lambda \gg 0$ we find the expression (2.87), where we have also used the asymptotic result derived in Appendix B that $\mathrm{E}_n \sim C_n/\lambda^{n+1}$ with $C_1 = 1/2$.

(a) SQG

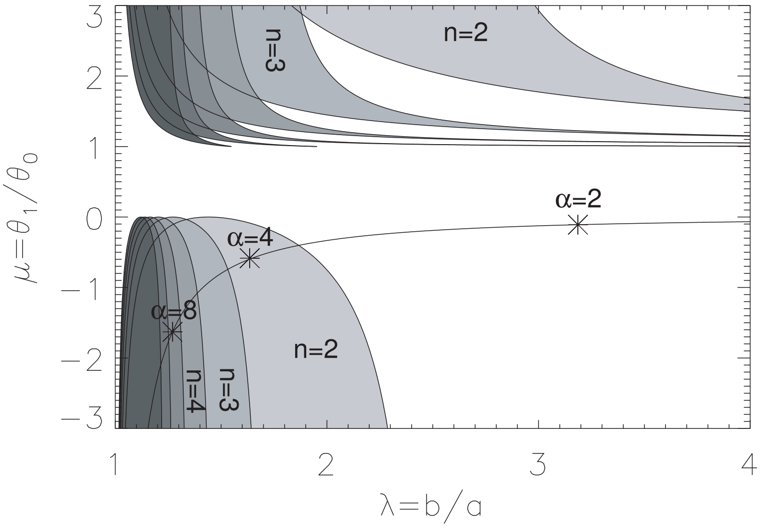

(b) 2D Euler

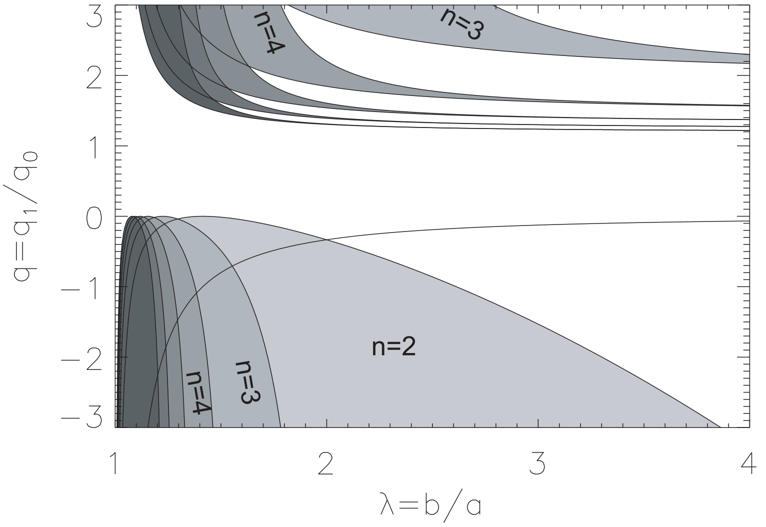

Figure 2.7 Panel (a): Stability boundary in (λ, μ)-space for wavenumbers $n = 2 - 7$. The solid line indicates vortices with zero integrated temperature, see (2.91), and the asterisks indicate the positions of the profiles (2.97)-(2.98) for several α values. Panel (b): Stability boundary for the 2-d Euler problem. The solid line indicates vortices with zero integrated vorticity.

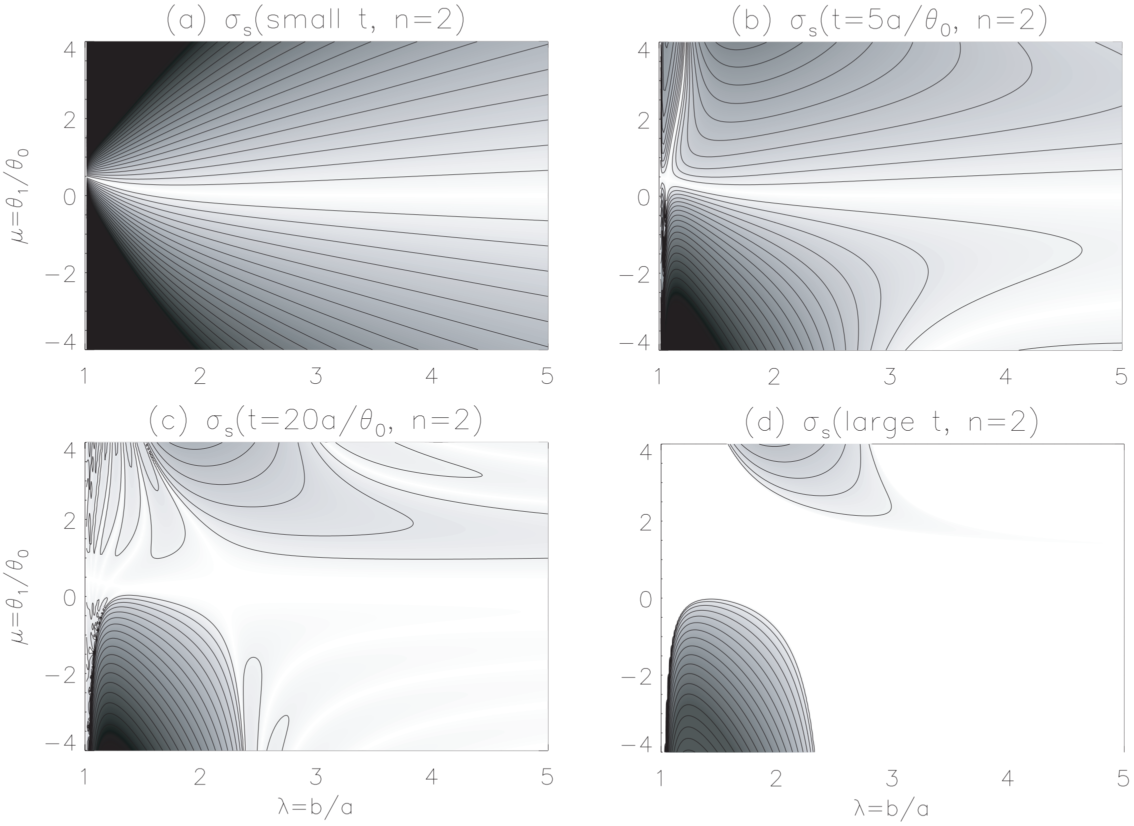

Figure 2.8 Contoured values of σ_s for wavenumber $n = 2$ and t values as indicated. The small and large t plots are given by the formulae (2.89) and (2.90) respectively. The contour interval is $0.05\theta_0/a$ with dark shading indicating high values and black shading indicating values greater than θ_0/a.

2.4.2 Non modal disturbances

The normal modes of (2.86) are special perturbation configurations which preserve their shape in time. In general, unstable solutions to equations of the form (2.85) undergo an initial period of transient development during which they align towards the growing normal mode shape (see Farrell & Ioannou (1996) and Carton et al. (2010) for a full description of such non-modal behaviour). The main result is that the transient development can exhibit a temporary period of growth at rates larger (or smaller) than the normal mode growth rate, depending on the initial configuration of the perturbation (i.e. $\hat{\eta}(0)$ and $\hat{v}(0)$). Similarly, stable solutions can exhibit periodic cycles of transient growth and decay which, whilst not causing a long-term net growth to perturbations, may temporarily increase the perturbation size. In this subsection we calculate some simple results to illustrate this.

A standard method of analysis is to consider the so-called singular mode amplitude, which is the value of a given norm at any given time maximised over all initial conditions. The singular mode amplitude can be calculated analytically in terms of the elements of $\boldsymbol{F}$ following the methods of Farrell & Ioannou (1996). This has been done for the root mean square wave slope norm and Figure 2.8 shows values of the corresponding singular mode equivalent growth rate,

$$\sigma_{\mathrm{s}}(t) = \frac{\log(N_{\mathrm{s}}(t)/N(0))}{t}, \tag{2.88}$$

where $N_{\mathrm{s}}(t)/N(0)$ is the singular mode amplitude scaled by the initial perturbation amplitude. It can be shown that (Farrell & Ioannou, 1996) N_{s} has the following asymptotic limit for small times ($t \ll |\Omega_n^{\pm}|^{-1}$)

$$N_{\mathrm{s}}(t) \sim N(0)(1 + \frac{|F_{12} - F_{21}|}{2} t), \tag{2.89}$$

where F_{12} and F_{21} are the off-diagonal elements of $\boldsymbol{F}$, and for large times ($t \gg |\Omega_n^{\pm}|^{-1}$)

$$N_{\mathrm{s}}(t) \sim N(0)\frac{|F_{12} - F_{21}|}{2\mathrm{Im}(\Omega_n^{+})} e^{\mathrm{Im}(\Omega_n^{+})t}, \tag{2.90}$$

if $\mathrm{Im}(\Omega_n^{+}) > 0$ and $N_{\mathrm{s}}(t) \sim 0$ otherwise. The figure shows these two limits graphically as well two intermediate times. It is consistent with the notion that non-modal disturbances of wavenumbers within the range of growing normal modes undergo a transient period of growth potentially larger than the corresponding normal mode growth rate during which they adjust towards the normal mode shape, followed by what is effectively normal mode growth. Non-modal disturbances outside the range of the growing normal modes continually undulate around their initial configuration resulting in a σ_{s} which decays in time. The ridges, particularly apparent in panel (c), are a result of this undulatory non-modal behaviour.

2.4.3 Completely shielded vortices

Returning now to analyse the normal modes in more detail, we focus on completely shielded vortices, that is, vortices with zero net integrated temperature anomaly. This constraint is given by

$$(\lambda^2 - 1)\mu = -1 \tag{2.91}$$

for shielded Rankine vortices, as is illustrated in Figure 2.7(a) by the solid line. This class of vortex is important because it represents vortices with a more localised influence than not-completely-shielded cases. In particular, the class of vortices studied by Carton (2009) are completely shielded. However, recall from Section 2.2 that, unlike in the 2-d

Euler case, this constraint is not required on energy grounds for surface QG vortices. Their energy is finite even if they are not shielded.

Figure 2.9(a) shows the normal mode growth rates of perturbations for completely shielded surface Rankine vortices as a function of λ. Panel (b) shows the corresponding 2-d Euler result for comparison. The surface QG vortices display the familiar behaviour also observed in the two-dimensional Euler case, through theory and experiment, that the wavenumber of the fastest growing normal mode is dependent on the vortex profile, with progressively higher modes being relevant for smaller λ, or larger μ. The increase in growth rate as $\lambda \to 1$ is consistent with a consideration of filament instability, as we show below. First we compare the growth rates to those of the Carton (2009) study.

The family of vortices studied by Carton (2009) have temperature profiles of the form

$$\theta = \Theta(r) \equiv \Theta_0(\alpha)\left(1 - \frac{\alpha}{2}\left(\frac{r}{R}\right)^{\alpha}\right) e^{-(r/R)^{\alpha}} \tag{2.92}$$

where r is the radial coordinate, R and α are positive constants and $\Theta_0(\alpha)$ is a normalisation factor such that the corresponding azimuthal velocity field $\bar{u}(r)$ satisfies $\max(\bar{u}) = u_0$. These profiles consist of a central temperature maximum surrounded by an annulus of negative temperature anomaly, as illustrated in Figure 2.10. We approximate them as shielded surface Rankine vortices by choosing suitable values for θ_0, θ_1 and the sizes of the inner and outer regions.

There is freedom in choosing these parameters; we choose them to satisfy the following four constraints:

$$r = a \qquad \text{minimises} \quad \mathrm{d}\Theta/\mathrm{d}r \tag{2.93}$$

$$r = b \qquad \text{maximises} \quad \mathrm{d}\Theta/\mathrm{d}r \tag{2.94}$$

$$\int_0^{\infty} \bar{\theta}(r) r \,\mathrm{d}r = 0 \tag{2.95}$$

$$\int_0^{a} \bar{\theta}(r) r \,\mathrm{d}r = \int_0^{a} \Theta(r) r \,\mathrm{d}r. \tag{2.96}$$

That is, the locations of the jumps coincide with the points of steepest temperature gradient and the two temperature values θ_0 and θ_1 are chosen so that both the total integrated temperature anomaly is zero and the integrated temperature anomaly in the range $r < a$ equals that of the smooth profiles. The choice is of course not unique, but it suffices to provide a qualitative comparison between the systems. Figure 2.10 illustrates this choice of parameters for several values of α. The differences between the two growth rates is expected to be sensitive in particular for small α where the smooth profiles differ most from the Rankine profiles.

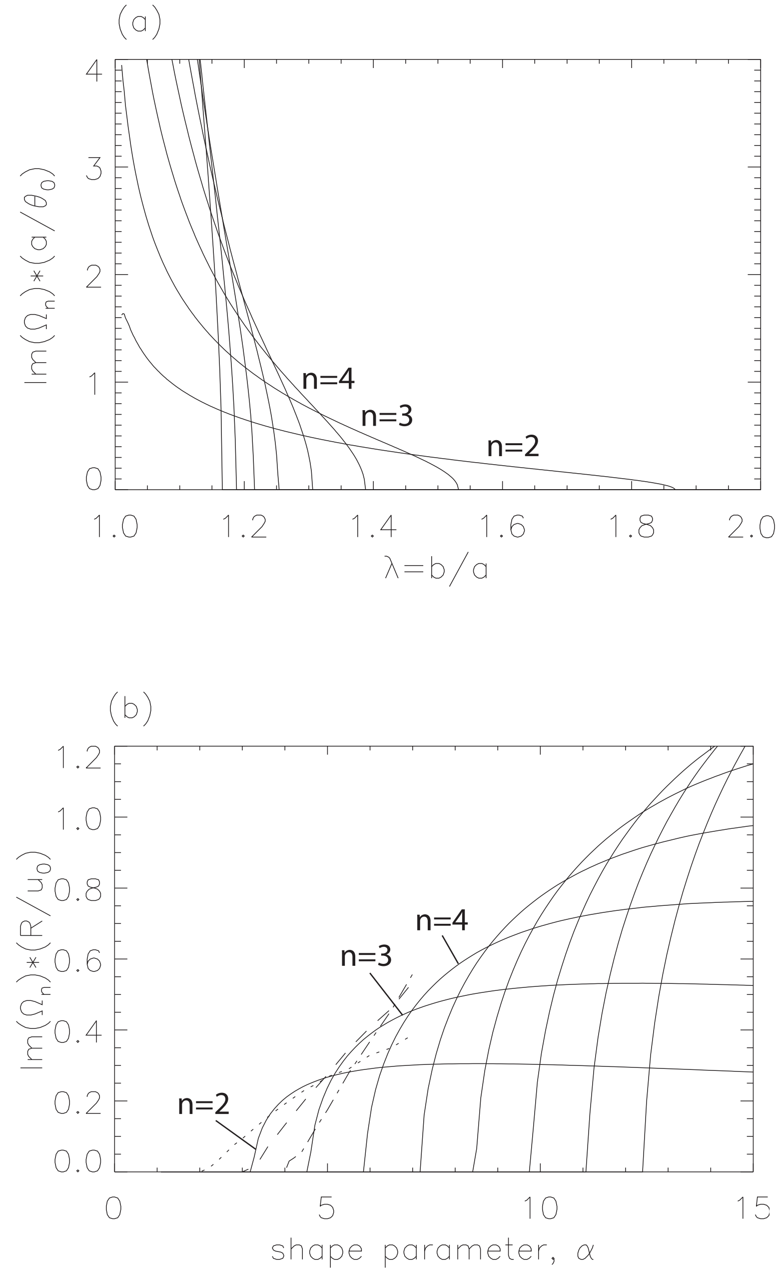

Figure 2.9 Panel (a): Normal mode growth rates for completely shielded vortices as a function of λ. Panel (b) Normal mode growth rates for the parameter values (2.97)–(2.98) as a function of α. In both panels, wavenumbers 2–4 are indicated, the higher modes follow the pattern. In panel (b) the broken lines show data from Carton (2009) (see text) where dotted is $n = 2$, dashed is $n = 3$ and dot-dash is $n = 4$.

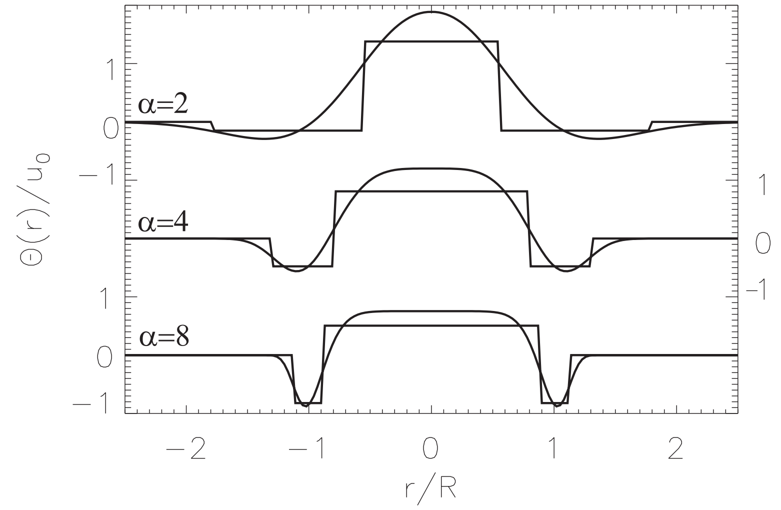

Figure 2.10 Some example temperature profiles. Smooth curves are the Carton (2009) profiles of (2.92), for the α values shown, and the discontinuous profiles are the corresponding shielded Rankine vortices given by (2.97)-(2.98).

The vortex parameters satisfying the constraints (2.93)-(2.96) are given by

$$\begin{pmatrix} a \\ b \end{pmatrix} = R\left[\frac{3\alpha+1}{2\alpha} \mp \sqrt{\left(\frac{3\alpha+1}{2\alpha}\right)^2 - \frac{(\alpha+2)(\alpha-1)}{\alpha^2}}\right]^{1/\alpha}, \tag{2.97}$$

$$\theta_0 = \Theta_0(\alpha)e^{-(a/R)^\alpha}, \quad \theta_1 = \frac{-\theta_0 a^2}{b^2 - a^2} \tag{2.98}$$

where Θ_0 and α are as in (2.92). Figure 2.9(b) shows the corresponding normal mode growth rates, $\mathrm{Im}(\Omega_n)$, as a function of α. Note that the data plotted here is identical to that of Figure 2.9(a) except for the choice of scalings.

Also shown in Figure 2.9(b) are the numerically obtained growth rates from Carton (2009) for the corresponding smooth cases. There is a clear similarity between the two cases. The main difference is a shift towards higher α values in our figure since the first unstable mode appears near $\alpha = 3$ whereas there are unstable modes from $\alpha = 2$ in Carton (2009). The magnitude of the growth rates, however, are comparable between the two cases.

As mentioned above, the increase in growth rates for λ close to one, or equivalently large α, is consistent with the nature of filament instability in surface QG dynamics. This instability is studied in detail in Chapter 3. For comparison, a straight temperature filament of width L with a 'top-hat' profile, analogous to the Rayleigh problem of two-dimensional Euler dynamics, is unstable with normal mode growth rates given by

$$\sigma_{\text{fil}} = \frac{\theta}{L}\mathrm{F}(\kappa) \tag{2.99}$$

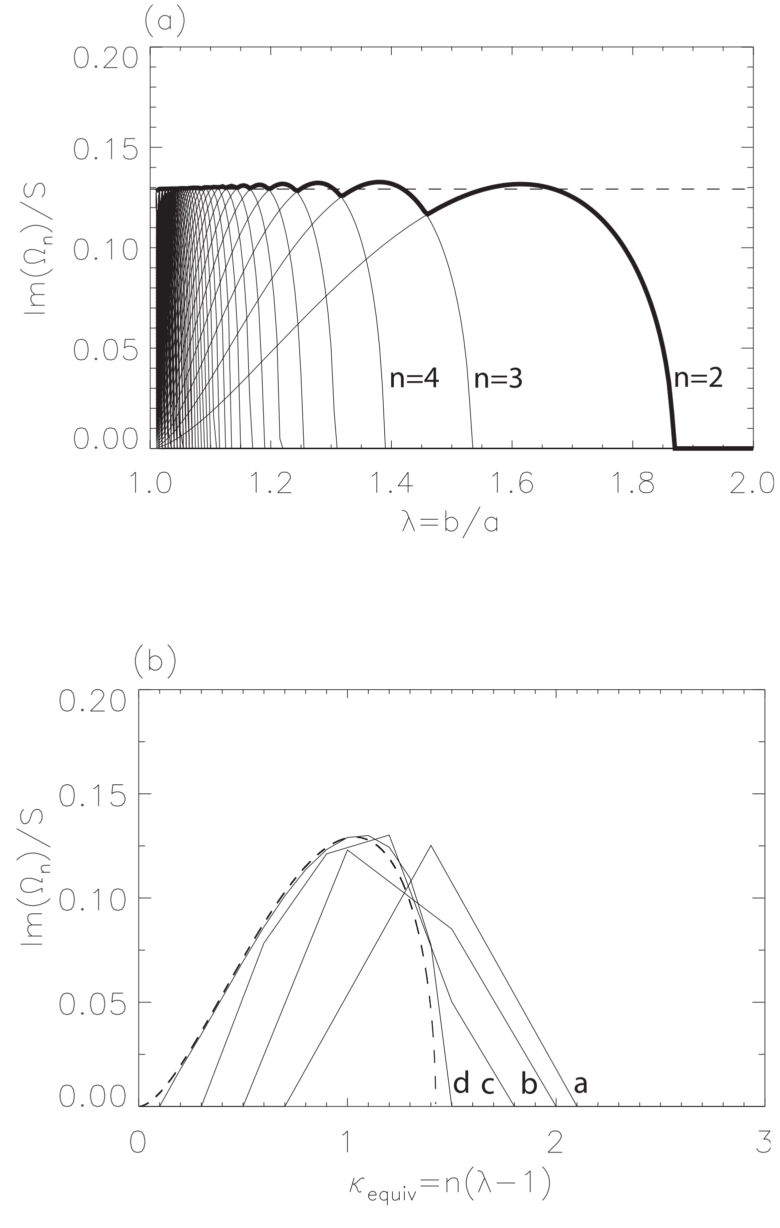

Figure 2.11 Panel (a): Normal mode growth rates scaled by S for vortices with zero integrated temperature anomaly. Wavenumbers 2–4 are indicated, the higher modes follow the pattern. The most unstable mode at each λ is emphasised by the heavy line and the dashed line represents $\max(\mathrm{F})S = 0.1292...S$ (see text). Panel (b): Scaled normal mode growth rates versus equivalent wavenumber κ_{equiv} for $\lambda = 1.7$, 1.5, 1.3 and 1.1, labelled a–d respectively. The dashed line shows the dispersion relation for a straight temperature filament.

where F is a function of the non-dimensional wavenumber $\kappa = kL$ (Juckes (1995); Harvey & Ambaum (2010)). As such, we define a scaling factor

$$S \equiv \frac{\sqrt{|\theta_1(\theta_0 - \theta_1)|}}{b-a} = \frac{\theta_0}{a}\frac{\lambda}{(\lambda+1)(\lambda-1)^2} \tag{2.100}$$

which is the ratio of a temperature scale (the geometric mean of the two temperature jumps) and the annulus width. Figure 2.11(a) shows that for unstable surface QG vortices satisfying (2.91), the maximum growth rate is always remarkably close to $\max(\mathrm{F})S \approx 0.1292S$. We expect a similar result to hold for the two dimensional Euler system, except in that case there is no length scale so the instability growth rates will just be proportional to the geometric mean of the two vorticity jumps.

To highlight the link to the filament instability further, Figure 2.11(b) shows the dispersion relation calculated for several vortices towards the limit of a large, but weak, central vortex with an outer annulus of fixed width L, i.e. $\lambda \to 1$ with $b - a = L$. The wavenumber n is scaled to coincide with the wavenumber κ of the filament in this limit,

$$\kappa_{\text{equiv}} = \frac{n}{a}(b-a) = n(\lambda-1), \tag{2.101}$$

and the growth rates are again scaled by S of equation (2.100). The growth rates do indeed appear to coincide with those of the straight filament in the limit of $\lambda \to 1$. The correction for larger λ shifts the growth rate curve to slightly larger κ_{equiv} values on average but, consistent with the discussion above, does not alter the maximum growth rate by very much. This shift in the maximum growth rate seems to be purely a geometric effect of the curvature.

2.5 Discussion

The main results from this chapter are (i) the derivation and testing of the dispersion relation for perturbations to the surface Rankine vortex, and (ii) the application of this dispersion relation to the study of unstable surface QG vortices. We now make a few comments regarding the implications of each result to our understanding of surface QG dynamics more generally.

The dispersion relation for the surface Rankine vortex shows qualitative similarities to its 2-d Euler counterpart and it is expected that further results from barotropic vortices carry over to the surface QG case. For instance, under 2-d Euler dynamics there are nonlinear perturbations to uniform vorticity patches which rotate steadily, the so-called V-states (Deem & Zabusky (1978), Verkley (1994), Ambaum & Verkley (1995)), and we expect there to be surface QG analogues. In fact, each mode of the linear dynamics in the barotropic case is associated with such a solution and we expect that the linear modes found here are likewise related to surface QG V-state solutions.

A further inference from the result concerns the behaviour of surface QG vortices embedded within a background flow. Such a flow will in general deform the vortex in a time dependent manner. For the simple case of a pure straining, $(u, v) = s(x, -y)$, there are illuminating steady state solutions in the small strain rate limit, $s \ll \theta_0/a$ (assuming s and θ_0 are both positive). In that case the deformation is small and so satisfies the dispersion relation (2.67). The $n = 2$ mode can propagate against the straining flow resulting in a steady state provided its phase speed matches the induced rotation speed of the straining which can be shown to be given by $c_{\mathrm{rot}} = -a^2 s/2\eta_0$, where η_0 is the perturbation amplitude. Equating this to $c_{\mathrm{p},2}$ from (2.69) we find the steady state requires

$$\frac{\eta_0}{a} = \frac{3\pi}{4}\frac{as}{\theta_0}. \tag{2.102}$$

Interestingly, this perturbation aspect ratio is proportional to the patch radius so a small vortex will not deform as strongly as a large vortex in the same straining field. Alternatively, this result suggests that small vortices require stronger strain values to cause vortex break-up than a larger vortex and this is consistent with the local nature of the surface QG Green's function. In contrast, the corresponding 2-d Euler result predicts a perturbation aspect ratio of $\eta_0/a = 2s/\Omega$ which is independent of vortex size. Whether (2.102) can be generalised to finite amplitudes as in the case of the Kida vortex is still an open question.

The consequences of this observation on the morphology of surface QG turbulence are interesting and something to which we later return (see Section 3.5). For the case of well-developed forced turbulence it might appear at first sight that (2.102) violates the possibility of achieving a statistically steady state which is scale-independent, in the sense of a snapshot looking the same at any magnification. However, we will suggest a mechanism by which typical values of θ_0 in such a turbulence situation must also scale with the length scale, meaning (2.102) is in fact consistent with the scale-independence of the shapes of vortices.

Chapter 3:

SURFACE QG FILAMENTS

3.1 Introduction[1]

In this chapter we investigate the third question posed in the Introduction: what controls the small scale curdling in surface QG simulations? The answer is already partly understood: it is related to the instability of filaments. In particular, the fact that a temperature filament in an otherwise quiescent fluid is unstable with disturbance growth rates that are *inversely proportional to the width of the filament*: narrower filaments become unstable faster than wider ones, resulting in the small scale curdling observed (Juckes (1995), Held et al. (1995)).

However, this is not the whole story. To see this we refer again to the 2-d Euler system. The corresponding problem, vorticity filament instability, is a very well-studied problem dating right back to Rayleigh (1880) in which the most basic set-up was first considered, the so-called Rayleigh problem. In that study the stability of a 'top-hat' filament of uniform vorticity in a quiescent background flow was derived: such a configuration is unstable, with disturbance growth rates that are *independent of the filament width*. It wasn't until high resolution numerical models were run during the 1980s (see, e.g. Juckes & McIntyre (1987)) that it was realised that the assumption of a quiescent background flow is not very robust. In fact, the very straining and shearing flows which often generate filament-like structures in the first place are often capable of inhibiting the growth of disturbances, as we observed in Figure 1.6 of the Introduction. In this chapter we investigate the effects that such external flow fields have on the instability of surface QG filaments, paying particular attention to the curdling which is observed at small scales.

---

[1] The work of this chapter is published in Harvey & Ambaum (2010)

The general mechanism whereby fluid dynamical flows can be stabilised by external straining and shearing has received a great detail of attention in the literature. The first, and again most basic, study was that of Dritschel (1989) and Dritschel et al. (1991). There the Rayleigh problem was extended to include the effects of first a background shearing flow and then a straining flow. As anticipated, it was shown that such modifications can indeed inhibit the instability. In particular, it was shown that a strain rate s as small as $0.25q_0$, where q_0 is the vorticity value of the filament, suppresses the conventional Rayleigh shear instability mechanism. This result lead to the now standard view that vorticity filaments which are formed in regions of strong straining remain coherent until they move away from the region, or else the straining there decreases, at which point they may succumb to the instability and 'roll-up' into vortices. These vortices themselves are then stable provided the ambient strain does not increase again to values comparable to q_0.

In this chapter we perform the analogous surface QG study to that of Dritschel. That is, we consider the stability of temperature filaments in the presence of both shear and strain in turn. To allow a simple comparison to the study of Dritschel we similarly consider a 'top-hat' filament of uniform temperature, the stability of which, in quiescent surroundings, has been studied by Juckes (1995). We find that the surface QG system exhibits striking differences to the 2-d Euler case, and these go a long way towards explaining and understanding the small scale curdling seen in the simulations. Put simply, the main results of the chapter are:

1. Adverse shearing can act to stabilise smooth surface QG filaments, in a similar fashion to the 2-d Euler case. However, the discontinuous top-hat profile can never be stabilised completely.
2. Straining, whilst capable of stabilising individual perturbations indefinitely, cannot in general stabilise filaments: there are always some perturbations which can grow large.

The first point is related to the inapplicability of the Fjortoft condition to discontinuous temperature profiles, as discussed previously in Section 2.1.2. The second point is the most important. We show that whilst perturbation growth on wide filaments can be inhibited by straining, narrow filaments are always unstable. As all filaments in strain eventually end up narrow the instability cannot be prevented indefinitely. This leads to an interesting result: in contrast to the standard view of 2-d Euler dynamics outlined above, surface QG filaments do not need to move away from the straining regions before instability occurs. They can be formed by straining, remain coherent whilst still wide and then, at a later time, become unstable.

Further motivation for this work comes from the debate in the literature as to whether the surface QG system can form temperature discontinuities in finite time. The 2-d Euler is well-known to be well posed for all time in the sense that an initially smooth vorticity distribution will remain smooth for all time. Majda & Tabak (1996) proposed a temperature distribution which according to their numerical surface QG simulations showed temperature gradients increasing like $|\nabla\theta| \sim (t-t_0)^{-5/3}$, thereby achieving finite-time discontinuity formation when $t = t_0$. However, Constantin et al. (1998) later disproved this claim. At present it is still unknown whether temperature discontinuities can form in finite time under surface QG dynamics. Given the above comments, the problem of filament instability is clearly a strong candidate for such behaviour. After the roll-up of a filament has occurred, there remains vortices that are inter-connected by much thinner filaments. Supposing these sub-filaments behave in a similar fashion to the original filament, it may be expected that a whole series of filaments develop at ever smaller scales. The time taken for each filament to roll-up, however, would be proportional its width. The total time taken to reach infinitely small scales would then be a geometric series with a finite sum. There are several potential problems with this hypothesis, the most obvious being that the presence of straining and shearing induced by the vortices is sufficient to retard the instability process, and this is something that we discuss at the end of this chapter.

To complete this introduction we provide a short survey of the literature around the mechanism of stabilisation by external flows. This provides a fuller picture of the context of this work. The main part of the chapter is then structured as follows. Section 3.2 reviews the work of Juckes (1995), with the aim of introducing notation and setting up the problem for the remaining sections. The analysis of the shear case is presented in Section 3.3 and the strain case takes up Section 3.4. We present our discussion and concluding remarks in Section 3.5.

3.1.1 History of ideas: stabilisation by strain and shear

An early paper commenting on the behaviour of vorticity filaments in the presence of large scale deforming flows was the work of Juckes & McIntyre (1987). They numerically integrate the 2-d Euler equations on a hemisphere with initial condition given by a circular vorticity distribution similar to that of the middle to upper stratosphere in winter. On the addition of a wave-1 topographic-like forcing, the 'polar vortex' deforms and sheds filamentary structures. Some of these behave as passive tracers, being stretched out into long thin filaments, whilst others are unstable and roll-up into vortices. Some of the vortices subsequently enter regions of stronger straining again because they are torn apart again into filaments. The authors promise some relevant theory in a forthcoming paper, presumably pointing to the papers of Dritschel (1989) and Dritschel et al. (1991) mentioned above.

An application of the idea in a more meteorological setting is investigated by Joly & Thorpe (1990) and Bishop & Thorpe (1994). They consider the following two-step mechanism for secondary cyclogenesis. First, a large scale strain field causes frontogenesis, and the associated formation of cloud. The diabatic lifting due to the large scale latent heat release induces a positive PV anomaly along the front in the lower troposphere. Typically, the strain forcing the frontogenesis is sufficient to suppress perturbation growth on the PV anomaly, so the second stage occurs only if the straining, and frontogenesis, weaken. Then the PV anomaly can become unstable and roll up into vortices which are observed at the surface through the induced wind field and associated wave-like displacement of the surface front. This process has recently been simulated in an idealised version of the Met Office Unified Model by Dacre & Gray (2006) producing results consistent with the previous studies which were of a more analytic nature.

Finally, Kevlahan & Farge (1997) perform an interesting numerical study which explicitly demonstrates the stabilising nature of large scale flows on 2-d Euler vorticity filaments. They run a simulation of a vortex-vortex merger situation from which complex system of filamentary structures is created. They then remove, using a novel wavelet transform technique, the part of the vorticity field which they define as making up the 'coherent vortices' and continue the simulation, in addition to also continuing the original full simulation. The subsequent evolutions are strikingly different: the filaments in the simulation with the coherent vortices removed quickly become unstable, whereas those of the original full simulation remain mostly coherent.

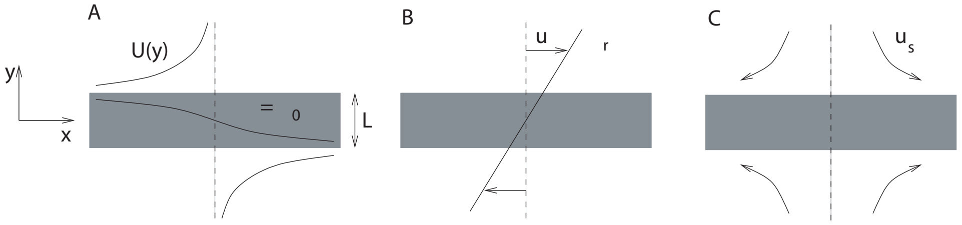

Figure 3.1 Sketches of (a) the basic state temperature and velocity fields, (b) the shear flow (3.16) and (c) the strain flow 3.22.

3.2 The isolated temperature filament

The problem considered by Juckes (1995) is that of a filament of anomalous surface temperature with a 'top-hat' profile as illustrated in Figure 3.1(a)[2],

$$\theta = \Theta(y) \equiv \begin{cases} \theta_0 & \text{for} \quad |y| < L/2 \\ 0 & \text{for} \quad |y| > L/2. \end{cases} \tag{3.1}$$

The velocity field induced by this temperature anomaly is also sketched in the figure. By (1.23), it is proportional to the Hilbert transform of the temperature field,

$$u = U(y) = \frac{\theta_0}{\pi} \log \left| \frac{y - L/2}{y + L/2} \right|, \quad v = 0. \tag{3.2}$$

The logarithmic singularities in the velocity field along the edges of the filament are again consistent with the observation of Section 1.3.3 that θ discontinuities induce velocity fields with logarithmic singularities under surface QG inversion. Recall, however, that despite this singularity the wave propagation characteristics of a slightly smoothed discontinuity are regular in the limit of sharp edges, at least for wavenumbers $k \ll \delta L^{-1}$ where δL is the width of the smoothing.

In the sharp edge limit, the dynamics of perturbations to the filament are governed entirely by the positions of the filament edges and the mathematical formulation follows very closely the method of Section 2.4. Similarly to that derivation there are two ways to proceed, either using the full nonlinear contour dynamics formulation or linearising the dynamics before applying the advection equations. We opt for the latter here for brevity. Suppose the filament edges are perturbed to the new positions

$$y = y_1(x,t) \equiv \frac{L}{2} + \eta_1(x,t) \quad \text{and} \quad y = y_2(x,t) \equiv -\frac{L}{2} + \eta_2(x,t). \tag{3.3}$$

Conservation of θ requires the filament edges to be material lines and so their evolution

---

[2] This is a special case of the shielded Rankine vortex of calculation of Section 2.4

is given by (analogous to (2.50))

$$\frac{\partial \eta_1}{\partial t} = \lim_{y \to L/2} \left(v' - U(y) \frac{\partial \eta_1}{\partial x} \right) \tag{3.4}$$

$$\frac{\partial \eta_2}{\partial t} = \lim_{y \to -L/2} \left(v' - U(y) \frac{\partial \eta_2}{\partial x} \right), \tag{3.5}$$

where v' is the y-component of the velocity field linearised about small η_1 and η_2. As before, the limits in (3.4) and (3.5) are required in order to avoid the velocity singularities at the temperature discontinuities: the large velocities always run parallel to the edges and so cancel in the product, leaving evolution of the temperature field on finite time scales.

Juckes (1995) finds an expression for v' and shows that the dynamics of perturbations on each edge of the filament can be split into a contribution from self-propagation and a contribution from interaction with the opposite edge, a process which can be written succinctly in terms of Fourier components:

$$i\frac{d\hat{\boldsymbol{\eta}}}{dt} = \begin{pmatrix} P(\kappa) & I(\kappa) \\ -I(\kappa) & -P(\kappa) \end{pmatrix} \hat{\boldsymbol{\eta}} \equiv \boldsymbol{G}\hat{\boldsymbol{\eta}}, \tag{3.6}$$

where

$$\kappa = kL \tag{3.7}$$

is the non-dimensional wavenumber and the Fourier components of the disturbance are defined by $(\eta_1, \eta_2) = \hat{\boldsymbol{\eta}}(t)e^{ikx}$, where k is the wavenumber of the Fourier component in question. The propagation (P) and interaction (I) coefficients for the SQG filament problem are given by Juckes (1995) as

$$P(\kappa) = \frac{\theta_0}{\pi L}\kappa(\log\kappa + \gamma - \log 2) \tag{3.8}$$

$$I(\kappa) = \frac{\theta_0}{\pi L}\kappa \mathrm{K}_0(\kappa) \tag{3.9}$$

where $\gamma = 0.57721...$ is the Euler constant and K_0 is the modified Bessel function of order zero. The formulation of (3.6) illustrates the similarity to the shielded Rankine vortex problem. Due to the symmetry of this problem (and $\boldsymbol{G}$) the general solution of (3.6) can be written down simply in this case as

$$\hat{\boldsymbol{\eta}}(t) = (\boldsymbol{\mathcal{I}} \cosh\sigma t - i\boldsymbol{G}\frac{\sinh\sigma t}{\sigma})\hat{\boldsymbol{\eta}}(0) \tag{3.10}$$

where $\sigma = \sqrt{\det(\boldsymbol{G})} = \sqrt{I^2 - P^2}$ is the normal mode growth rate and $\boldsymbol{\mathcal{I}}$ is the identity matrix. Note from (3.8) and (3.9) that $\sigma \propto \theta_0/L$ so perturbation growth rates are inversely proportional to the filament width as claimed above.

As before, we use the root mean square wave slope norm, now defined as

$$N(t) = \left(\frac{k}{2\pi} \int_0^{2\pi/k} \left[\left(\frac{\partial \eta_1}{\partial x} \right)^2 + \left(\frac{\partial \eta_2}{\partial x} \right)^2 \right] \mathrm{d}x \right)^{1/2} = \frac{\kappa}{\sqrt{2}} \left| \hat{\boldsymbol{\eta}}(t) \right|, \tag{3.11}$$

to measure the amplitude of disturbances. This norm represents the size of the dominant nonlinear terms in the governing equations, which typically consist of derivatives, and as such is a useful diagnostic for nonlinear development (Dritschel et al. (1991)). The rate of change of N can be shown to be given by

$$\frac{\mathrm{d}N}{\mathrm{d}t} = -2I(\kappa) \frac{\mathrm{Im}(\hat{\eta}_1 \hat{\eta}_2^*)}{|\hat{\boldsymbol{\eta}}|^2} N, \tag{3.12}$$

where $\mathrm{Im}(\cdot)$ represents the imaginary component of the argument. The growth rate therefore takes a maximal value of $I(\kappa)$ for waves of equal amplitude and a phase difference of $\pi/2$, as is common for this type of problem (Heifetz & Methven, 2005). This is the disturbance configuration which undergoes maximum instantaneous growth under this norm. The normal modes, conversely, have the growth rate σ.

As in Section 2.4, to focus on the growth of disturbances we consider the amplification factor of the norm,

$$A(t) = \frac{N(t)}{N(0)}. \tag{3.13}$$

We also consider the singular mode amplification

$$A_{\mathrm{s}}(t) = \max_{\hat{\boldsymbol{\eta}}(0)} (A(t)), \tag{3.14}$$

that is, the value of the amplification factor (3.13) maximised over all initial conditions, and the corresponding singular mode equivalent growth rate,

$$\sigma_{\mathrm{s}} = \log(A_{\mathrm{s}}(t))/t. \tag{3.15}$$

This measure of disturbance growth is plotted in Figure 3.2(a) at various times t for the solution (3.10). Initially (when $\sigma t \ll 1$), $\sigma_{\mathrm{s}} \sim I(\kappa)$ and in the long time limit (when $\sigma t \gg 1$), $\sigma_{\mathrm{s}} \sim \sigma$: the equivalent growth rate collapses onto the normal mode growth rate in the long time limit. This represents the possibility of transient growth at a rate larger than σ initially followed by what is effectively normal mode growth. This process is identical to that discussed in Section 2.4 for the shielded vortices so we do not discuss it further here. It is insightful, however to compare Figures 3.2(a) and 2.8.

3.3 Surface QG filaments in shear

The first problem we consider is the effect of adding an external shear flow to the filament stability problem. We take the simplest case where the shear is aligned with the filament as illustrated in Figure 3.1(b). We find that such a flow can act to stabilise smooth temperature filaments in a manner to be explained, but not the discontinuous 'top-hat' profile.

The shear flow is written

$$(u_r, v_r) = r(y, 0), \tag{3.16}$$

where r is the rate of shear. The shear is adverse, that is, it acts against the shear within the filament, if r has same sign as θ_0 and it is a complementary shear if r has the opposite sign as θ_0 (see Figure 3.1). With this addition, the perturbation evolution is still given by (3.6) with a simple modification to the propagation coefficient,

$$P(\kappa) = \frac{\theta_0}{\pi L}\kappa(\log\kappa + \gamma - \log 2) - \kappa r, \tag{3.17}$$

which represents the modification of the local wave speed due to advection by the shear flow. The analytic solution of (3.10) also holds with this modification and we plot, in Figure 3.2, the corresponding equivalent growth rates, see (3.15), for various shear values.

The figure shows that an adverse shear shifts the unstable normal modes to higher wave numbers thus reducing the wavelength of the most unstable perturbations. Likewise, a complementary shear shifts the unstable normal modes to smaller wave numbers and hence larger scales. The normal mode growth rate curves always lie below the $I(\kappa)$ curve which is not affected by the shear. In contrast to the barotropic vorticity case, there is no critical shear value which stabilises the filament completely: there are always unstable modes, albeit with reduced growth rates.

An estimate for this growth rate can be obtained as follows. Since $\sigma = \sqrt{I^2 - P^2}$, the growing normal modes have wavenumbers near to $\kappa = \kappa^*$ given by the solution to

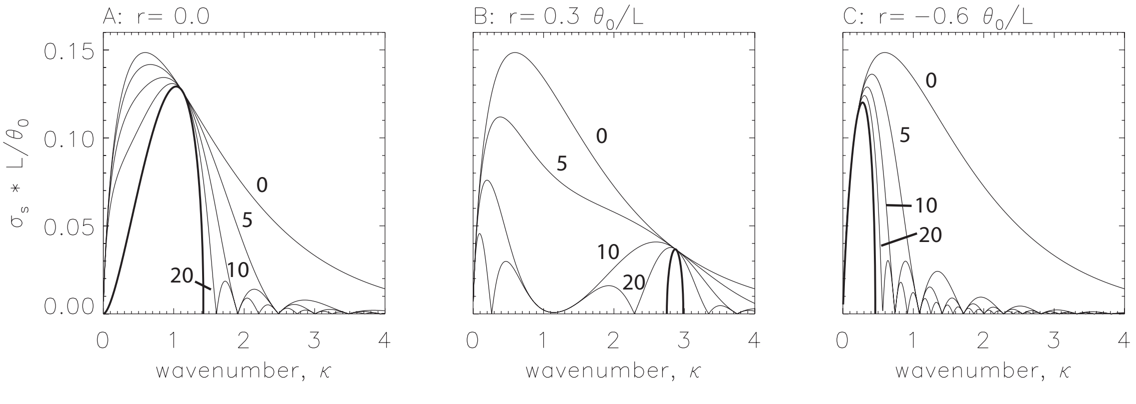

Figure 3.2 Equivalent growth rate values (see (3.15)) for rates of shear $r = 0.0$ (left), $r = 0.3\theta_0/L$ (centre) and $r = -0.6\theta_0/L$ (right). The times plotted are $t = (0, 5, 10, 20)L/\theta_0$ as indicated and the bold line indicates the normal mode growth rate.

$P(\kappa^*) = 0$. That is, $\kappa^* = 2\exp(rL/\pi\theta_0)$. The maximum normal mode growth rate is therefore roughly

$$\begin{aligned} I(\kappa^*) &= \frac{\theta_0}{\pi L}\kappa^* \mathrm{K}_0(\kappa^*) && (3.18) \\ &\sim \frac{\theta_0}{\sqrt{2\pi}L}\sqrt{\kappa^*}\exp(-\kappa^*), && (3.19) \end{aligned}$$

where we have used a common result for the modified Bessel function at large values of its argument: $\mathrm{K}(\kappa) \sim \sqrt{\pi/2\kappa}\mathrm{e}^{-\kappa}$ (Gradshteyn & Ryzhic, 2000). Therefore the growth rate of the instability with a strong shear decays very quickly with the rate of shear, but the instability is not completely destroyed. This does not rule out, however, the possibility of saturation at finite amplitude preventing filament roll-up.

The inability of shear to inhibit normal mode growth of the surface QG top-hat filament is consistent with a consideration of the Fjortoft condition. As discussed in Section 2.1.2, the condition is not useful when there are temperature discontinuities present. Applied to this problem, the condition assures stability provided the basic state velocity profile is anti-correlated with the sign of the temperature gradients at each edge of the filament. Clearly (see Figure 3.1) the velocity singularities at the filament edges prevent this from occurring for any finite shear value.

If instead we consider the case of a filament with slightly smoothed edges, however, then the singularities disappear. Suppose the filament edge is smoothed slightly over a width δL. The peak in the basic state velocity field will then scale as

$$U_{\mathrm{peak}} \sim \frac{\theta_0}{\pi}\log(L/\delta L) \tag{3.20}$$

and the Fjortoft condition will be met when

$$r \sim \frac{\theta_0}{2\pi L}\log(L/\delta L). \tag{3.21}$$

Therefore we conclude that smooth surface QG filaments can be stabilised by suitably strong shearing, the strength of which is dependent on the filament profile.

3.4 Surface QG filaments in strain

3.4.1 Basic considerations

We now turn attention to the effects of an external strain on the stability of surface QG filaments. We will demonstrate that the straining is also a stabilising process in the sense that all linear perturbations eventually decay when there is an external strain present.

However, we will also show that at intermediate times perturbation growth to any specified amplitude can occur. In this sense, the surface QG filament cannot be stabilised by straining. We then draw several remarkable conclusions regarding the formation of vortices by filament instability in a straining flow which have implications for understanding the morphology of surface QG turbulence.

We write the external strain as

$$(u_s, v_s) = s(x, -y), \tag{3.22}$$

where s is the strain rate. The effect of this flow on the basic state of (3.1) is to thin the filament exponentially in the y-direction so that at later times its width is given by $L = L_0 e^{-st}$, where L_0 is the width of the filament at $t = 0$. Note that this increases the instantaneous growth rate of perturbations, which by (3.12) is proportional to θ_0 / L.

The straining also has a direct effect on perturbations which are squashed in the y-direction and stretched in the x-direction. The linear evolution is still given by (3.6) but now with time-varying wave numbers, $k = k_0 e^{-st}$, which correspond to

$$\kappa = \kappa_0 e^{-2st}, \tag{3.23}$$

and each Fourier mode taking the form

$$\boldsymbol{\eta}(x,t) = \hat{\boldsymbol{\eta}}(t) \exp(\mathrm{i} k_0 \mathrm{e}^{-st} x - st). \tag{3.24}$$

The wave slope norm amplification factor of Equation (3.13) becomes

$$A(t) = e^{-2st} |\hat{\boldsymbol{\eta}}|. \tag{3.25}$$

where $\hat{\boldsymbol{\eta}}$ are the Fourier components of both edge perturbations.

We thus see that the strain introduces two competing effects: there is a kinematic decay of perturbations at the constant rate $2s$, which is stabilising, whilst the thinning of the filament causes an exponential increase in the instantaneous perturbation growth rates. In addition to these, the exponential growth of perturbation wavelengths mean that eventually all disturbances will decay.

The analytic solution of (3.10) is not valid for non-zero strain rates so in Sections (3.4.2) and (3.4.3) we resort to numerical integration to analyse the problem in detail. As a first consideration of the combined effects, however, consider the instantaneous growth rates of perturbations. From (3.12) and (3.25) it is clear that the rate of change of N takes a maximum value of $I(\kappa) - 2s$ when there is straining, and therefore for each strain rate there is a critical filament width above which no perturbations can grow,

$$L = L_c = \max_{\kappa} \left(\frac{\kappa \mathrm{K}_0(\kappa)}{2\pi} \right) \frac{\theta_0}{s} \approx 0.0742 \frac{\theta_0}{s}, \tag{3.26}$$

where the maximum value is achieved at non-dimensional wavenumber $\kappa \approx 0.595$ (see Figure 3.2). Note also that in the long time limit, whereby $\kappa \to 0$, all perturbations will decay at the kinematic rate of $-2s$.

The result of (3.26) suggests two regimes for the filament. Either $L < L_c$ initially and there are some perturbations which can grow, or else $L > L_c$ initially and all perturbations initially decay. At the later time

$$t = t_c = \frac{1}{s} \log \left(\frac{L_0}{L_c} \right) \approx \frac{1}{s} \log \left(\frac{1}{0.0742} \frac{s L_0}{\theta_0} \right), \tag{3.27}$$

where L_0 is the initial filament width, there will be some perturbations which can grow. Therefore instantaneous perturbation growth can occur for any strain rate but only after the filament has thinned to the critical width L_c.

Applying this argument to the initial value problem, which we study in detail in Section 3.4.2, we note that the amplitude of a perturbation applied to a wide filament, in the sense that initially $L > L_c$, will have decayed kinematically by the time $t = t_c$. Further, the wavenumber of the perturbation will have decreased. Whether the perturbation can subsequently become large will depend on whether the subsequent growth, which will depend on the wavenumber and initial configuration of the disturbance, is sufficient to overcome this initial decay. Note also that if the filament was perturbed with a further disturbance of amplitude $A = 1$ at time $t = t_c$ then it is possible that this will become large before the initial perturbation, a possibility we consider in Section 3.4.3.

We note briefly the similarity of the result (3.26) with the result of Dritschel et al. (1991) for the barotropic vorticity case who found that perturbation growth on vorticity filaments is prevented if $s > 0.25q_0$, where q_0 is the filament vorticity. Likewise, the condition of (3.26) means that perturbation growth in the surface QG case is prevented if $s > 0.0742\theta_0/L$. The difference here is the factor L which, due to the exponential thinning of the filament, means that the condition cannot be met indefinitely.

In the next section we investigate the initial value problem by numerically integrating the linear equations (3.6). The integrations provide the evolution of perturbation amplitudes with time and we are able to infer whether the growth predicted by (3.26) is sufficient to overcome the initial kinematic decay.

3.4.2 Initial value problem

We scale time with respect to the constant strain rate, s,

$$T = st, \tag{3.28}$$

leaving only two non-dimensional parameters in the linear equations: the initial values of L/L_c and $\kappa = kL$ which we write as L_0/L_c and $\kappa_0 = k_0 L_0$ respectively. In addition the solution depends on the initial structure of the perturbation, $\hat{\boldsymbol{\eta}}(0)$, but here we only consider the maximum amplification, $A_{\mathrm{s}}(t)$, introduced in (3.13). In this section we follow closely the procedure of Dritschel et al. (1991).

The maximum amplification, $A_{\mathrm{s}}(t)$, can be calculated from numerical integrations using the method of Dritschel et al. (1991) as follows. For given values of L_0 and κ_0 we numerically integrate the system just twice with different initial conditions to obtain linearly independent solutions $\hat{\boldsymbol{\mu}}(t)$ and $\hat{\boldsymbol{\nu}}(t)$. As the equations are linear, any solution $\hat{\boldsymbol{\eta}}(t)$ can be obtained from linear combinations of the form:

$$\hat{\boldsymbol{\eta}}(t) = \alpha\hat{\boldsymbol{\mu}}(t) + \beta\hat{\boldsymbol{\nu}}(t) \tag{3.29}$$

where α and β are complex constants. $A(t)$ then takes the form

$$A(t) = \frac{e^{-2st}}{|\hat{\boldsymbol{\eta}}(0)|}\left(|\alpha|^2|\hat{\boldsymbol{\mu}}|^2 + |\beta|^2|\hat{\boldsymbol{\nu}}|^2 + 2\mathrm{Re}(\alpha\beta^*\hat{\boldsymbol{\mu}}\cdot\hat{\boldsymbol{\nu}}^*)\right)^{\frac{1}{2}} \tag{3.30}$$

which can be maximised over all α and β. Choosing $\hat{\boldsymbol{\mu}}$ and $\hat{\boldsymbol{\nu}}$ to satisfy $\hat{\boldsymbol{\mu}}(0)\cdot\hat{\boldsymbol{\nu}}^*(0) = 0$ simplifies the expressions since then the initial condition simplifies to $|\alpha|^2|\hat{\boldsymbol{\mu}}(0)|^2 + |\beta|^2|\hat{\boldsymbol{\nu}}(0)|^2 = |\hat{\boldsymbol{\eta}}(0)|^2$ which, combined with the phase invariance of the dynamics, means we can write

$$\alpha = \frac{|\hat{\boldsymbol{\eta}}(0)|}{|\hat{\boldsymbol{\mu}}(0)|}\mathrm{e}^{i\gamma}\cos\delta \tag{3.31}$$

$$\beta = \frac{|\hat{\boldsymbol{\eta}}(0)|}{|\hat{\boldsymbol{\nu}}(0)|}\mathrm{e}^{-i\gamma}\sin\delta \tag{3.32}$$

and maximise (3.30) with respect to the real constants γ and δ. The maximum of A given by this calculation is

$$A_{\mathrm{s}}(t) = \frac{\mathrm{e}^{-2st}}{\sqrt{2}}\left(\frac{|\hat{\boldsymbol{\mu}}(t)|^2}{|\hat{\boldsymbol{\mu}}(0)|^2} + \frac{|\hat{\boldsymbol{\nu}}(t)|^2}{|\hat{\boldsymbol{\nu}}(0)|^2} + \left[\left(\frac{|\hat{\boldsymbol{\nu}}(t)|^2}{|\hat{\boldsymbol{\nu}}(0)|^2} - \frac{|\hat{\boldsymbol{\mu}}(t)|^2}{|\hat{\boldsymbol{\mu}}(0)|^2}\right)^2 + 4\frac{|\hat{\boldsymbol{\mu}}(t)\cdot\hat{\boldsymbol{\nu}}^*(t)|^2}{|\hat{\boldsymbol{\mu}}(0)||\hat{\boldsymbol{\nu}}(0)|}\right]^{\frac{1}{2}}\right)^{\frac{1}{2}}. \tag{3.33}$$

To simplify the integration numerics we use alternative variables defined by $(\hat{\lambda}_1, \hat{\lambda}_2) = (\hat{\eta}_1 + \hat{\eta}_2, i(\hat{\eta}_1 - \hat{\eta}_2))/\sqrt{2}$ as then all the coefficients in (3.6) are real. The natural choices of $\hat{\lambda}(0) = (1,0)$ and $(0,1)$ for the two linearly independent solutions correspond to

$$\hat{\mu}(0) = \frac{1}{\sqrt{2}}(1,1) \tag{3.34}$$

$$\hat{\nu}(0) = \frac{i}{\sqrt{2}}(-1,1) \tag{3.35}$$

and this is what we use.

The integration scheme used is a second order semi-implicit scheme. Accuracy is ensured by systematically reducing the time step until convergence is achieved. Integrations have been performed systematically over a wide range of parameter space, $(L_0/L_c, \kappa_0)$, and we now discuss the results.

As an initial illustration, Figure 3.3 shows the evolution of A_s as a function of the scaled time, T, for $L_0 = 0.8L_c$ and several different wave numbers, κ_0. In all simulations the long time behaviour is that of decay at the kinematic rate. In some cases, however, there is intermediate growth prior to this decay and we are interested in the magnitude of this growth. As such, we define $A_{\max}(L_0/L_c, \kappa_0)$ as the maximum value of A_s achieved throughout the integration period for each value of $(L_0/L_c, \kappa_0)$. $A_{\max}$ is plotted in Figure 3.4A for a wide range of $(L_0/L_c, \kappa_0)$ values and the corresponding time at which this occurs, that is, $T_{\max}$ such that $A_s(T_{\max}) = A_{\max}$, is shown in Figure 3.4B. Note the logarithmic scales in these plots.

An important feature of Figure 3.4 is that it appears that for all values of the initial width, L_0, there are wave numbers which have large $A_{\max}$ values and therefore may

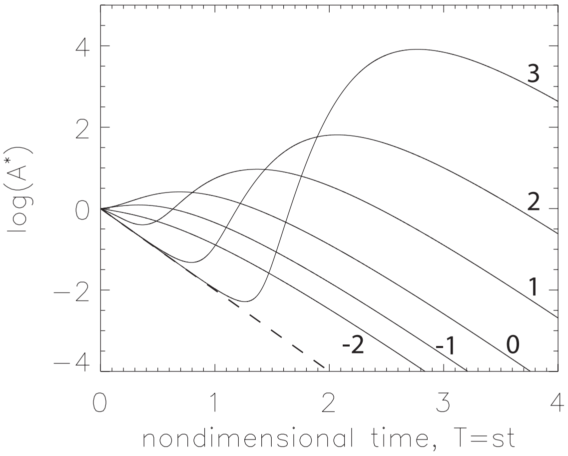

Figure 3.3 Evolution of $\log(A_s(T))$ for $L_0 = 0.8L_c$ and $\kappa_0 = \exp[-2, -1, 0, 1, 2, 3]$, labelled as -2 to 3 respectively. Also shown by the dashed line is the kinematic decay $\log(A_s(T)) = -2T$.

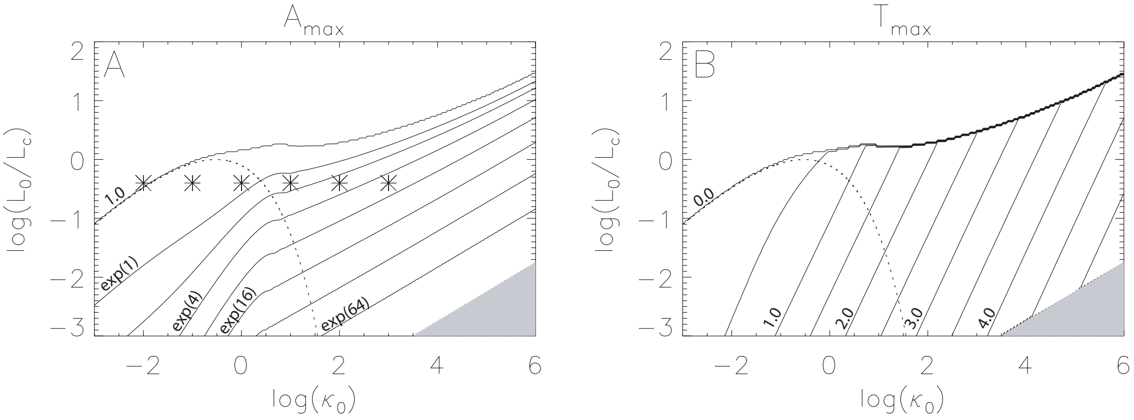

Figure 3.4 Panel A: Contours are A_{max}, the dashed line is $L_0 = (\theta_0/s)\kappa_0 \mathrm{K}_0(\kappa_0)/2\pi$ which represents the boundary between positive and negative initial growth (see (3.26)), the symbols indicate the parameter values used in Figure 3.3, the shaded region is not numerically accessible with our method. Panel B: Contours are T_{max}.

be unstable in the sense that nonlinear terms may be important and possibly cause the filament to 'roll-up'. The initial wave numbers, κ_0, of perturbations which grow large increase with L_0, as expected. This is due to the following combined effects: (i) the intermediate period of growth seen in Figure 3.3 occurs when $\kappa = O(1)$ and (ii) perturbation growth rates are larger on thinner filaments. Therefore the largest A_{max} values are achieved by the largest κ_0 experiments for which the filaments are very thin by the time $\kappa = O(1)$. Note that, despite this prediction of nonlinear instability at all strain rates, an initial disturbance of any given wavenumber can be stabilised if a suitably strong strain is applied. We also note in passing that the increase in A_{max} with κ_0 for a given L_0 appears from Figure 3.4 to be doubly exponential. This means that if a filament was perturbed by noise at all scales it can only remain stable if the power of the noise also decreases like (or faster than) a double exponential at small scales. In particular, in any power-law turbulence situation there is enough small scale noise to cause filament roll-up.

We next consider an alternative diagnostic from the integrations: the smallest time at which a certain threshold amplitude, A_{th}, is achieved. That is, the first T_{th} such that $A_{\mathrm{s}}(T_{\mathrm{th}}) = A_{\mathrm{th}}$. The motivation for this approach is that the amplification factor A is a measure of the importance of nonlinear terms in the corresponding full nonlinear problem and as such filament 'roll-up' may be expected to occur when this reaches some threshold value. Without knowing this value, which will of course depend on the absolute size of the initial perturbation, we calculate our results for a range of different

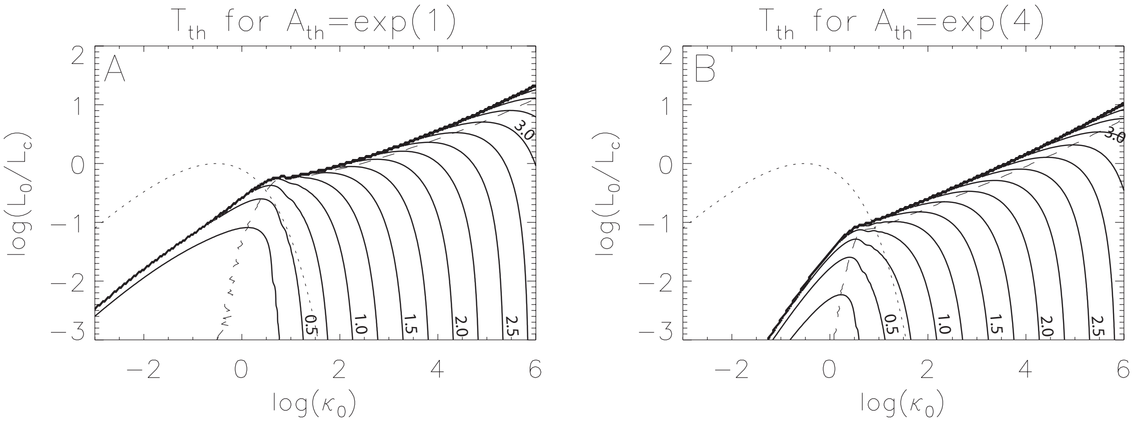

Figure 3.5 T_{th} values for threshold amplitudes $A_{\mathrm{th}} = e^1$ (panel A) and $A_{\mathrm{th}} = e^4$ (panel B). The dashed line indicates the minimum values.

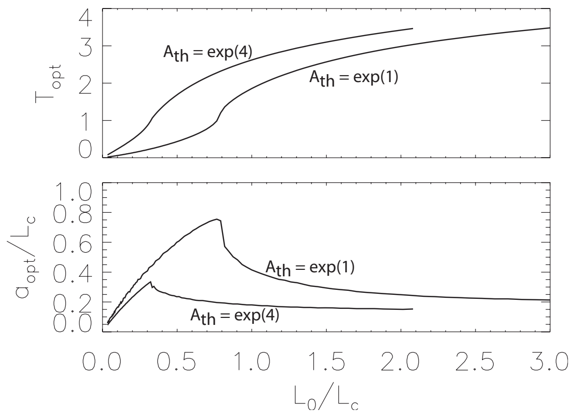

Figure 3.6 Upper panel: T_{opt} values for the threshold amplitudes $A_{\mathrm{th}} = e^1$ and $A_{\mathrm{th}} = e^4$. Lower panel: a_{opt} values for the same threshold amplitudes, see (3.36).

threshold amplitudes.

Figure 3.5 shows T_{th} for the cases $A_{\mathrm{th}} = e^1 = 2.72...$ and $A_{\mathrm{th}} = e^4 = 54.6....$ The plots show that for each L_0 there is an optimal initial wavenumber, $\kappa_{\mathrm{opt}}(L_0; A_{\mathrm{th}})$, which achieves the threshold amplitude first. This is marked on the plots by the dashed lines. Figure 3.6A shows the corresponding optimal times, $T_{\mathrm{opt}}(L_0, A_{\mathrm{th}})$, that is the times at which the optimal wavenumber perturbations reach the threshold amplitudes, as a function of L_0. As expected, the $A_{\mathrm{th}} = 4$ case has larger T_{opt} values than the $A_{\mathrm{th}} = 1$ case. Also shown, in Figure 3.6B, is an estimate of the radii of vortices formed from the instability, $a_{\mathrm{opt}}(L_0, A_{th})$. This is defined such that the area of of one vortex is equal to the area of filament contained within one wavelength of the optimally growing mode:

$$\pi a_{\mathrm{opt}}^2 = \frac{2\pi}{\kappa_{\mathrm{opt}}(L_0)} L_0^2. \tag{3.36}$$

Both panels of Figure 3.6 show a regime change at a certain value of L_0, which depends on the choice of A_{th}. A comparison with Figure 3.5 suggests the interpretation that for small L_0 values perturbations can grow immediately whereas for large values none of the initially growing perturbations reach A_{th}. Instead the first perturbation to do so is an initially decaying one which must first overcome the kinematic decay. The result is that for filaments with large L_0 values the resultant vortices are, according to this theory, significantly smaller than the initial filament width.

3.4.3 Continued perturbations

We now consider a different approach to the problem, that of a filament under continued perturbations. By this we mean a filament which is perturbed at each instant in time during the integration. We still assume each perturbation to evolve independently of the others but expect that, since the quasi-stationary growth rate increases in time, a perturbation applied at a time $T = \tau > 0$ may grow and reach the threshold amplitude A_{th} before a perturbation applied at time $T = 0$.

Note that the evolution of a perturbation applied at $T = \tau$ is equivalent to that of an initial value problem with initial value of L given by $L_0 e^{-\tau}$ and therefore all the information we require to test this hypothesis is included in the initial value integrations already performed.

The motivation for the continued perturbation approach comes from the fact that the wavenumber of the optimally growing modes is often very large. A filament with initial width $L = 3L_c$ has, for $A_{\text{th}} = e^4$, an optimally growing mode of initial wavenumber $\kappa_0 \approx e^6$ and this appears to increase for stronger strain rates (see Figure 3.5). Clearly a consideration of numerical resolution or other diffusive effects may make these modes unrealistic. Further, defining the initial condition of a filament in a turbulent flow is not a well-defined procedure since there is no time $t = 0$. Instead we suppose that the perturbations which cause filament roll-up are in practice generated throughout the straining period through either small irregularities in the straining field or else internal variations in the basic state which are not captured by our simple ‘top-hat’ model.

To calculate whether a later perturbation can grow to a particular threshold amplitude before an initial perturbation consider minimising the sum of waiting until the perturbation release time τ and the subsequent optimal growth time for a filament of width $L_0 e^{-\tau}$, over all possible release times:

$$T_{\text{cp}} = \min_{\tau < T_{\text{opt}}(L_0)} \left(\tau + T_{\text{opt}}(L_0 e^{-\tau}) \right). \tag{3.37}$$

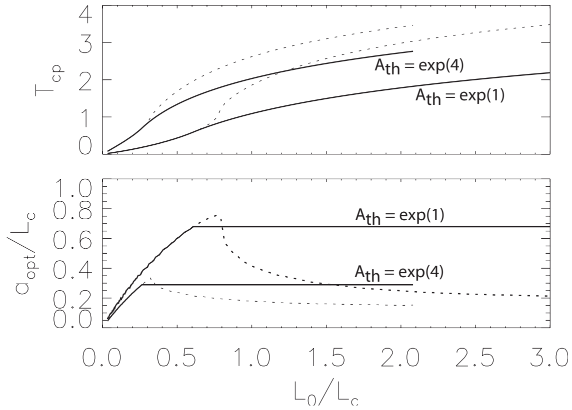

Figure 3.7 Upper panel: T_{cp} values for the threshold amplitudes $A_{th} = e^1$ and $A_{th} = e^4$ (solid lines), dashed lines are from Figure 3.6. Lower panel: a_{cp} values for the same threshold amplitudes, see (3.38).

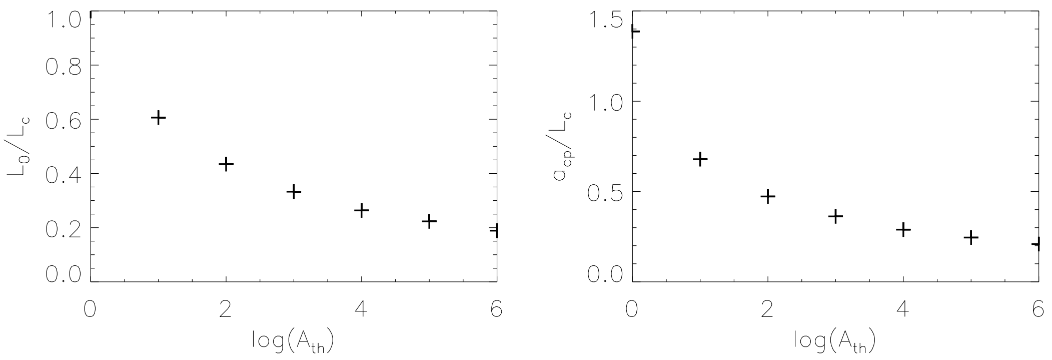

Figure 3.8 Panel A: Critical widths vs threshold amplitude, see text. Panel B: Resultant vortex radii vs threshold amplitude, see text.

Either the minimising τ is zero and it is the initial perturbation which is important or else the minimising value is positive and it is a perturbation applied later which reaches the threshold amplitude first.

Figure 3.7A shows T_{cp} as a function of L_0 for both $A_{th} = \exp(1)$ and $A_{th} = \exp(4)$. For L_0 larger than some critical value T_{cp} is indeed smaller than T_{opt} indicating that later perturbations can be important. Figure 3.7 shows the corresponding vortex radii of the first perturbations to reach the threshold amplitude, now defined by

$$\pi a_{cp}^2 = \frac{2\pi}{\kappa_{opt}(L_0 e^{-\tau^*})}(L_0 e^{-\tau^*})^2, \tag{3.38}$$

where τ^* represents the minimising τ value from (3.37). This is constant for precisely the same L_0 values and from this we infer the following: if a filament is initially wide in a sense made precise below then it has no ‘memory’ and will become unstable only once it has thinned to a critical width which is independent of L_0. The resultant vortices will have radii proportional to θ_0/s, again independent of how the filament was formed.

The relevant width in this statement refers to the transition in Figure 3.7 between the regime whereby initial perturbations dominate and the regime whereby later perturbations dominate, which depends on the value chosen for A_{th}. Figure 3.8A shows the critical width for various A_{th} values, and the the resulting vortex radii are shown in Figure 3.8B.

Both L_0/L_{c} and the vortex radii values reduce to zero for large A_{th}. For $A_{\text{th}} = e^4 \approx 54.6$ the theory predicts instability to occur on a wide filament once the width has reduced to $L \approx 0.3L_{\text{c}}$ and the resultant vortices to have radii $a \approx 0.3L_{\text{c}}$.

3.5 Discussion

Straining and shearing tend to inhibit the development of various fluid dynamical instabilities. However, we have shown that straining is unable to stabilise temperature filaments in the surface quasi-geostrophic system since it acts to thin filaments and thus increase the instantaneous growth rates of perturbations. Shearing is also unable to stabilise surface QG ‘top-hat’ filaments and this is due to the velocity singularities they induce.

For the straining case our numerical integrations show that the increase in perturbation growth rate is large enough that following the evolution of a single perturbation is not the fastest way to reach large amplitude. Instead, by considering many perturbations applied continuously in time, we found that there is an optimal width for applying a perturbation such that it grows to a given threshold amplitude first. According to this simple theory, the size of the resultant vortices is independent of the previous history of the filament, instead being proportional to θ_0/s, with θ_0 the temperature anomaly of the filament and s the strain rate.

We now draw several qualitative conclusions from the results of this chapter. The first is that, unlike the 2-d Euler case, surface QG filaments do not have to move away from the region of straining before becoming unstable. This is in contrast to the commonly head view (see Section 3.1.1) that filament instability only occurs when the straining is removed and is particularly applicable to the behaviour of stratospheric intrusions.

Second, recall the result from Section 2.5 concerning the effects of straining on the shape of vortices. We noted there that a straining of rate s will act to deform surface QG vortices of radius a into ellipses with aspect ratios proportional to θ_0/as, see (2.102), which, at first sight, appears to violate the possibility of a statistically steady state which is scale independent. However, we have shown here that vortices forming from filaments in the same strain field will have radii scaling as $a \propto \theta_0$, making the two results consistent.

Another comment worth making concerns the energy spectra of the fluid motions. As discussed in the Introduction, surface QG and 2-d Euler turbulence exhibit different energy spectra. As pointed out there, the different power laws predicted for the surface kinetic energy in the enstrophy inertial range are due to two factors. One is a purely kinematic effect due to the smoothness of the inversion operators and the other is due to the dynamics which occurs. It seems likely that the qualitative difference in behaviour observed in this chapter is responsible for this second factor. Whether a given filament rolls up or not will clearly influence the distribution of enstrophy at different scales. A roll-up situation will quickly move some enstrophy to small scales whilst 'trapping' most of it in the vortices formed, whereas the enstrophy associated with a non-roll up filament will continue moving gradually to smaller scales under the action of the strain. It may be possible to develop a turbulence power law spectrum based on this observation.

Next, we note the implications of these results on the finite-time temperature discontinuity formation problem mentioned earlier. It is important to note that the idealised 'top-hat' profiles used for this work already have temperature discontinuities present. However, it is still an interesting question to ask if the sequence of roll-ups on the braids between vortices can develop to infinitely small scales in finite time, as this qualitative feature may well carry over to the case of an initially smooth filament. The work of this chapter allows an interesting insight into this problem. We have shown that straining cannot stabilise filaments indefinitely, suggesting that it is not possible for the cascade to small scales to be stopped by this process. What our work has highlighted, however, is the importance of the initial perturbation amplitude on the time taken for instability to occur. It is possible that as smaller scales are reached, the filaments that are formed are 'cleaner' than their ancestors to the extent that the total time taken for the instability to reach small scales is finite.

Finally, we make a comment regarding the influence of diffusion on the stability of a filament under strain, something which we have not discussed in detail before. Diffusion will act to smooth the 'top-hat' filaments studied here possibly making the method unsuitable. However, it can be shown analytically that the combined effects of straining and diffusion introduces a critical filament width

$$l_\nu = \left(\frac{\nu}{s}\right)^{1/2}, \tag{3.39}$$

where ν is the diffusion coefficient, above which diffusion plays a minor role. We therefore expect filament instability to occur readily if $L_\mathrm{c} \gg l_\nu$, or alternatively, if filament amplitudes typically satisfy

$$\theta_0 \gg \frac{\sqrt{\nu s}}{C}, \tag{3.40}$$

where $C \approx 0.0742$. For filaments satisfying these criteria, diffusion can be ignored. Clearly any form of diffusion will prevent finite-time temperature discontinuity formation.

Chapter 4:

BAROCLINIC INSTABILITY

4.1 Introduction

In this final work chapter we move away from pure surface QG dynamics and instead consider a new analytic model of baroclinic instability. By definition, baroclinic instability involves dynamical interactions between different vertical levels of the atmosphere and so the effectively single-layer surface QG model in isolation is not suitable and must be extended. This is done by introducing a rigid upper boundary to the domain, representing the tropopause, whilst still keeping the assumption of zero interior QGPV. The resulting model, sometimes called 'uniform PV dynamics' (Blumen, 1978), consists of two dynamical components, namely the temperature distributions on both the upper and lower boundaries, which we write as θ_{t} and θ_{s} respectively.

The setup we study here is sketched in Figure 4.1. It takes the form of two vertically aligned temperature patches, one at the surface and one at the tropopause. Together these crudely represent the extra-tropical dynamics of an entire hemisphere and as such we take the patches to be negative temperature anomalies. Recall that the effective PV associated with a surface cold anomaly is negative whereas that associated with a tropopause cold anomaly is positive so this setup includes the opposing PV gradients crucial for instability from the Charney-Stern-Pedlosky condition (Vallis, 2006). We discuss the stability condition further below.

The original motivation for this study came from the recent paper of Smy & Scott (2009). Their numerical study investigates the dynamical coupling between the stratosphere and troposphere by considering the effect of direct perturbations to the stratospheric potential vorticity distribution on the evolution of baroclinic instability in the troposphere. The setup they use for the tropospheric part of their model is very similar to that of Figure 4.1. Their simulations show baroclinic instability developing around the edges of the fronts in Figure 4.1. The theory we developed in Chapter 2 for the linear dynamics of temperature patches allows analytic progress to be made on this instability problem. There are however differences between the setup of Figure 4.1 and that of the Smy & Scott (2009) simulations so no direct comparisons can be made. For instance, their model uses a more realistic setup with an exponential decaying reference density profile, and it also has a region above the troposphere with a larger static stability, representing a stratosphere.

In this chapter we perform the linear stability analysis of the problem illustrated by Figure 4.1 in some detail and also present some of our own numerical simulations. The study complements that of Smy & Scott (2009) by providing an analytic analysis of the instability. Our numerical simulations were performed using the surface QG code described in Section 1.3.4, extended so as to model the two boundaries coupled together. Details of this are given below. The reasons for running the code are two-fold. Firstly, as a basic verification of the linear theory. Secondly, to study the nonlinear behaviour of the instability.

The chapter is organised as follows. Section 4.2 is used to outline some details of previous analytic models of baroclinic instability to show how our new model differs from them. In Sections 4.3 and 4.4 we then introduce and develop the linear theory for our model and in Section 4.5 we present the numerical simulations.

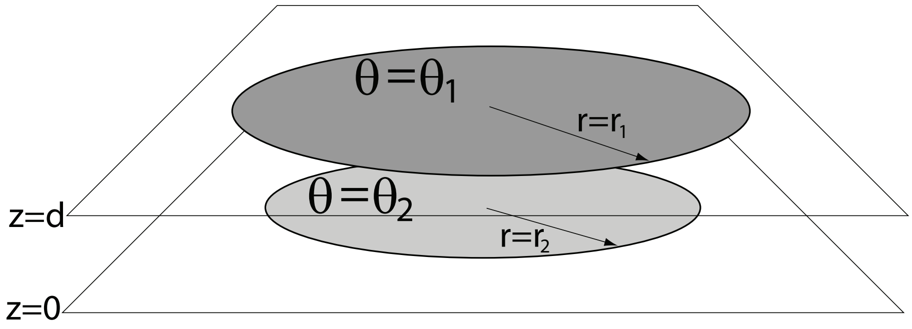

Figure 4.1 A sketch of the baroclinic instability setup studied in this chapter. The light and dark shaded ellipses represent patches of anomalous temperature on the lower and upper boundaries respectively.

4.2 Previous models of baroclinic instability

The two archetypal, analytical models of baroclinic instability in a continuously stratified atmosphere are those of Charney (1947) and Eady (1949). The model of Eady takes the uniform PV setup with a uniform temperature gradient on each boundary as the basic state. Each boundary therefore supports edge waves which both propagate along the boundaries as well as interacting with the opposing wave to form the instability. This interpretation of the dynamics is discussed in detail by Davies & Bishop (1994). The mathematical structure is essentially the same as that studied already in this thesis whereby the propagation and interaction of each wave can be described in terms a 2×2 matrix equation of the form (2.85). However, Davies & Bishop (1994) choose a more intuitive, but nonlinear, form for the equations. The so-called counter-propagating-Rossby wave (CRW) formulation instead focuses explicitly on the amplitudes and phases of each wave (see the series of papers : Heifetz et al. (2004a), Heifetz et al. (2004b), Methven et al. (2005a) and Methven et al. (2005b) for a comprehensive description of this approach). Below we derive both formulations of the problem studied here.

The Charney model uses an atmosphere with a uniform temperature gradient at the lower boundary but which is unbounded above. Crucially, the interior potential vorticity is taken not to be uniform, but rather a linear function of latitude. Some of the associated interior Rossby waves have the correct phase speeds to interact with the surface edge waves and develop an instability.

It is interesting to note that these two models, historically the first two to be fully investigated and understood, both take basic states formed from uniform potential vorticity gradients. This is presumably because the simple structure allows the key mechanisms of the instability to be understood. It also points towards the reason why the atmosphere does not usually exhibit its meridionally smooth radiatively balanced temperature profile. However, an arguably more appropriate setup would be to use a basic state in which the regions of significant potential vorticity gradient are localised into frontal structures, a viewpoint reminiscent of the earlier conceptual models of baroclinic instability developed by the Bergen school. To our knowledge, a full mathematical treatment of such a problem was only first presented by Juckes (1998). In that study a uniform potential vorticity setup was considered with no temperature gradients on the boundaries except for a straight temperature discontinuity, i.e. a front, on each boundary. Disturbances, that is, perturbations to the positions of the fronts, can propagate along each front and interact between the fronts, in much the same way as the edge waves in the

Eady model propagate along the uniform temperature gradient.

In fact, the Eady model and the Juckes model produce remarkably similar linear dynamics. Figures 4.2 (a) and (b) show the normal mode growth rates calculated for the two models. The two growth rate curves are qualitatively very similar. Both models have long waves which are unstable and a short wave cut-off beyond which disturbances are stable. The wavenumbers on the plots are both scaled by the model depth, d, so are directly comparable. The magnitudes of the growth rates, however, cannot be compared directly between the models. The Eady growth rates have been scaled by $\Lambda f/N$, where Λ is the meridional temperature gradient (using the temperature scaling used throughout this thesis, defined in (1.16)). The Juckes growth rates have been scaled by $(\theta/d)f/N$ where θ is the frontal temperature jump and d the tropopause height. The wavenumbers of the short wave cut-offs are similar, both lying in the range $2-2.5$ which corresponds to wavelengths $\approx 3d$. The scaled values of the maximum growth rates are also similar, both being in the range $0.3-0.35$, meaning that the instabilities develop at similar rates if the frontal temperature jump of the Juckes model is equal to the meridional change in temperature over a distance of one model depth.

Taken together, these two models provide two insightful opposing viewpoints of the same physical mechanism. However, there is one major constraint that both of these models suffer from and that is that due to their infinite meridional extent. They are

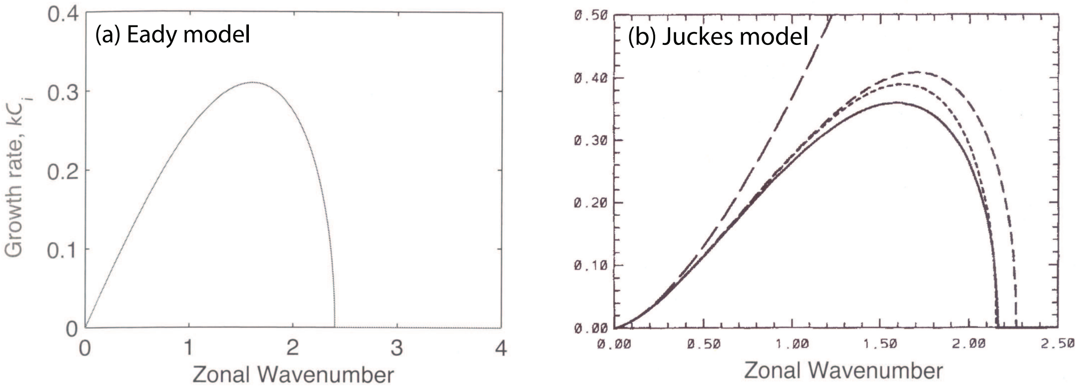

Figure 4.2 Panel (a): Normal mode growth rates for the Eady model (taken from Vallis (2006)). Panel (b): The solid line is the normal mode growth rates for the Juckes model, the other lines are not relevant here (taken from Juckes (1998)). The scalings used are discussed in the text.

required to have equal temperature gradients on the upper and lower boundaries. This is related to the condition of (1.24) discussed in Section 1.3.1. There is therefore always a symmetry between the upper and lower boundaries. If the model is turned upside down then exactly the same evolution will ensue. This strongly constrains the possible nonlinear behaviours produced by the instability, making neither case very realistic. The model studied in this chapter is an extension of the Juckes model which extends it to circular geometry thereby removing this constraint. A much wider range of basic states is possible and the circular geometry results in a more realistic nonlinear development of the instability.

The Charney-Stern-Pedlosky stability condition. Finally, for completeness, we note the famous CSP stability condition referred to above. The condition applies to all of the setups discussed above. It is in fact the three-dimensional QGPV analogue to the Rayleigh condition, and as such can be derived from a consideration of conservation of momentum, just as we did for the surface QG version of Section 2.1.2.

Starting from the domain integral of zonal momentum (c.f. (1.34))

$$M = \int u \, \mathrm{d}V \tag{4.1}$$

and noting that

$$\begin{aligned} u &= -\nabla\psi \cdot \nabla y && (4.2) \\ &= -\nabla \cdot (y\nabla\psi) + y\nabla^2\psi && (4.3) \end{aligned}$$

gives

$$M = \int y \left(\int_0^d q(x,y,z)\,\mathrm{d}z + \theta_s(x,y) - \theta_t(x,y) \right) \mathrm{d}x\,\mathrm{d}y \tag{4.4}$$

in a similar fashion to the expression (1.37).

By the same arguments as those presented in Section 2.1.2, that is, writing this expression in terms of contour perturbations, we arrive at the standard result that there must be opposing PV gradients somewhere in the domain. Either between any of the three components (the surface temperature, the interior QGPV or the upper boundary temperature) or within any one of the components. The Eady and Juckes models achieve instability through a compensation of the first two terms in parentheses in (4.4) whereas in the Charney model it is achieved though the second and third terms. This same formulation can be applied for the circularly symmetric case studied in this section, but using the angular momentum expression of (1.37). The analogous result is obtained.

4.3 The new model: preliminaries

In this section we describe the new model of baroclinic instability and derive its linear stability characteristics. This is done by closely following the method of Section 2.4 for the surface shielded Rankine vortex. The new model of baroclinic instability described here is most similar to that of Juckes (1998). We consider a uniform PV, Boussinesq, quasi-geostrophic atmosphere which is bounded above and below by rigid horizontal boundaries at heights $z = 0$ and d. Each boundary contains only a circular region of uniform anomalously cool temperature. That is, the basic state studied is given by the equations

$$\nabla^2\psi = 0 \qquad \text{in} \quad 0 < z < d \tag{4.5}$$

$$\text{with} \qquad \theta_s = \frac{\partial\psi}{\partial z}\bigg|_{z=0} = \begin{cases} \theta_2 & \text{for} \quad r < r_1 \\ 0 & \text{for} \quad r > r_1 \end{cases} \tag{4.6}$$

$$\text{and} \qquad \theta_t = \frac{\partial\psi}{\partial z}\bigg| = \begin{cases} \Lambda d + \theta_2 & \text{for} \quad r < r_2 \\ \Lambda d & \text{for} \quad r > r_2 \end{cases}, \tag{4.7}$$

with θ_1 and θ_2 both negative constants and Λ is the background vertical temperature gradient. Recall that a cold tropopause anomaly corresponds to a positive PV anomaly whereas a cool surface corresponds to a negative PV anomaly.

This setup is a 3-d extension to that of Juckes (1998) in that it models the instability produced by the interaction of two surface QG frontal waves. There are two main benefits of this extension. The first is that the temperature jumps at the fronts are no longer required to be equal, as we show below, and the second is that the circular geometry allows a more realistic nonlinear development of the instability. The aim is to use this simple (both conceptually and computationally) model to understand better the behaviour of breaking waves in the atmosphere.

Before analysing this model we briefly highlight here that this model continues to adopt the condition of a uniform reference density field used throughout the thesis (see Section 1.2). For this large-scale model of the atmosphere it would be more appropriate to use an exponentially decaying function of the form

$$\rho_0 \propto \exp^{-z/H} \tag{4.8}$$

to take account of the reduced density at upper levels. However, performing this calculation is beyond the scope of the thesis. There is recent work studying the problem of interior QG dynamics with this density profile (Scott & Dritschel (2005)), and it would be an interesting extension to the work of this chapter to perform the analysis presented here with the more general model. We would expect there to be qualitative differences, particularly in the wave-breaking behaviour, because using the density profile (4.8) removes the up-down symmetry of the system.

4.3.1 The surface Rankine vortex revisited

Before analysing the problem (4.5)-(4.7) directly we note down some useful formulae which could have been included in Chapter 2 but were omitted for clarity. In that chapter we introduced the surface Rankine vortex and derived the dispersion relation for disturbances to its edge. As part of the process we also derived, in Section 2.3.1, the associated basic state surface velocity field (see (2.37)). In this chapter we require the corresponding full three dimensional velocity and temperature fields so we note them here for reference.

From the discussion of Section 2.1.1, the full three dimensional streamfunction is given by multiplying the integrand of (2.3) by $e^{-k|z|}$:

$$\Psi(r,z) = -\theta_0 a \int_0^\infty \frac{\mathrm{J}_1(ka)}{k} \mathrm{J}_0(kr) e^{-k|z|}\,\mathrm{d}\kappa. \tag{4.9}$$

Following the discussion there, the corresponding azimuthal velocity field, $U = \partial\Psi/\partial r$, is

$$U(r,z) = \theta_0 \int_0^\infty \mathrm{J}_1(\kappa)\mathrm{J}_1(\kappa r/a) e^{-\kappa|z|/a}\,\mathrm{d}\kappa \tag{4.10}$$

and the full temperature field, $\Theta = \Lambda z + \partial\Psi/\partial z$, is

$$\Theta(r,z) = \Lambda z + \theta_0 \mathrm{sgn}(z) \int_0^\infty \mathrm{J}_1(\kappa)\mathrm{J}_0(\kappa r/a) e^{-\kappa|z|/a}\,\mathrm{d}\kappa. \tag{4.11}$$

These both reduce to the original surface-only expressions (2.35) and (2.32) when $z = 0$ (with the definition $\mathrm{sgn}(0) = +1$).

Figure 4.3 shows an illustration of these integrals which have been evaluated numerically. The plot should be compared to Figure 2.4(a) which shows only the surface values of the velocity field. Figure 4.3 shows that the singularity at the patch edge is indeed confined to the surface. The plot is scaled so that r and z increments are equal: it displays clearly the fact that the wind field has a shape aspect ratio near to one, despite the PV distribution being infinitely thin. Finally, the temperature field away from the surface exhibits the usual feature whereby the isentropes curve down towards the '+'ve PV anomaly, consistent with the wind field through thermal wind balance. The figure should be compared to Figure 16 of Hoskins et al. (1985) which shows a similar setup.

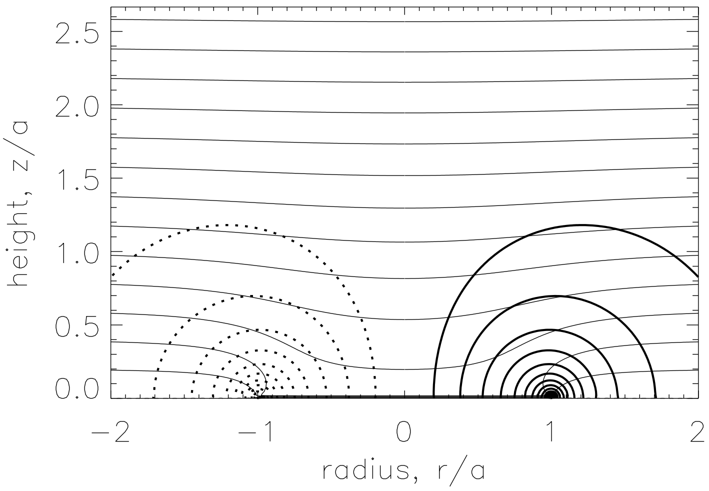

Figure 4.3 Full 3-d azimuthal velocity and temperature fields for the surface Rankine vortex, given by (4.10) and (4.11) respectively. The heavy contours show the velocity field with a contour interval of $0.1\theta_0$ (negative is dashed). The light contours show the temperature field with a contour interval of $0.4\theta_0$. The background temperature gradient is $\Lambda = 2\theta_0/a$.

Their fields were calculated numerically but using a more accurate balance relationship than the QG inversion used here.

4.3.2 The capped surface QG Rankine vortex

As a first step to constructing the new baroclinic instability model of (4.5)-(4.7), we now extend the analysis of Chapter 2 to the setup of capped surface QG dynamics: instead of inverting the surface temperature field in an unbounded atmosphere we put a rigid lid at height $z = d$. The boundary condition applied at the lid is that the temperature is constant or, equivalently, that the vertical wind shear is zero. This, then, represents the surface contribution to the new baroclinic instability model introduced above.

The model is of course symmetric so the tropopause contribution is simply given by a similar PV anomaly at the tropopause level. In this sense, the capped surface QG Rankine vortex is a crude model of the jet stream and the dynamics of perturbations to it, which we study in this subsection, can be interpreted as a planetary scale Rossby wave dispersion relation. Later we construct the full model by superposing two such patches, one at the lower surface and one at the lid.

The uniform temperature boundary condition is achieved by taking the expression

(1.25) for the inverse Fourier transform of the surface temperature field and multiplying the integrand by the factor

$$\frac{\sinh(|\mathbf{k}|(d-z))}{\sinh(|\mathbf{k}|d)}. \tag{4.12}$$

This is the unique linear combination of the exponentials $e^{-|\mathbf{k}|z}$ and $e^{|\mathbf{k}|z}$ which satisfies the joint constraints of being equal to unity at $z = 0$ and vanishing at $z = d$. The streamfunction associated with this temperature field is therefore given by

$$\hat{\psi}(\mathbf{k}) = -\frac{\hat{\theta}(\mathbf{k})}{|\mathbf{k}|}\mathrm{M}(|\mathbf{k}|, z, d) \tag{4.13}$$

where the function is M is defined as

$$\mathrm{M}(|\mathbf{k}|, z, d) = \frac{\cosh(|\mathbf{k}|(d-z))}{\sinh(|\mathbf{k}|d)}. \tag{4.14}$$

An alternative way to derive this inversion operator is to use the method of images from electrostatics. An infinite 'stack' of PV δ-functions spaced a distance $2d$ apart in the vertical will, when inverted with zero velocity boundary conditions at large distances, give the solution we are after in the region $0 \le z \le d$. This setup is illustrated in Figure 4.4. Summing the relevant exponentials gives the inversion as (4.13) so we do not write down the details; however, this viewpoint provides useful insight into the problem. For instance, we show below that the presence of the rigid upper boundary introduces a barotropic flavour to the dynamics. We do not have the usual picture (see Section 1.3.1) of an infinitely tall uniform potential vorticity anomaly associated with 2-d Euler dynamics, but we do have an infinitely tall 'stack' of image discs. We also note that the function M can in fact be written as

$$\mathrm{M}(|\mathbf{k}|, z, d) = e^{-|\mathrm{k}|z} + e^{-|\mathrm{k}|d}\frac{\cosh(|\mathrm{k}|z)}{\sinh(|\mathrm{k}|d)}, \tag{4.15}$$

a formulation which makes explicit the usual surface QG contribution from the original temperature patch, and the correction term from the image patches.

Returning now to consider the capped surface Rankine vortex, the full three-dimensional velocity and temperature fields can be written down by analogy to (4.10) and (4.11). In both expressions the exponential is simply replaced by the appropriate expression involving the function M:

$$U(r,z) = \theta_0 \int_0^\infty \mathrm{J}_1(\kappa)\mathrm{J}_1(\kappa r/a)\mathrm{M}\left(\kappa, \frac{z}{a}, \frac{d}{a}\right)\,\mathrm{d}\kappa \tag{4.16}$$

and

$$\Theta(r,z) = \Lambda z - \theta_0 \int_0^\infty \mathrm{J}_1(\kappa)\mathrm{J}_0(\kappa r/a)\frac{a}{\kappa}\frac{\partial \mathrm{M}}{\partial z}\left(\kappa, \frac{z}{a}, \frac{d}{a}\right)\,\mathrm{d}\kappa. \tag{4.17}$$

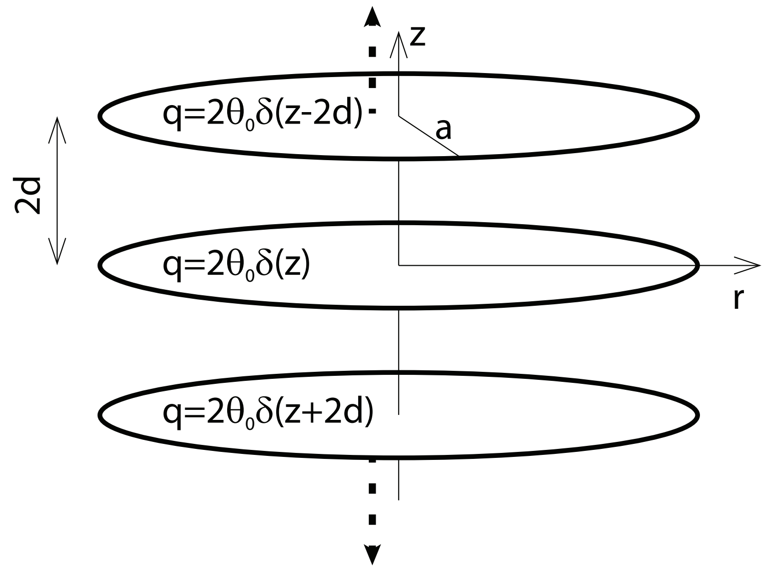

Figure 4.4 Sketch of the PV image 'stack'. There is an infinite stack of image discs separated by a distance of $2d$ in the vertical.

The upper two panels of Figure 4.6 from the next section show the difference between (4.16) and (4.10) visually. The plots show the upper tropospheric interpretation of the model. The upper panel is the standard surface QG inversion in an unbounded atmosphere (the data is the same as that used to create Figure 4.3 although only a small section is shown) whilst the second panel shows the case with a rigid isothermal lower boundary. There is clearly a stronger barotropic component to the flow when the boundary is present. The origin of this can be visualised as follows. The dashed isentrope in the upper panel has the same temperature as the entire lower surface in the second panel; if it is 'pulled' down to the surface then the resulting vortex tube stretching will induce the barotropic component of the flow observed.

We now derive the dispersion relation for perturbations to this capped surface QG Rankine vortex following the direct method of Section 2.3.2. In fact, the derivation is identical except for a factor of the function M in the integrands. The linearised perturbation radial velocity field induced by a disturbance of the surface temperature patch to the position $r = a(1+\hat{\eta}(t)e^{in\varphi})$ can be written, by inspection of (2.55), as

$$u'_r(r,\varphi,z) = \frac{in}{r}\theta_0 a\hat{\eta}(t)e^{in\varphi}\int_0^\infty \mathrm{J}_n(\kappa)\mathrm{J}_n(\kappa r/a)\mathrm{M}\left(\kappa,\frac{z}{a},\frac{d}{a}\right)\,\mathrm{d}\kappa \tag{4.18}$$

and the corresponding dispersion relation, by inspection of (2.56), as

$$\begin{aligned}\omega_n &= \frac{\theta_0 n}{a}\int_0^\infty \left(\mathrm{J}_1(\kappa)^2-\mathrm{J}_n(\kappa)^2\right)\mathrm{M}\left(\kappa,0,\frac{d}{a}\right)\,\mathrm{d}\kappa. & (4.19)\\ &= \frac{\theta_0 n}{a}\int_0^\infty \left(\mathrm{J}_1(\kappa)^2-\mathrm{J}_n(\kappa)^2\right)\coth(\kappa d/a)\,\mathrm{d}\kappa \equiv \frac{\theta_0 n}{a}\beta_n(d/a) & (4.20)\end{aligned}$$

where we have introduced the functions $\beta_n(d/a)$ which are analogous to the α_n of Chapter 2 (see (2.56)). Equation (4.20) should be compared to (2.56) which gives the surface QG result. There is a nice symmetry here: for large arguments the hyperbolic cotangent tends to one, so the surface QG result is recovered,

$$\beta_n(\infty) = \alpha_n. \tag{4.21}$$

Conversely for small argument $\coth(x) \sim 1/x$, which gives integrals of the form

$$\int_0^\infty \frac{\mathrm{J}_n(\kappa)^2}{\kappa}\,\mathrm{d}\kappa \tag{4.22}$$

which are of a standard form and evaluate as $1/2n$ (Gradshteyn & Ryzhic (2000)). Therefore the 2-d Euler result of (2.68) is recovered in the limit of small d/a with the corresponding vorticity value given by

$$q = \theta_0/d. \tag{4.23}$$

That is, the vorticity value is given by the temperature anomaly averaged over the depth of the atmosphere. This is an interesting result because it means that under this limit disturbances on the infinite stack of PV δ-function discs illustrated in Figure 4.4 behave like those on a uniform column of anomalous PV, at least for barotropic disturbances.

Figure 4.5 shows (4.20) calculated numerically for several different parameter values. These were not integrated directly because the integrands do not decay very fast. Instead, we first perform the analogous manipulation to that of (2.57)–(2.66) of Section 2.3.2. Unlike that case, however, the result is not a simple analytic formula. Instead the process results in an alternative integral which is much faster to evaluate numerically. We start by recalling the Bessel function identity of (2.60):

$$n\mathrm{J}_n^2 + \frac{1}{2}\kappa(\mathrm{J}_n^2)' = (n-1)\mathrm{J}_{n-1}^2 + \frac{1}{2}\kappa(\mathrm{J}_{n-1}^2)', \tag{4.24}$$

where as before we have suppressed the arguments of the J_n which are all just κ. Using this identity it is straight forward to derive the analogous expression to (2.61) for the present case,

$$\begin{aligned} n\beta_n(d/a) = {} & (n-1)\beta_{n-1}(d/a) \\ & - \frac{1}{2}\int_0^\infty \left[\coth(\kappa d/a) + \frac{\kappa d}{a}(1-\coth^2(\kappa d/a))\right](\mathrm{J}_n^2 + \mathrm{J}_{n-1}^2)\,\mathrm{d}\kappa \\ & + \frac{1}{2}\left[\kappa(\mathrm{J}_n^2 + \mathrm{J}_{n-1}^2)\coth(\kappa d/a)\right]_0^\infty + \int_0^\infty \mathrm{J}_1^2\coth(\kappa d/a)\,\mathrm{d}\kappa. \end{aligned} \tag{4.25}$$

Evaluating the limits using (2.63) and (2.64) and rearranging gives the result we are after:

$$\beta_n(d/a) = \beta_{n-1}(d/a) + \frac{1}{(n-1/2)}\left(\frac{1}{\pi} + \frac{d}{2a}\int_0^\infty \kappa\frac{\mathrm{J}_n^2 + \mathrm{J}_{n-1}^2}{\sinh^2(\kappa d/a)}\,\mathrm{d}\kappa\right). \tag{4.26}$$

The first term in parentheses gives the original surface QG result (2.65), and the correction term for the finite depth of the atmosphere is now easily calculated numerically because the integrand decays exponentially with κ. This has been done, and Figure 4.5 shows some results. As in Chapter 2 we have defined the phase and group speeds as

$$c_{\mathrm{p},n} = \frac{a\omega_n}{n} \quad \text{and} \quad c_{\mathrm{g},n+1/2} = a(\omega_{n+1} - \omega_n). \tag{4.27}$$

Panel (a) shows $c_{\mathrm{p},n}$ as a function of a/d for several different wavenumbers n. The plot shows that the effect of the rigid lid is to increase the phase speeds of disturbances. At small a/d, when there is little influence from the upper boundary, the phase speeds match those of the surface Rankine vortex. The dotted lines show the values of α_n to illustrate this. As a/d increases the phase speeds increase; the $n = 2$ mode phase speed is double its surface Rankine vortex value by the time $a = 1.6d$. Finally, the dashed lines show the phase speeds of the 2-d Euler Rankine vortex with vorticity values given by (4.23), that is,

$$c_{\mathrm{p},n} = \frac{\theta_0}{d} a \left(1 - \frac{1}{n}\right). \tag{4.28}$$

The phase speeds transition towards these values for $a \gg d$ as expected.

Panel (b) conversely shows the phase and group speeds as a function of wavenumber, n, for a fixed vortex with radius $a = 4d$. This represents a typical aspect ratio of the troposphere in each hemisphere as discussed above. Both the phase and group speeds increase monotonically with wavenumber. To help understand the plot we have again superimposed two additional lines. The dashed lines show, as before, the corresponding 2-d Euler result with $q = \theta_0/d$. Both the phase and group speed values match these for low wavenumbers. The dotted lines show the surface QG dispersion relation with the addition of a uniform rotation,

$$c_{\mathrm{p},n} = \theta_0\alpha_n + C \quad \text{and} \quad c_{\mathrm{g},n+1/2} = \theta_0(\alpha_{n+1} - \alpha_n) + C. \tag{4.29}$$

The uniform rotation C shifts the values vertically on the plot (so the phase speed is no longer zero at $n = 1$). It is given by the background flow induced by just the image discs which is calculated from (4.16) with the first term in (4.15) removed. The plot shows that both the phase and group speeds asymptote to these values at high wavenumbers. The wavenumber of the transition between the two regimes depends on the value of a/d but occurs around $n = 6$ for the case shown where $a = 4d$.

In summary, we have derived the dispersion relation for a simple model of large scale Rossby waves. For a shallow atmosphere (large a/d) the waves behave as

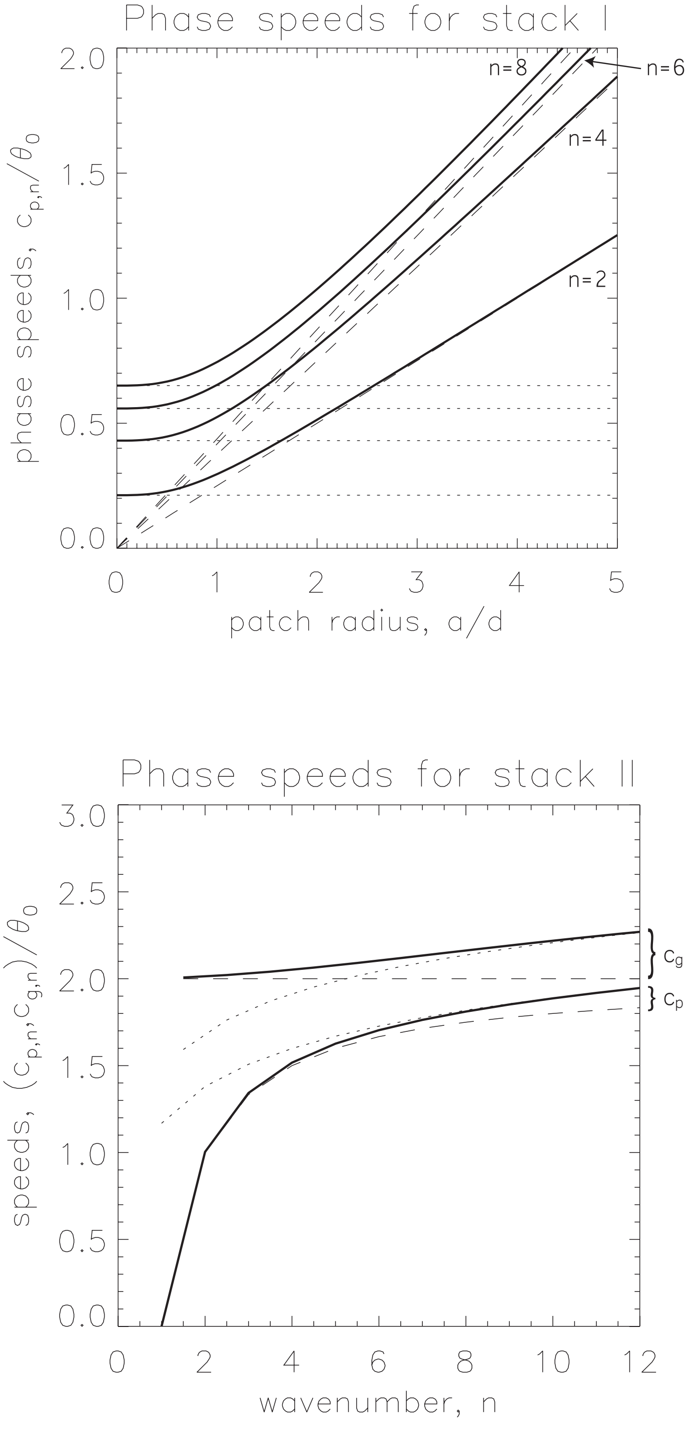

Figure 4.5 Dispersion relation for the PV stack distribution. Panel (a): phase speeds as a function of a/d for wavenumbers $n = 2, 4, 6$ and 8 as indicated. Panel (b): phase and group speeds as a function of wavenumber n with $a/d = 4$. The feint lines indicate the surface QG (dotted) and 2-d Euler (dashed) results as described in the text.

barotropic waves on a vorticity jump. For a deep atmosphere (small a/d) the waves behave like those on the surface Rankine vortex of Chapter 3 (plus a constant background rotation). Conversely for a more realistic intermediate atmosphere, there is a smooth transition between barotropic-like long waves and surface QG-like short waves.

4.4 The new model: linear theory

Having derived the dispersion relation for a single capped surface QG temperature patch we are now in a position to consider the full setup of (4.5)-(4.7). The full model is simply two such patches combined - one on the upper surface with temperature value θ_1 and radius r_1 and one on the lower surface with temperature value θ_2 and radius r_2. This works because neither patch induces a temperature anomaly at its opposing boundary thanks to the capped surface QG boundary condition that was applied.

The process of superimposing the two vortices presented here is very similar to that of Section 2.4 where we studied the surface shielded Rankine vortex. The result is a pair of coupled equations, one for the evolution of each patch edge, which we write in the form of a 2×2 matrix. The four components of the matrix represent the local propagation of each edge wave and the interactions between the waves. In this section we derive the matrix and then study the stability of the system and the form of the normal modes in detail. We also discuss the relation with the commonly used counter-propagating Rossby wave equations for this setup.

The basic state velocity and temperature fields are given by combinations of (4.16) and (4.17):

$$\begin{aligned} U(r,z) = \theta_1 \int_0^\infty \mathrm{J}_1(\kappa)\mathrm{J}_1(\kappa r/r_1)\mathrm{M}\left(\kappa, \frac{z-d}{r_1}, \frac{d}{r_1}\right) \mathrm{d}\kappa \\ + \theta_2 \int_0^\infty \mathrm{J}_1(\kappa)\mathrm{J}_1(\kappa r/r_2)\mathrm{M}\left(\kappa, \frac{z}{r_2}, \frac{d}{r_2}\right) \mathrm{d}\kappa \end{aligned} \quad (4.30)$$

and

$$\begin{aligned} \Theta(r,z) = \Lambda z - \theta_1 \int_0^\infty \mathrm{J}_1(\kappa)\mathrm{J}_0(\kappa r/r_1)\frac{r_1}{\kappa}\frac{\partial \mathrm{M}}{\partial z}\left(\kappa, \frac{z-d}{r_1}, \frac{d}{r_1}\right) \mathrm{d}\kappa \\ - \theta_2 \int_0^\infty \mathrm{J}_1(\kappa)\mathrm{J}_0(\kappa r/r_2)\frac{r_2}{\kappa}\frac{\partial \mathrm{M}}{\partial z}\left(\kappa, \frac{z}{r_2}, \frac{d}{r_2}\right) \mathrm{d}\kappa. \end{aligned} \quad (4.31)$$

These profiles are plotted in Figures 4.6 and 4.7 for two illustrative sets of parameter values. One is the completely symmetric case where

$$\theta_2 = \theta_1 \quad \text{and} \quad r_2 = r_1, \quad (4.32)$$

which is the closest this model can get to that of Juckes (1998), and the other is an unsymmetric case which is perhaps more realistic for typical atmospheric conditions

$$\theta_2 = 0.6\theta_1 \quad \text{and} \quad r_2 = 0.9 r_1. \tag{4.33}$$

These parameter values are referred to throughout this chapter as the 'symmetric' and 'realistic' cases respectively.

As with the shielded Rankine vortex, we derive an equation for the linear dynamics

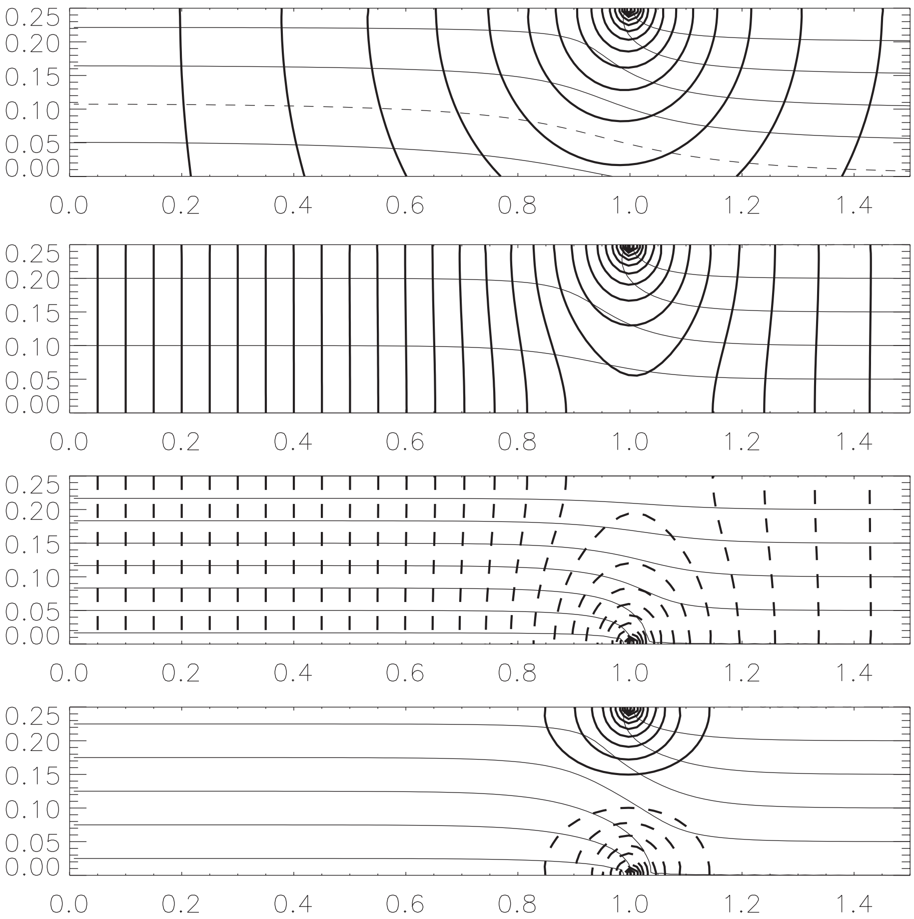

Figure 4.6 Basic state wind and potential temperature profiles for the symmetric case of (4.32). Upper three panels are a decomposition into: (a) an upper tropospheric isolated surface Rankine patch, (b) an upper tropospheric capped surface Rankine patch, and (c) a lower surface capped surface Rankine patch. Panel (d) is the full system given by the sum of (b) and (c). The heavy contours show the azimuthal velocity field with a contour interval of interval $0.1\theta_1$ (negative is dashed). The light contours show the potential temperature field with a contour interval of $0.4\theta_1$. The background potential temperature gradient is $\Lambda = 8\theta_1/r_1$.

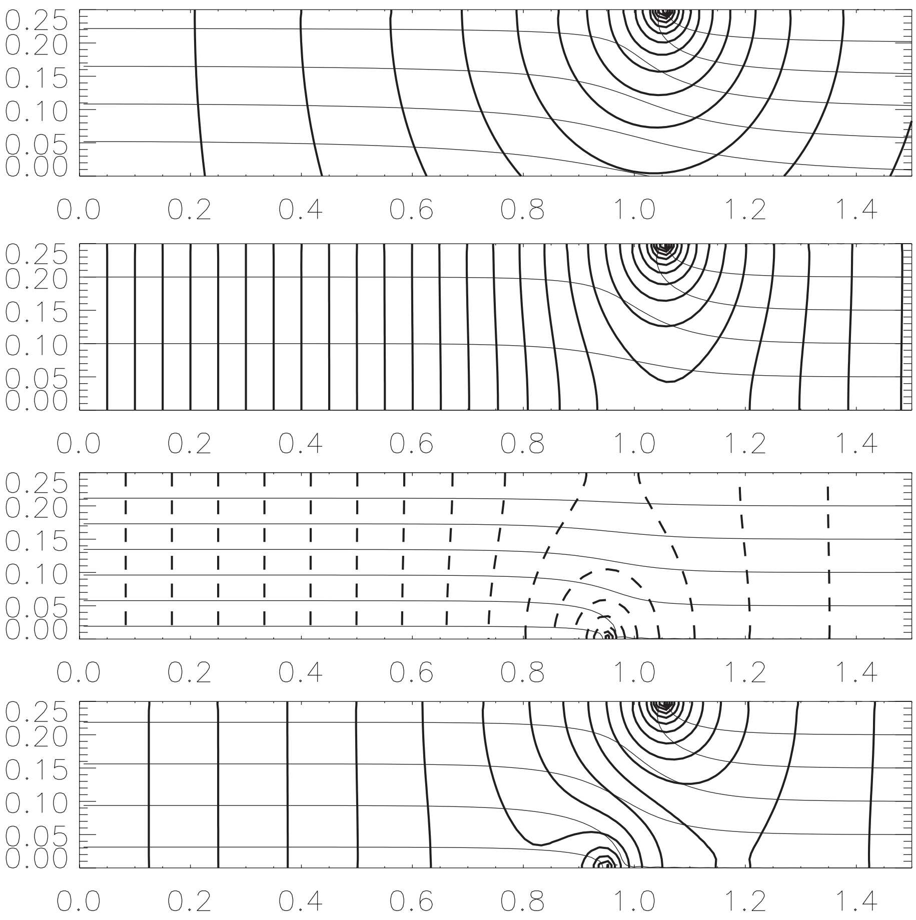

Figure 4.7 As Figure 4.6 but for the realistic case of (4.33).

by perturbing each patch boundary to the new positions

$$r = r_1 + \eta_1(\varphi, t) \quad \text{and} \quad r = r_2 + \eta_2(\varphi, t) \tag{4.34}$$

at the upper and lower surfaces respectively and considering the linearised equations for material advection of each boundary:

$$\frac{\partial \eta_1}{\partial t} = \lim_{r \to r_1} \left(u_r'(r, \varphi, d) - \frac{U(r, d)}{r_1} \frac{\partial \eta_1}{\partial \varphi} \right) \tag{4.35}$$

$$\frac{\partial \eta_2}{\partial t} = \lim_{r \to r_2} \left(u_r'(r, \varphi, 0) - \frac{U(r, 0)}{r_2} \frac{\partial \eta_2}{\partial \varphi} \right), \tag{4.36}$$

where $U(r, z)$ is given by (4.16) and the perturbation radial velocity $u_r'(r, \varphi, z)$ is likewise a linear sum of contributions from each boundary of the form (4.18). Like before we restrict attention here to a single Fourier mode, $(\eta_1, \eta_2) = (r_1 \hat{\eta}_1(t), r_2 \hat{\eta}_2(t)) e^{in\varphi}$, so that

$$u_r'(r, \varphi, z) = \frac{in}{r} e^{in\varphi} \left(\theta_1 r_1 \hat{\eta}_1(t) \int_0^\infty \mathrm{J}_n(\kappa) \mathrm{J}_n(\kappa r / r_1) \mathrm{M}\left(\kappa, \frac{d - z}{r_1}, \frac{d}{r_1} \right) \mathrm{d}\kappa \right.$$
$$\left. + \theta_2 r_2 \hat{\eta}_2(t) \int_0^\infty \mathrm{J}_n(\kappa) \mathrm{J}_n(\kappa r / r_2) \mathrm{M}\left(\kappa, \frac{z}{r_2}, \frac{d}{r_2} \right) \mathrm{d}\kappa \right), \tag{4.37}$$

and substitute for U and u'_r in (4.35) and (4.36). It is useful to define a new function

$$\mathrm{S}_n(x,y) = \int_0^\infty \frac{\mathrm{J}_n(\kappa)\mathrm{J}_n(\kappa x)}{\sinh(\kappa y)}\,\mathrm{d}\kappa. \tag{4.38}$$

which plays a similar role here to the E_n of Chapter 2. Note that $\mathrm{S}_n(1/x, y/x) = x\mathrm{S}_n(x,y)$ so the matrix equation governing the full system can be written as

$$\begin{aligned} i\frac{\mathrm{d}}{\mathrm{d}t}\begin{pmatrix}\hat{\eta}_1\\ \hat{\eta}_2\end{pmatrix} &= n\begin{pmatrix}(-\theta_1\beta_n(d/r_1)+\theta_2\mathrm{S}_1)r_2/r_1^2 & -\theta_2\mathrm{S}_n r_2^2/r_1^3\\ \theta_1\mathrm{S}_n r_1/r_2^2 & (\theta_2\beta_n(d/r_2)-\theta_1\mathrm{S}_1)/r_2\end{pmatrix}\begin{pmatrix}\hat{\eta}_1\\ \hat{\eta}_2\end{pmatrix}\\ &\equiv \boldsymbol{H}\begin{pmatrix}\hat{\eta}_1\\ \hat{\eta}_2\end{pmatrix} \end{aligned} \tag{4.39}$$

where all of the S functions are evaluated at $(r_1/r_2, d/r_2)$. This matrix governs the evolution of all linear disturbances in the system. As with the matrix of (2.85), the diagonal elements represent wave propagation on the basic state at the upper and lower patch boundaries respectively whilst the off-diagonal elements represent interactions between disturbances on opposing boundaries.

The normal mode frequencies of the system are given by the eigenvalues of $\boldsymbol{H}$ which take the form

$$\Omega_n^\pm = \frac{\mathrm{tr}(\boldsymbol{H})}{2} \pm \sqrt{\left(\frac{\mathrm{tr}(\boldsymbol{H})}{2}\right)^2 - \det(\boldsymbol{H})} \tag{4.40}$$

so there are unstable normal modes when $\mathrm{tr}(\boldsymbol{H})^2 < 4\det(\boldsymbol{H})$. Typically the solutions are a sum of both normal modes, resulting in possible transient growth at a rate as large as $|H_{12} - H_{21}|/2$ which is larger than Ω_n^+. A description of such non-modal evolution is given in Section 2.4.2, so here we focus on examining the structure of the normal modes, with the implicit understanding that they form the full range of non-modal solutions.

We first non-dimensionalise the system to reduce the dimension of the problem. There are five dimensional parameters: $\theta_1, \theta_2, r_1, r_2$ and d but we write

$$\lambda = r_2/r_1 \quad \text{and} \quad \nu = \theta_2/\theta_1 \tag{4.41}$$

to reduce this and also use

$$R = \sqrt{r_1 r_2} \quad \text{and} \quad \Sigma = (\theta_1+\theta_2)/2d \tag{4.42}$$

as length and growth rate scales respectively. The solutions to (4.39) then depend only on the initial conditions (i.e. $\hat{\eta}_1(0)$ and $\hat{\eta}_2(0)$), the wavenumber n, and the values of λ, ν and d/R as well as Σ which just scales time. Typical values of the dimensional quantities are

$$\begin{aligned} d &= 10^6\text{m} && (4.43)\\ R &= 4\times 10^6\text{m} && (4.44)\\ \Sigma &= \frac{25\text{K}\times 3\text{ms}^{-1}\text{K}^{-1}+50\text{K}\times 1.7\text{ms}^{-1}\text{K}^{-1}}{2\times 10^6\text{m}} = 8\times 10^-5\text{s}^{-1}\approx 7\text{day}^{-1}. && (4.45)\end{aligned}$$

For the rest of this chapter we set $d/R = 1/4$ to match these atmospheric values.

The CRW formulation. Before analysing the normal modes of the system we write down an alternative form of the equations. It has become common practice in baroclinic instability studies to think in terms of counter-propagating Rossby wave (CRW) components (see, for instance, Heifetz & Methven (2005)) and there is also corresponding commonly used notation.

The idea behind the CRW formulation is that any general baroclinic instability problem can be viewed as the interaction of two CRWs which are constructed from a pair of growing and decaying normal modes. The waves are untilted in both the latitude and height directions and are entirely specified by their amplitudes and phases. Each wave component propagates at its local Rossby wave speed as well as interacting with the other wave component. The linear evolution of any baroclinic instability problem can therefore be expressed in the form of a 2×2 matrix of the form (2.85) representing the propagation and interaction of the two wave components. The simplicity of the present model arises from the fact that the two CRWs are simply the perturbations on the two temperature patches, the structure and propagation properties of which have been calculated explicitly in the previous section.

The notation commonly used in CRW studies involves thinking in terms of the amplitudes and phases of each wave component by writing

$$\hat{\boldsymbol{\eta}} = \begin{pmatrix} a_1 \mathrm{e}^{\mathrm{i}\epsilon_1} \\ a_2 \mathrm{e}^{\mathrm{i}\epsilon_2} \end{pmatrix} \tag{4.46}$$

where a_i and ϵ_i are both real functions of time. On differentiating and comparing to (4.40) the following relations are obtained

$$\dot{a}_1 = H_{12}a_2\sin\epsilon, \qquad \dot{a}_2 = -H_{21}a_1\sin\epsilon \tag{4.47}$$

$$\dot{\epsilon}_1 = -H_{11} - H_{12}\frac{a_2}{a_1}\cos\epsilon, \qquad \dot{\epsilon}_2 = -H_{22} - H_{21}\frac{a_1}{a_2}\cos\epsilon, \tag{4.48}$$

where $\epsilon = \epsilon_2 - \epsilon_1$ is the relative phase of the wave components. Therefore, the off-diagonal elements of $\boldsymbol{H}$ are precisely the *interaction coefficients* of (Heifetz et al. (2004a)) and the diagonal elements are related to the *Rossby wave phase speeds*.

The main strength of this formulation is in the ease of interpretation, in particular the interpretation of non-modal evolutions. For instance, Equations (4.47) show that the amplitude of each wave component changes at a rate proportional to the other wave's amplitude multiplied by the relevant interaction coefficient. The effect is modulated by the relative phases of the two waves. If $0 < \epsilon < \pi$ then both wave amplitudes grow, if $\pi < \epsilon < 2\pi$ then both wave amplitudes decay. Equations (4.48) show that the phases of the two waves change due to two contributions: propagation at the local Rossby wave speed and an interaction effect which is again proportional to the interaction coefficients. This second effect is also modulated by the relative phases of the two waves.

In summary, the CRW evolution equations (4.47)-(4.48) provide some insight into the dynamics of this problem. However, for consistency with the rest of the thesis we now return to using the explicitly linear system (4.39).

The normal modes As a first analysis of (4.39), Figure 4.8 shows the dispersion relation (4.40) calculated for the two example sets of parameter values. The dashed lines, which are $\text{Im}(\Omega_n)$, show that both cases have growing normal modes at some wavenumbers. The symmetric case is unstable for $n = 2 - 8$ whilst the realistic case is unstable for $n = 5 - 8$. There is therefore a long-wavelength cut-off for this case. For both cases, the largest growth rate values are around 0.15Σ which is close to 1day^{-1} for the atmospheric values.

The solid lines in the figures, which are $\text{Re}(\Omega_n)$, show that the phase speeds of the growing normal modes in the symmetric case are all zero, as expected from the symmetry, whereas those of the realistic case are westward. In fact, the values of $\text{Re}(\Omega_n)$ are remarkably linear meaning that the growing normal modes propagate like perturbations on a 2-d Euler Rankine vortex. This is perhaps to be expected since the growing normal modes are, by definition, constructed from two capped surface QG waves whose influence can reach the opposing boundary and, as shown above, such waves propagate as 2-d Euler waves.

As for the shielded Rankine vortex, we now present several parameter space diagrams to illuminate some features of the instability further. Figure 4.9(a) shows the boundaries of stability in (λ, ν)-space for several wavenumbers. Clearly different regions of parameter space have instability at different wavenumbers. For instance, the wavenumber 2 region is almost entirely confined to the quadrant where both $\nu < 1$ and $\lambda > 1$, and its mirror image, meaning that there is a long-wavelength cut-off in

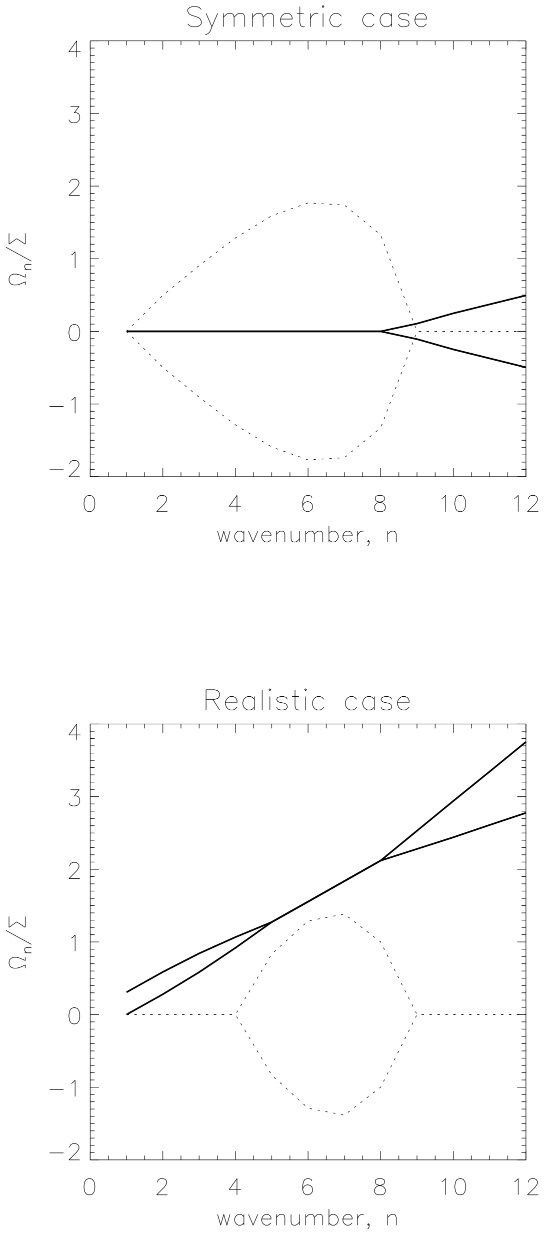

Figure 4.8 Example dispersion relations for the baroclinic instability model. Panel (a) shows the symmetric case and panel (b) is the realistic case. The solid lines show the frequencies $\mathrm{Re}(\Omega_n)$ and the dashed lines show the growth rates $\mathrm{Im}(\Omega_n) \times 10$.

this model if the weaker of the two patches is also the smaller patch. The realistic case, marked R in the diagram, is an example of this.

The next plot, Figure 4.9(b), shows the growth rate of the fastest growing normal mode at each point in parameter space. The wavenumber which achieves the fastest growth is also shown and is indicated by the shading. This plot agrees with the dispersion relation plots of Figure 4.8. One point of note is that the most unstable mode for the completely symmetric case is wavenumber $n = 6$. This will be different for different values of the aspect ratio a/R. It is also interesting that the fastest growing setups are those in which the temperature patches have almost equal radii. This is to be expected since this is the setup for which there is the strongest interaction between the two patches. There is, however, a slight bias whereby the instability is faster when the larger patch is also the weaker of the two.

Comparison to the 2-d Euler shielded Rankine vortex. Finally, we briefly note the similarity between this baroclinic setup and the completely barotropic setup of the 2-d Euler shielded Rankine vortex discussed in Section 2.4. The shielded Rankine vortex (see Figure 2.7(b))[1] is equivalent to the present system after averaging the PV distribution across the depth of the troposphere.

The plot of Figure 2.7(b) is the main comparison we make. However, the vorticity variables we used in Chapter 2 (q_0 and q_1) represented the vorticity values rather than the vorticity jumps which is what θ_0/d and θ_1/d represent here. We have therefore reproduced in Figure 4.10(a) the plot of Figure 2.7(b) but with the modified μ variable on the y-axis. There are clear similarities between this and Figure 4.9(a). One point of interest is that the confinement of the wavenumber 2 instability to just two quadrants is directly related to the absence of the wavenumber 2 instability in the upper half of Figure 2.7(b), which we noted in Chapter 2.

The major difference between the two plots, 4.9(a) and 4.10(a) is in the topology of the high wavenumber regions. The unstable regions of the baroclinic model have a clear transition between wavenumbers $n = 8$ and 9 where the region becomes disconnected, because the two wave components are less able to phase lock across the gap. The 2-d Euler case does not have this feature since for λ close to one all wavenumbers become unstable. This difference is essentially because in the baroclinic model the distance between the two wave components is always at least as large as the depth of the atmo-

---

[1] Not the shielded *surface* Rankine vortex, but rather its 2-d Euler counterpart

sphere whereas is for the shielded Rankine vortex the annulus can be infinitely narrow.

To complete the 2-d Euler comparison we present the 2-d Euler version of Figure 4.9(b) as Figure 4.10(b). The main difference again is the large wavenumber modes near $\lambda = 1$. Together these plots suggest that although the instability is baroclinic in the sense that it involves interactions between different vertical levels, there is clearly a barotropic flavour to it when the patches have different radii. Put another way, when the patches are not very close meridionally, what they 'feel' of the other's presence is dominated by the barotropic component.

4.5 The new model: numerical results

In this section we present some numerical simulations of the baroclinic instability problem studied above. We restrict attention to the two example cases (the 'symmetric' and 'realistic' cases of (4.32) and (4.33)) and only present a rather basic analysis of the simulations. A discussion is then presented which poses some questions arising from the simulations and points to directions for further work.

4.5.1 A note on the numerical code

The code used to integrate the uniform PV dynamics equations is an adapted version of the code described in Section 1.3.4. Each variable is doubled in size so as to hold information at both the surface and tropopause levels and the inversion operator is altered to give the appropriate coupling between the two fields. Here we briefly note the formulae for reference.

Denoting the surface and tropopause temperature fields as θ_s and θ_t respectively, and the corresponding streamfunction fields as ψ_s and ψ_t, we note from (4.13) and (4.14) that the appropriate inversion operator is given by

$$\hat{\psi}_s(\mathbf{k}) = -\frac{\hat{\theta}_s(\mathbf{k})}{|\mathbf{k}|}\coth(|\mathbf{k}|d) + \frac{\hat{\theta}_t(\mathbf{k})}{|\mathbf{k}|}\operatorname{csch}(|\mathbf{k}|d) \tag{4.49}$$

$$\hat{\psi}_t(\mathbf{k}) = -\frac{\hat{\theta}_s(\mathbf{k})}{|\mathbf{k}|}\operatorname{csch}(|\mathbf{k}|d) + \frac{\hat{\theta}_t(\mathbf{k})}{|\mathbf{k}|}\coth(|\mathbf{k}|d). \tag{4.50}$$

The two temperature fields add linearly, multiplied by the term $1/|\mathbf{k}|\tanh(|\mathbf{k}|d)$ for self interaction and $1/|\mathbf{k}|\sinh(|\mathbf{k}|d)$ for interaction with the opposing boundary.

The advection part of the code is unchanged from before except that now the velocity field is calculated at each boundary and each temperature field is advected separately via the semi-Lagrangian scheme.

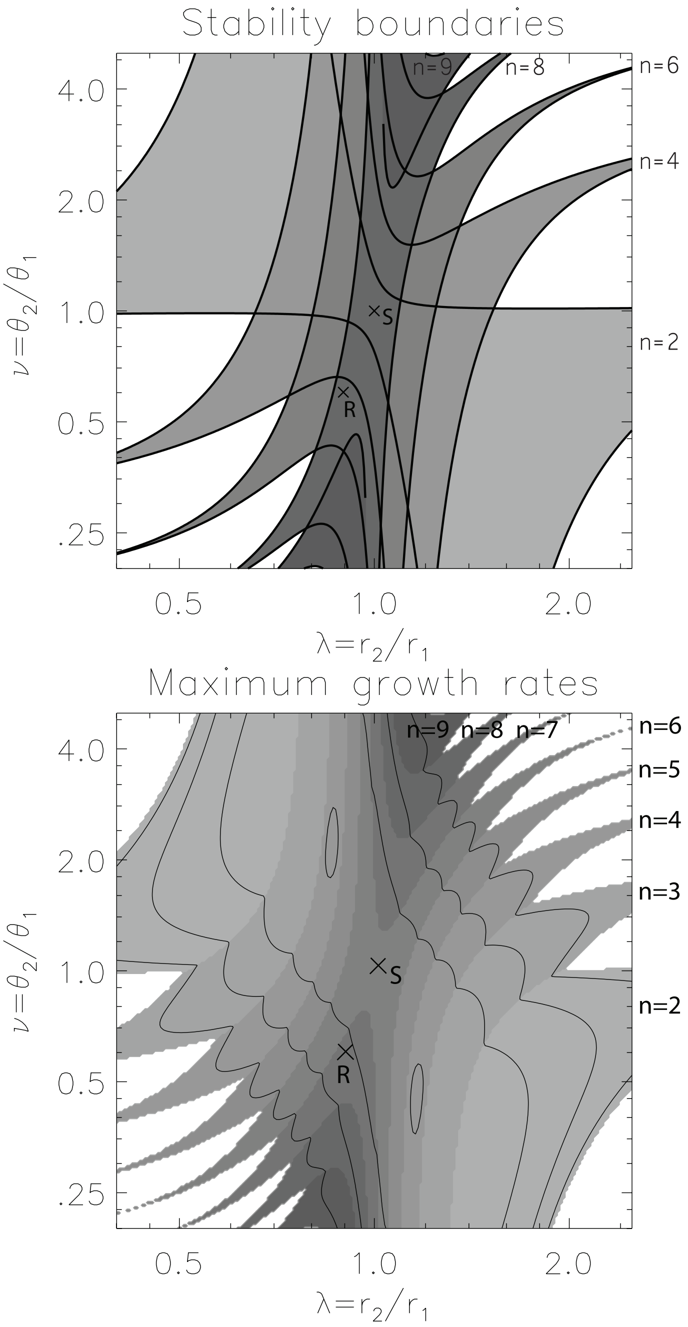

Figure 4.9 Parameter space diagram for the model of baroclinic instability. Panel (a): Stability boundaries in (λ, ν)-space for wavenumbers $n = 2, 4, 6, 8$ and 9. Panel (b): The maximum growth rates of all wavenumbers, shaded by wavenumber, with contour interval 0.05Σ. In both panels the 'S' and 'R' indicate the positions of the symmetric and realistic example cases respectively.

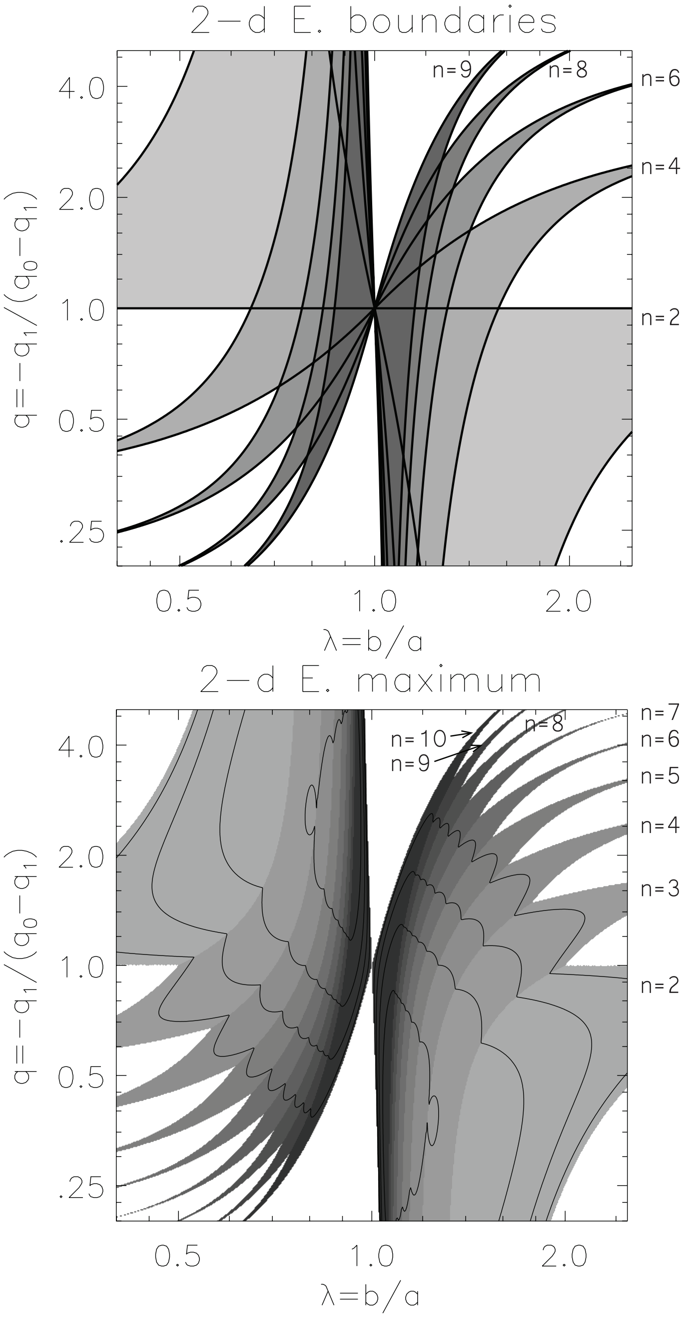

Figure 4.10 Parameter space diagrams for the 2-d Euler shielded Rankine vortex. Panel (a): Stability boundaries for wavenumbers $n = 2, 4, 6, 8$ and 9 plotted in $(\lambda, -q_1/(q_0 - q_1))$-space (see text). Panel (b): The maximum growth rates of all wavenumbers, shaded by wavenumber, with contour interval $0.05(q_0/2 - q_1)$.

Similarly to Chapter 2 the simulations presented here have initial temperature distributions which are smoothed slightly to improve the running of the code. They are specified at each boundary using formulae of the form

$$\theta_{\mathrm{t,s}}(r,\varphi) = \frac{\theta_{1,2}}{2}\left\{1 - \tanh\left[\frac{r - a(1 + \epsilon\cos(n(\varphi - \{1,2\}\pi/2))}{\delta}\right]\right\}, \tag{4.51}$$

where δ and ϵ are measures of the patch-edge temperature gradient and perturbation amplitude respectively. Note that the initial phase difference between the upper and lower level perturbations is chosen to be $\pi/2$ but other than that the upper and lower level perturbations are symmetric. In all simulations shown here the perturbation amplitudes were set as $\epsilon = 0.02$ and the initial temperature gradients fixed using $\delta = 0.001$.

4.5.2 Some example simulations

Figures 4.11 and 4.12 show plots of the numerical simulations for the symmetric and realistic cases respectively, both for the case of wavenumber 6 disturbances which, from Figure 4.8, is close to the wavenumber with the largest normal mode growth rate. The solid contours show the tropopause level temperature anomalies and the dashed contours show the surface temperature anomalies. There are two contours plotted for each level so that the amount of unintentional smoothing, caused by both the smooth initial condition and the numerical hyperviscosity-like diffusion can be seen. The times shown are dimensionless values, the scaling factor being $1/\Sigma \approx 1/7$day for typical atmospheric values, as discussed above. Therefore the panels are roughly one day apart.

Both cases show an instability develop, as expected. Both instabilities appear to develop from the intentional initial perturbation and remain close to the six-fold symmetry throughout the integrations. Considering first the symmetric case of Figure 4.11, the perturbations appear to have phase locked by the time $t = 8$ of the second panel. From Figure 4.8(a) (and symmetry), we expect the phase speed of the phase-locked system to be zero, and the disturbance does indeed grow without rotation throughout panels 3, 4 and 5. The nonlinear behaviour of this particular setup is peculiar. Since the surface and the tropopause level anomalies are equal, neither dominates the evolution and the result is that each wave peak, or what would meteorologically be called a ‘trough’, continually protrudes away from the ‘pole’ in a symmetric fashion. By the final panel it appears that six coherent dipolar structures have formed and these continue to propagate outwards. The dipolar structures are interesting in that they are split across the two levels. The positive PV component is at the tropopause whilst the negative PV component is at the surface. Finally, we note that what remains of the temperature patches appears to be stable, at least to the wavenumber 6 disturbance. Presumably this is because the remaining patches are much smaller than the initial setup so will have different stability characteristics. Effectively the value of d/R has increased so that, for instance, the plot of the stability boundaries in Figure 4.9(a) will change and the wavenumber 6 unstable region will no longer cover the symmetric case.

The realistic case of Figure 4.12 is very different because the upper-level–lower-level symmetry is broken. The temperature anomaly of the upper patch is stronger than that of the lower patch and the upper patch is also slightly larger than the lower patch. Again the disturbances appear to phase lock, this time with a net positive phase speed, as predicted by Figure 4.8(b). The growing disturbances therefore rotate clockwise in Figure 4.12. As before the troughs protrude away from the pole as the disturbance grows, but this time they tilt to the right, i.e. the wave breaks anti-cyclonically. As is typical for anti-cyclonic wave breaking events, the upper level trough is stretched-out into a filamentary structure. We note here that since only a small amount material is in the filament the upper level patch is not much smaller than its original size. The lower patch does however appear to be smaller than its initial size. This suggests that here the stabilisation has occurred primarily by moving location in the parameter space of Figure 4.9(a) rather than changing the stability boundaries themselves.

We present two further diagnostics of the evolutions. The first is the angular momentum of the system (see (1.34)). Figures 4.14(a) and (b) each show the total angular momentum, as well as its split between the upper and lower temperature anomalies for each simulation. The total angular momentum should be conserved and so the slight increase during the realistic simulation is a measure of the effects of the numerical diffusion. The two separate components are not constrained to be fixed, and do indeed show large variations. Since the total angular momentum is simply the sum of the two components it makes some sense to think of the instability as acting to transfer angular momentum form the lower patch to the upper patch. However, this might be slightly misleading since the magnitude of both are forced to increase as the variance of the temperature distributions increase (see (4.4)).

The next plots, Figures 4.15(a) and (b), show the zonal mean temperature profiles at the beginning and end of each simulation. This is to illustrate the comments made above regarding the poleward migration of the fronts. In the symmetric simulation both fronts move poleward, whereas in the realistic simulation the lower front moves further than the upper front.

Finally, Figure 4.13 shows the evolution of the instability for the realistic set of parameter values, but this time the initial perturbation is not chosen to deliberately favour wavenumber six. Instead the frontal perturbations consist of randomly selected amplitudes and relative phase values for each of the first ten wavenumbers. The development in this case is not so clean as the earlier cases. This is because, as Figure 4.8(b) shows, The two fastest growing normal modes have very similar growth rates for this set of parameter values with wavenumber six only slightly smaller than wavenumber seven. The nonlinear breaking, however, is of a similar nature to the cleaner case of Figure 4.12 whereby the upper level filaments break anticyclonically.

4.6 Discussion

To summarise this chapter, we have described and analysed a new simple analytic model of baroclinic instability. The model represents the hemispheric-scale interactions between an upper-level mid-latitude jet and a surface front. It is an extension of the model described by Juckes (1998), the main difference being that it is set in circular geometry which has the major advantage of permitting a wider range of basic states to be considered. In particular, the strong upper-level–lower-level symmetry present in both the standard Eady model and that of Juckes can be broken.

The linear analysis follows one the main themes of the thesis: the study of waves on surface QG temperature fronts. It most closely follows the work of Section 2.4 in that the system comprises two such waves which interact to form the instability. The analysis includes the derivation of the dispersion relation for perturbations to the ‘capped surface Rankine vortex’ which is effectively a new dispersion relation for Rossby waves on a mid-latitude jet stream. The full problem comprises two such vortices, one at the surface and one at tropopause level, which interact to form the instability. The nonlinear simulations presented show that the instability is vaguely realistic, in terms of growth rate and spatial pattern, for sensible atmospheric parameters.

The analysis of the numerical simulations presented here was however rather brief, and it leaves many interesting questions. For instance, how does the wave breaking behaviour vary around parameter space? Or, put another way, is the nonlinear wave breaking behaviour a simple function of the basic state parameters? In particular the results could be compared in detail with some of the previous models of wave break-

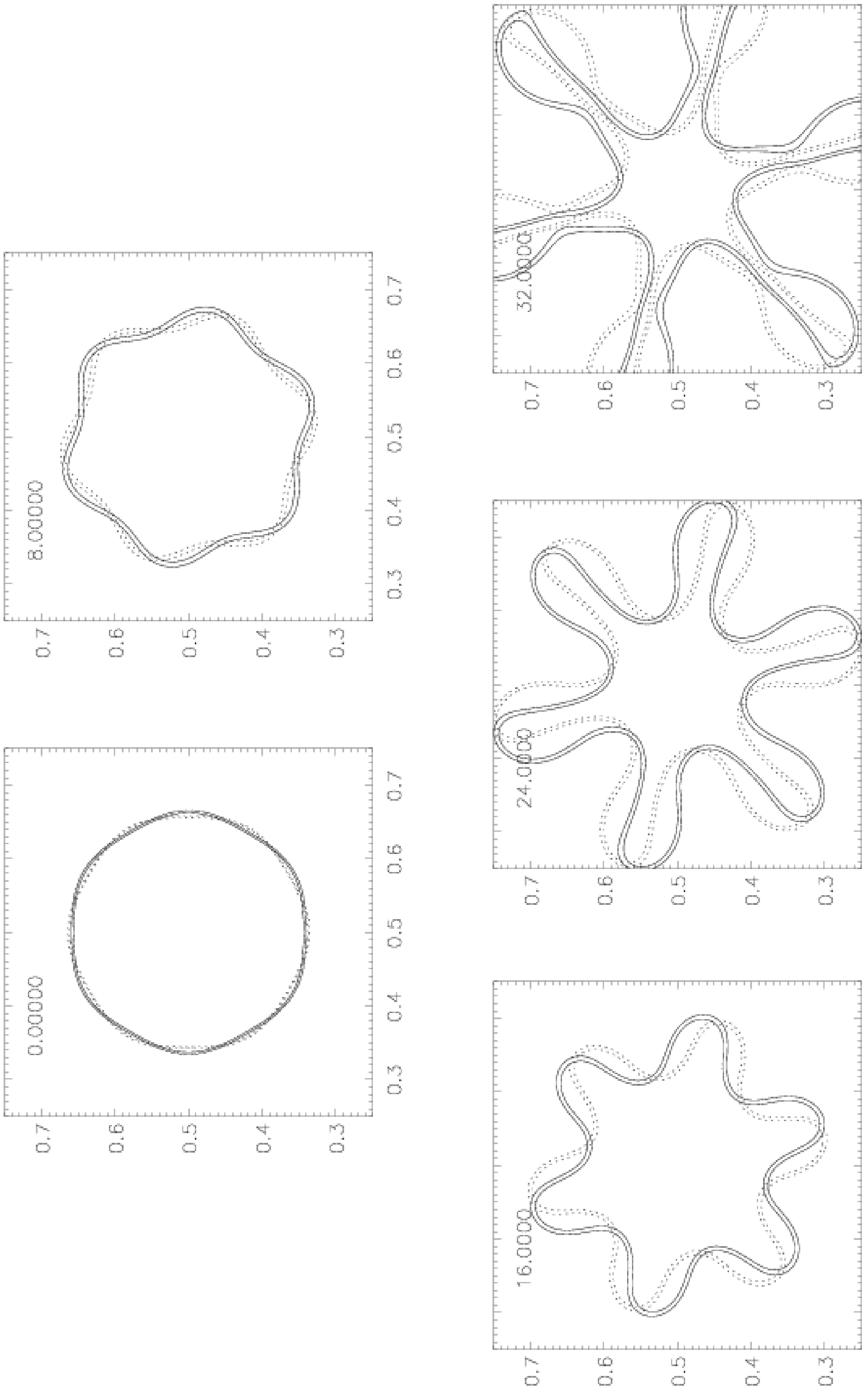

Figure 4.11 Baroclinic instability numerical simulation, symmetric case. Each panel shows the temperature distributions at height $z = d$ (solid contours) and at the surface (dashed contours) at the times indicated on the plots.

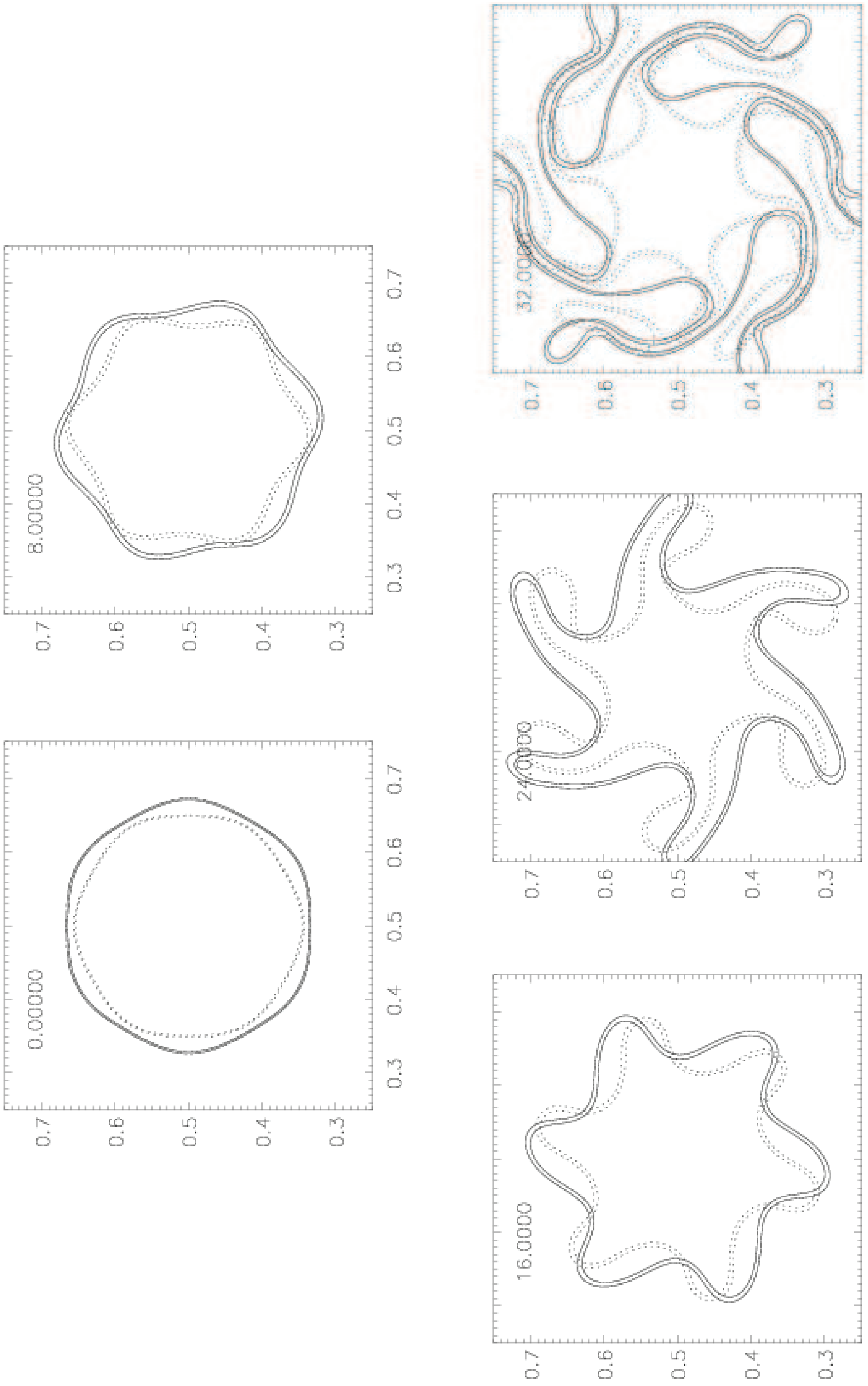

Figure 4.12 Baroclinic instability numerical simulation, realistic case. Each panel shows the temperature distributions at height $z = d$ (solid contours) and at the surface (dashed contours) at the times indicated on the plots.

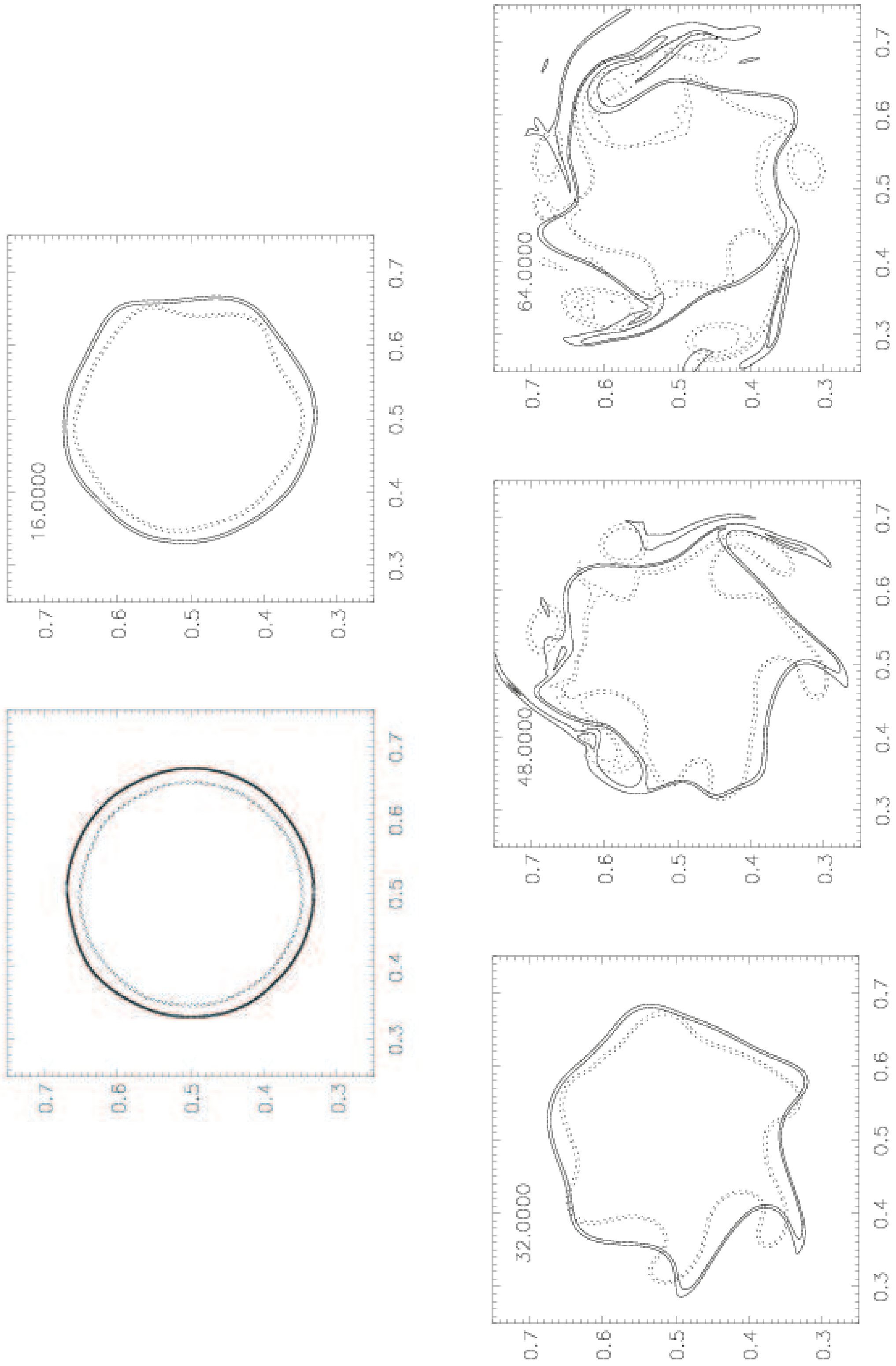

Figure 4.13 Baroclinic instability numerical simulation, realistic case with a random initial perturbation. Each panel shows the temperature distributions at height $z = d$ (solid contours) and at the surface (dashed contours) at the times indicated on the plots.

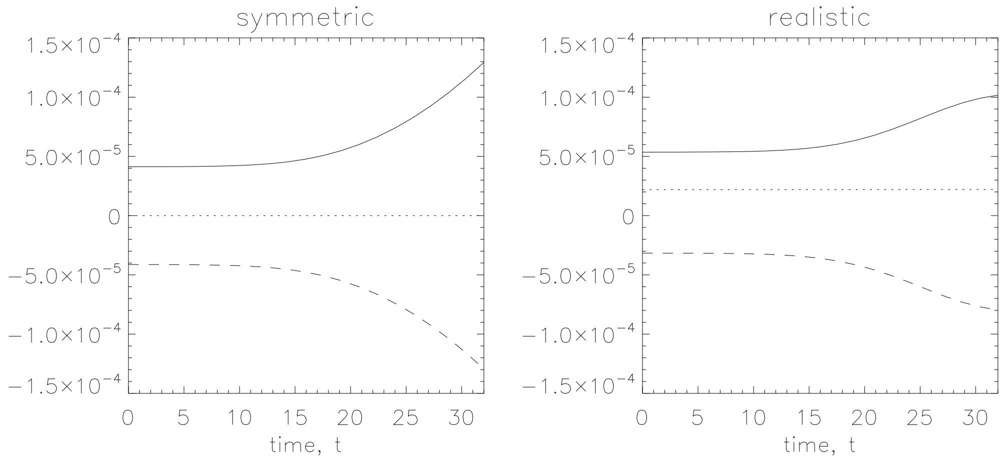

Figure 4.14 Angular momentum time series. The left panel shows the symmetric simulation, the right panel is the realistic simulation. In both panels the dotted line shows the total angular momentum, the solid line shows the angular momentum induced by the upper patch and the dashed line shows that induced by the lower patch.

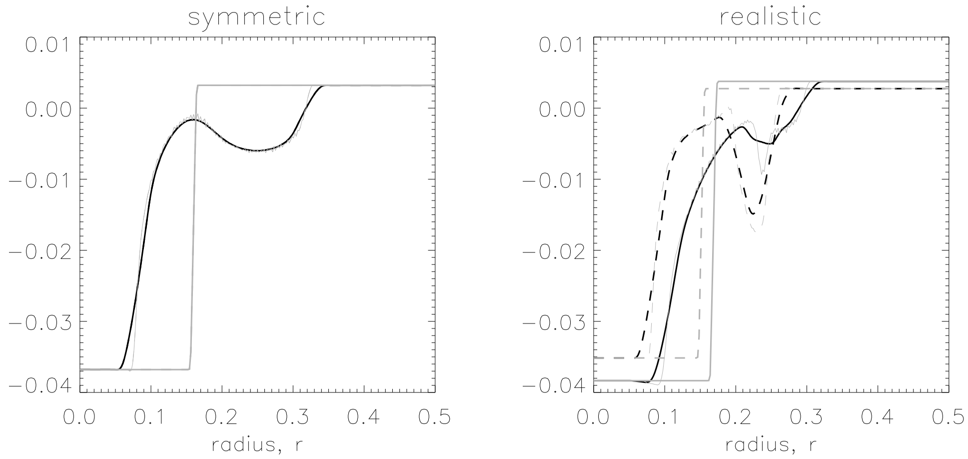

Figure 4.15 Final state zonal mean temperature profiles. The left panel shows the symmetric simulation, the right panel is the realistic simulation. In both panels the solid lines are upper level values and the dashed lines are lower level values. There are two curves shown for each: the thick grey lines are the initial values and thick black lines are the final values. The final values are in fact a smoothed version of the data; a running mean has been used to remove some of the small scale structure. The mean is taken over approximately $1/12^{\text{th}}$ of the domain shown. The original data is shown by the faint lines.

ing, in particular Simmons & Hoskins (1978) and Thorncroft et al. (1993) who look at baroclinic wave breaking in more realistic atmosphere models and Polvani & Dritschel (1993) who investigate the influence of spherical geometry on the breaking of barotropic Rossby waves. The symmetric case shown here breaks symmetrically, with no preference between anti-cyclonic versus cyclonic turning of the temperature contours. Although we have stated that this is perhaps not the most realistic choice of parameters, there are sometimes instances in the real atmosphere whereby quasi-stationary Rossby waves grow meridionally to very large amplitude without obviously tilting in one direction or the other, and this is a manifestation of this behaviour in our model. The realistic case shown above clearly breaks anti-cyclonically due to the ambient shear in the basic state outside of the patches. This shear is clear in Figure 4.7 and is a result of there being a net positive PV anomaly when integrated over both patches. Therefore the far-field azimuthal velocity field is positive, but decays barotropically with distance from the patch centres (i.e. like $1/r$), giving an anti-cyclonic shear. In essence, filaments which protrude too far equatorward get 'left behind' by the mean flow at the patch edges.

It is easy to calculate the far field behaviour from the basic state parameters. From (4.30) the basic state velocity field satisfies

$$U(r) \sim \frac{1}{r}\left(\frac{\theta_1}{d}r_1^2 - \frac{\theta_2}{d}r_2^2\right) \tag{4.52}$$

and is positive or negative, meaning the ambient shear is anti-cyclonic or cyclonic, when the non-dimensional combination $\lambda^2\nu$ is greater than or smaller than 1. Preliminary experiments suggest that this does indeed predict the direction of wave breaking in this model. However, the cyclonic breaking produced when $\lambda^2\nu > 1$ is perhaps not always realistic. An example of this is given by the 'realistic' setup chosen above in reverse. Due to the symmetry of the system, if the temperature values and the radii values are swapped between the upper and lower surfaces then evolution would simply be the mirror image of that we obtained. The breaking would be cyclonic, but based on a net easterly jet which is dominated by the surface component.

The second question concerns the basic state chosen for the problem. The basic state used here was chosen primarily for its mathematical tractability. An interesting setup, which is not tractable mathematically, would be to take different temperature profiles and study their stability properties numerically. For instance, an interesting lower boundary condition would be to choose the lower boundary temperature distribution which makes the basic state velocity field zero everywhere on the lower boundary, whilst still keeping the patch profile at the upper boundary.

Finally, we mentioned above that the final states of the simulations appear to be stable and that this is achieved through different mechanisms. In the symmetric case of Figure 4.11 both patches appear to lose sufficient material that the resultant vortex is smaller than the initial setup, thereby effectively increasing the value of d/R (recall that this parameter has been set to $1/4$ throughout this chapter) and presumably changing the topology of the stability curves in Figure 4.9(a). The realistic case, however, whilst also losing material to the filaments, stays much nearer to its original size. The stability arises due to changing the relative sizes of the patches, thereby moving position on the stability diagram. This difference in behaviour may well be related to the type of wave breaking exhibited by the model. For instance, does anti-cyclonic breaking always lead to the lower-level patch losing more material to filaments than the upper layer? It would be insightful to perform detailed experiments over all of parameter space to illuminate these features further. These results could then be compared to wave breaking in the real atmosphere to see which features of the model are robust in observations.

Chapter 5:

THESIS SUMMARY AND FUTURE WORK

In this thesis we have examined several topics related to linear wave dynamics in the surface QG system, in particular the dynamics of frontal waves. Each topic answers one of the four key scientific questions set out in the introduction, and they all contribute to the first question about the qualitative differences between the surface QG and 2-d Euler models.

A derivation of arguably the most basic linear frontal wave solution, that of waves on a circular patch of uniform temperature, is presented. This solution is analogous to the 2-d Euler Rankine vortex dispersion relation. Surface QG frontal waves are peculiar since they exist on a basic state with a singular velocity profile. The dispersion relation is also logarithmically singular meaning that infinitely short waves propagate infinitely quickly, such that wave their phase speeds (advection plus propagation) are finite.

The theory used to derive the dispersion relation is then extended to study more complicated vortices; for the first time, an analytic study of the stability of surface QG vortices is presented. In particular, the case of a vortex formed by two temperature patches summed together is studied. The results are consistent with the numerical study of Carton (2009) and are compared in detail to the 2-d Euler study of Flierl (1988). One interesting conclusion regarding the stability of surface QG vortices is that in the presence of an external straining field of strength s a vortex of temperature θ_0 and radius a will deform by a factor proportional to as/θ_0. This means that smaller vortices are less affected by straining than larger vortices.

The stability of temperature filaments in the surface QG system is also investigated.

This builds on the earlier work of Juckes (1995) who studied the stability of an isolated 'top-hat' filament, considering the application of the instability upper tropospheric shear lines often observed in satellite images. The addition of external shearing and straining presented here changes the stability properties remarkably. Straining in particular can speed up the instability process. This is in contrast to the 2-d Euler system for which it is well known that straining has a stabilising effect. In contrast to that case, surface QG filaments which are formed by a large scale straining do not have to leave the region of straining before they become unstable.

Furthermore, we have shown that the instability is unusual in that it is not always the initial perturbations which grow large first. Perturbations applied after the start of an initial value problem can potentially cause the filaments to roll-up faster than any initial perturbations which are present. This situation arises here because the basic state evolves in time. Finally, we noted that the vortices which form out of the instability have radii inversely proportional to strain rate, making the observation of the previous paragraph that small vortices are less vulnerable to deformation than larger vortices, consistent with the possibility of a statistically steady scale-independent state.

In Chapter 4 we moved away from pure surface QG dynamics and instead consider a simple baroclinically unstable setup in the uniform PV model of Blumen (1978). The model consists of two temperature patches, one at the surface and one at the rigid upper lid. The setup is baroclinically unstable to disturbances to the two temperature fronts. The study therefore provides another example of wave propagation of temperature fronts as well as some insightful comparisons between the surface QG and 2-d Euler models. It also provides an alternative problem to the well-known Eady model which highlights some of the short comings of that model. Numerical simulations of the instability are also presented. These show the instability occurring as expected and also pose questions about the nature of the nonlinear wave breaking that the model exhibits.

It was noted in the Introduction chapter that the turbulence spectra of energy and enstrophy are different between the surface QG and 2-d Euler systems and that this is due to the qualitatively different evolutions between the models. The curdling of filaments studied in Chapter 3 is the most obvious candidate for this difference. Recent work by Dritschel et al. (2008) has considered 2-d Euler turbulence in terms of the statistics of vortices of different scales. It seems likely that a similar framework could be applied to the surface QG system, particularly since vortices appear to be much more prevalent in the system at small scales. The scaling argument presented in Chapter 3 whereby the size of vortices is dependent on the magnitude of the strain in which they are formed would contribute to such an investigation.

Further to this it would be of interest, given the recent studies of Lapeyre & Klein (2006) and Klein et al. (2008) which apply the surface QG framework to the dynamics of the upper layers of the ocean, to look at the behaviour of near surface vortices in an ocean model and compare their characteristics with those predicted for the surface QG system. The presence of the curdling at small scales in particular will have impacts on the transport of heat, salt and other advected quantities.

The final chapter leaves another avenue for future work and that is to perform a more thorough analysis of the nonlinear wave breaking behaviour of the baroclinic instability model. We have presented the nonlinear evolution for two different sets of parameter values. It would be straightforward to run simulations over the entire parameter space of Figure 4.9. Aspects of the wave breaking, for instance the direction of the breaking and the amount of material lost from the patches could then be examined and quantified systematically.

We conclude by noting that this thesis has illuminated the conceptual relevance of the surface QG model to many geophysical problems. It is arguably just as conceptually relevant to many geophysical situations as the more well-studied 2-d Euler system, albeit with a slightly more mathematically challenging structure. However, many of the well-studied 2-d Euler calculations can be performed in the surface QG setup and doing this has provided an intriguing insight into the dynamics of the real atmosphere which has aspects that can be modelled at times as either model, or else something between the two.

Appendix A:

THE NUMERICAL MODEL: DETAILS AND TESTS

A.1 Introduction

The numerical scheme developed for this project runs on a doubly periodic domain. The inversion of the temperature field to obtain the velocity field is performed in spectral space, this part of the scheme is tested below in Section A.2. The time-stepping procedure is a semi-Lagrangian scheme with 2^{nd} order trajectory integrations and a 3^{rd} order interpolation scheme. The time-stepping procedure is tested in Section A.3.

A semi-Lagrangian scheme was chosen because it is computationally cheap thanks to its favourable stability constraints. Unlike many finite difference schemes the criterion for numerical stability is independent of the grid size. Instead, numerical stability only requires a small enough time step such that grid-point trajectories do not cross. This condition can be expressed succinctly at leading order in terms of the velocity field gradient, a type of Lipschitz number, and is used in the code to implement an adaptive time step. A general disadvantage of semi-Lagrangian schemes is the numerical hyper diffusion inherent in the necessary interpolation process. A novel attempt is made in Section A.4 to quantify the effects of this.

As a final test of the scheme, Section A.5 examines how accurately the model conserves several conserved quantities of the surface QG equations.

A.2 Testing the inversion scheme

The inversion scheme has been tested with several temperature distributions for which simple analytic solutions are possible. Three cases are presented here. The analytic solutions for the three cases are derived from the following results:

$$\theta = \sin y \quad \text{induces} \quad u = \cos y \tag{A.1}$$

$$\theta = \mathrm{J}_0(r/a) \quad \text{induces} \quad u = \mathrm{J}_1(r/a) \tag{A.2}$$

$$\theta = \begin{cases} 1 & |y| < L \\ 0 & |y| > L \end{cases} \quad \text{induces} \quad u = -\frac{1}{\pi} \log \left| \frac{y-L}{y+L} \right| \tag{A.3}$$

where y in cases (1) and (3) is a Cartesian coordinate and r in case (2) is the radial coordinate. The J_i in case (2) are the regular Bessel functions of the first kind. All of these inversions were carried out on a grid with resolution 512 in each direction.

Case (1). For this simple test case the maximum absolute error between the numerical result and the analytic result was smaller than the accuracy of the output data, which has 5 decimal places. This is to be expected because the inversion is trivial in spectral space and the profile is well resolved here.

Cases (2). The case of Bessel functions was tested because they have different symmetry properties to the square numerical grid (and case (1)). This case cannot be made periodic so the numerical output cannot be compared quantatively to the analytic solution, but Figure A.1 shows that the solution is qualitatively correct.

Case (3). Finally we test the inversion of a temperature profile with large gradients. It is well known that Fourier decompositions do not converge well near discontinuities: piecewise continuous functions have Fourier coefficients which decay like $(\text{wavenumber})^{-1}$, but we do not investigate this here. We assume that a temperature feature with steep gradients is represented sufficiently accurately provided the large gradient region is resolved by several grid points. We test our inverter is performing as we expect by comparing the output of a slightly smoothed version of (A.3) as shown in Figure A.2 to that of a 1-dimensional Hilbert transform code. The Hilbert transform code is also spectral and so has the same convergence properties as the inversion scheme for the surface QG code. Figure A.2 shows that the two agree well for this case.

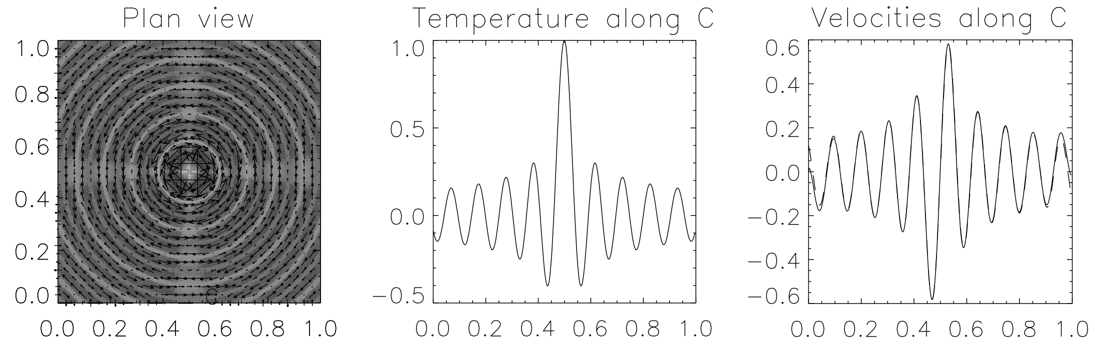

Figure A.1 Inverter test, case (2). The left hand panel shows the temperature field (shading) and the corresponding velocity field (arrows) throughout the domain. The other two panels show cross sections of temperature (centre) and velocity (right) along the line C. The right hand panel also shows the analytic solution for an unbounded domain (dashed line) - see text.

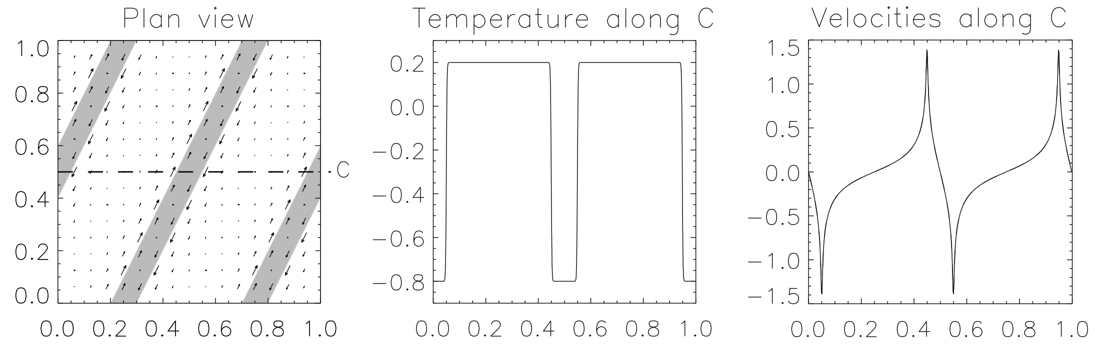

Figure A.2 Inverter test, case (3). The left hand panel shows the temperature field (shading) and the corresponding velocity field (arrows) throughout the domain. The other two panels show cross sections of temperature (centre) and velocity (right) along the line C. The right hand panel also shows the numerical Hilbert transform solution (dashed), but the two lines are indistinguishable.

A.3 Testing the advection scheme

The back-trajectory calculation in the semi-Lagrangian scheme uses a midpoint scheme to estimate the change of velocity along trajectories. Given the velocity fields from the current and previous timesteps, $\mathbf{u}_i$ and $\mathbf{u}_{i-1}$, an estimate of the velocity field at time $i + 1/2$ is calculated as

$$\mathbf{u}^* = \frac{3}{2}\mathbf{u}_i - \mathbf{u}_{i-1}. \tag{A.4}$$

Then, for each gridpoint $\mathbf{x}_0$ an estimate of the midpoint of the trajectory that lands on $\mathbf{x}_0$ at time $i + 1$ is given by

$$\mathbf{x}_{\text{mid}} = \mathbf{x}_0 - \mathbf{u}^*(\mathbf{x}_0)\frac{\Delta t}{2} \tag{A.5}$$

where Δt is the timestep. The step (A.5) is then iterated twice more, but each time cubic interpolation is used to estimate the value of $\mathbf{u}^*$ at the latest version of $\mathbf{x}_{\text{mid}}$ rather than $\mathbf{x}_0$. Finally, the source of the trajectory is estimated by iterating once more, this time without the factor of $1/2$ in the final term. This is similar to methods described by Durran (1999) and is second order in time. To test this we prescribed a solid-body rotation velocity field and set the initial θ distribution to be a small localised patch with a Gaussian profile displaced from the origin. The advection scheme was run through one rotation period with several different time step values and the resulting errors compared. The error in the advection was quantified by taking a cross section through the initial and final distributions and measuring the 'peak error', defined as the distance between the peaks of the profiles (the profiles were first smoothed by fitting a quadratic polynomial to the central three gridpoints). The results in Figure A.3 suggest the scheme is close to second order accurate for this experiment.

A.4 Quantifying the numerical diffusion

The numerical scheme uses cubic interpolation (in two dimensions) as part of the time-stepping process. This generates spurious hyper diffusion-like behaviour which is dependent on the spatial and temporal resolution that is used. Mariotti et al. (1994) argue that the effects of such diffusive behaviour can be significant in some situations, at least in the 2-d Euler case. Here an attempt to quantify the effect of the hyper diffusion is presented (see also Durran (1999)).

Consider the simplest interpolation scheme: one dimensional linear interpolation. The semi-Lagrangian scheme works by estimating the back-trajectory from each grid

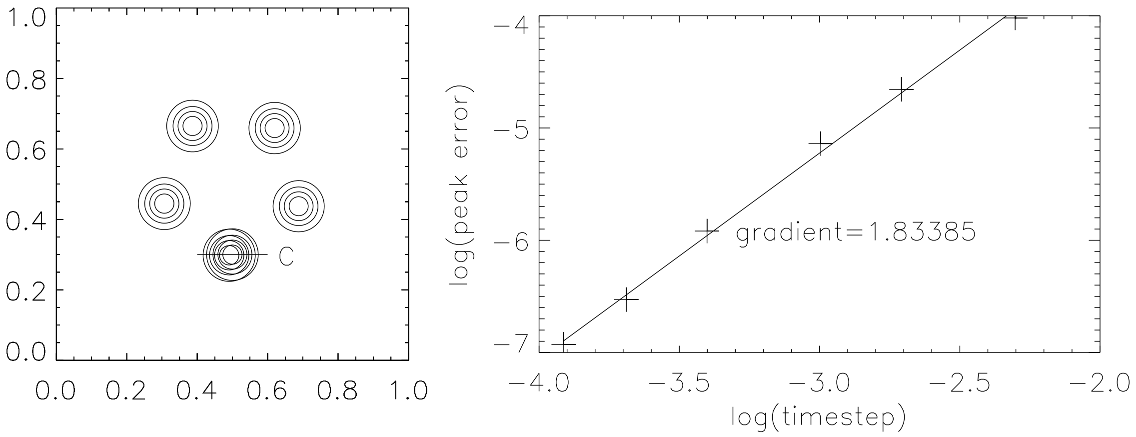

Figure A.3 Time-stepping test. Left panel shows a superposition of the temperature profile at several times during one run. The patch moves anticlockwise and returns to near its initial position. The error (as defined in text) between the initial and final profiles is plotted in the right panel.

point and then estimating the value of θ at the start of the trajectories by interpolation. To estimate the error in this interpolation process, suppose that a function $y(x)$ is known at time $t = t_0$ only at some gridpoints $(..., x_{-1}, x_0, x_1, ...)$ where it takes the values $(..., y_{-1}, y_0, y_1, ...)$ (see Figure A.4). Now suppose a back-trajectory ends at $a \equiv x_0 + \delta$ and suppose the velocity is nearly constant so the back-trajectory from the previous grid point ends at $b \equiv x_{-1} + \delta$. Estimating $y(a)$ and $y(b)$ by linear interpolation gives the values taken to the next step. However, the value of y associated with the point x_0 will no longer be the same after the advection. Under linear interpolation this value is instead given by $Y_0 = y_0 + \delta(1-\delta)(y_{-1} - 2y_0 + y_1)$: to leading order the error is proportional to the second derivative of y. If there are many time steps with random back-trajectories then the average value of the proportionality constant will be appropriate and to first order in time the evolution is given by (using $\overline{\delta(1-\delta)} = 1/6N^2$)

$$\frac{\partial y}{\partial t} = \frac{1}{6N^2 \Delta t} \frac{\partial^2 y}{\partial x^2}. \tag{A.6}$$

This is clearly only an approximation to the reality, but it shows explicitly the diffusive nature of linear interpolation.

The above calculation can be extended to cubic interpolation and also higher dimensions. For example, one dimensional cubic interpolation results in a generalised form of hyper diffusion

$$\frac{\partial y}{\partial t} = \frac{11}{360\Delta t} \left(-\frac{1}{N^4} \frac{\partial^4 y}{\partial x^4} + \frac{31}{464} \frac{1}{N^6} \frac{\partial^6 y}{\partial x^6} \right). \tag{A.7}$$

Although the two terms on the right hand side are formally of the same order, the first

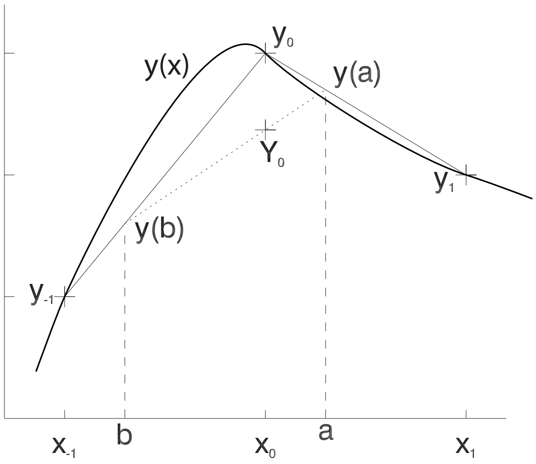

Figure A.4 Diagram to illustrate the effect of interpolation.

term generally dominates the behaviour due to the small coefficient of the second term. The corresponding result for two dimensions is more complicated again, but it is similarly dominated by a term of the form $-\nabla^4 y/N^4$. As could be expected, some of the small terms ignored in the 2-d case are not isotropic, there are terms like $\partial^4/\partial x^2 \partial y^2$, but their effect is unlikely to be important.

To test how well this theory applies to the real numerical errors involved in interpolation, consider the simple model

$$\frac{\partial \theta}{\partial t} = -\nu \frac{\partial^4 \theta}{\partial x^4}, \tag{A.8}$$

where ν can be taken to give the first term in (A.7), with the initial condition a step function

$$\theta(t=0) = \begin{cases} 1 & x > 0 \\ 0 & x < 0. \end{cases} \tag{A.9}$$

An analytic solution can be obtained via a similarity variable $s \equiv x/(4\nu t)^{1/4}$:

$$\theta(x,t) = \Theta(s) \equiv \frac{1}{2} + \frac{1}{\pi} \int_0^\infty \frac{\sin ks}{k} e^{-k^4/4} dk \tag{A.10}$$

(an example of this profile is the dashed curve of Figure A.6). The gradient of θ at $x = 0$ can be calculated from this solution, giving

$$\left. \frac{\partial \theta}{\partial x} \right|_{x=0} = \frac{\Gamma(1/4)}{4\pi} \frac{1}{(\nu t)^{1/4}}, \tag{A.11}$$

where $\Gamma(1/4) \approx 3.626$. Here we test this formula against the numerical scheme.

A square 'top-hat' patch of anomalous θ was advected around the domain with a constant velocity until it returned to its starting position where its profile was compared to its initial profile. As the velocity field was prescribed there were no errors due to the advection or inversion parts of the scheme. Figure A.5 shows some results. Plotted are cross sections of part of the domain at various times where the θ patch should have returned to its initial position. According to the simple model, the gradient of the cross section in θ at its steepest point should be proportional to $t^{-1/4}$ and it can be seen that this agrees well with the numerics. Further, an estimate for ν can be obtained by comparing two consecutive cross sections. This was done and found to be 6.0×10^{-10}, a value which agrees well with the theoretical value of 7.1×10^{-10} predicted from (A.7) at this resolution.

Further weight is given to the form of (A.7) by Figure A.6 which plots one of the cross sections in Figure A.5 with the similarity solution of (A.10) at a time such that the maxima are aligned. The theoretical result is in good agreement with the numerics.

Finally we consider the effect of using an adaptive time step. As discussed in the introduction to this appendix, semi-Lagrangian schemes are stable provided the calculated back-trajectories do not cross and this condition is met at leading order provided the velocity gradients are not too large compared to Δt^{-1}. That is,

$$|\nabla \mathbf{u}|\, \Delta t < C, \qquad \text{(A.12)}$$

where C is some constant which we choose typically to be 0.3. Here the matrix norm is calculated as

$$|\boldsymbol{A}| \quad = \max_{|\mathbf{x}|\neq 0} \frac{|\boldsymbol{A}\mathbf{x}|}{|\mathbf{x}|} \quad = \sqrt{\text{largest e.value of } \boldsymbol{A}^*\boldsymbol{A}} \qquad \text{(A.13)}$$

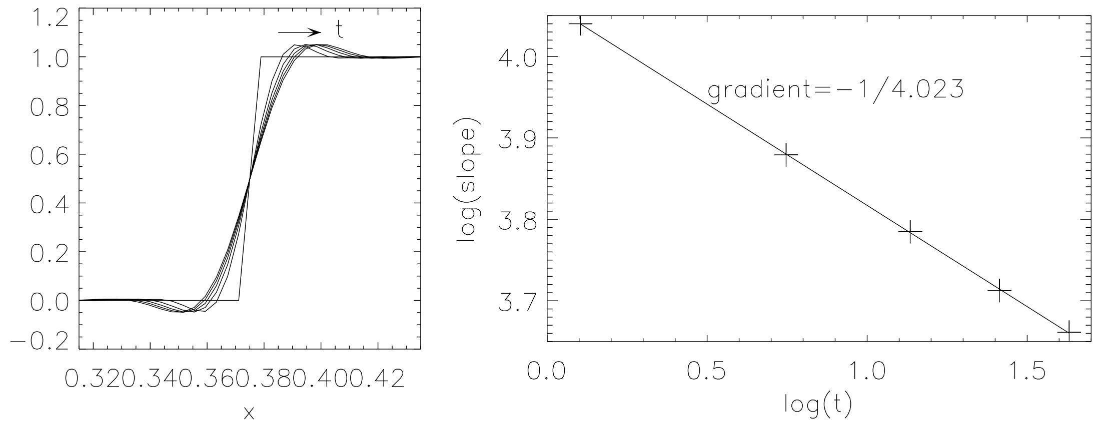

Figure A.5 Examining effects of interpolation. The left hand panel is a superposition of cross sections at a temperature jump as time proceeds. The right hand panel shows the slope of the profiles at their steepest point.

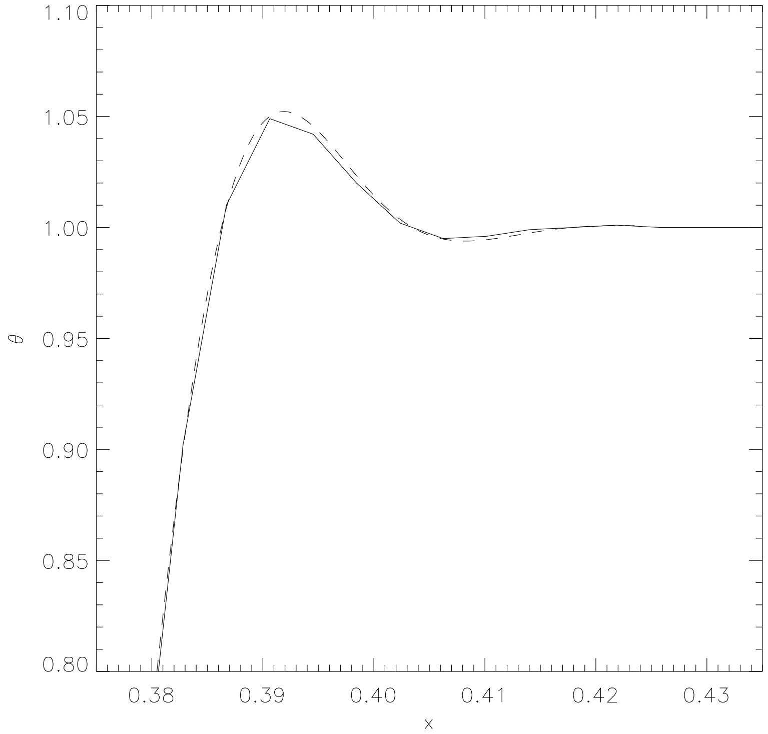

Figure A.6 The solid curve is one curve from the left hand panel in Figure A.5. The dashed curve is (A.10) with s chosen such that the maxima of the two curves are aligned.

where * represents the conjugate transpose. In the numerical code the condition (A.12) is checked every second time step and the length of the time step is either unaltered, halved or doubled accordingly.

If a simulation is well-developed in the sense that enstrophy has cascaded to the grid scale then typically

$$\nabla \mathbf{u} \sim \frac{\max \theta}{\Delta x} \sim N \max \theta \tag{A.14}$$

meaning that the time step chosen satisfies $\Delta t \propto C/N$. Therefore the diffusion coefficient estimated in (A.7) will in fact behave as N^{-3} rather than N^{-4} when there is grid-scale activity.

A.5 Conservation properties of the scheme

The surface QG equations conserve both the total energy, E, and the surface temperature variance, Z, which are defined in the Introduction chapter. Figure A.7 shows the evolution of these quantities for the turbulence simulation of Figure 1.3 in the Introduction.

The total energy is conserved remarkably well by this relatively long simulation. The enstrophy is only conserved well up to about $t = 0.3$ which, by looking at the plots of Figure 1.3, is when temperature variations reach the grid scale and also filament instability begins to occur. This breakdown of conservation is expected since as disucssed in the Introduction the joint constraints of energy and enstrophy conservation force the dominant enstrophy contributions to move downscale, whilst the dominant energy contribution does not change wavenumber.

This turbulence simulation was run at resolution $n = 2048$ which is a higher resolution than all of the other runs in this thesis. To test the conservation properties in a more relevant setting we present in Figure A.8 a smooth slowly evolving situation run at resolution $n = 512$. Both E and Z are conserved to within 0.2% over this time period. Another quantity of the surface QG equations is the maximum and minimum values of the temperature field. These are also presented in the figures and can be seen to remain constant to a good degree of accuracy.

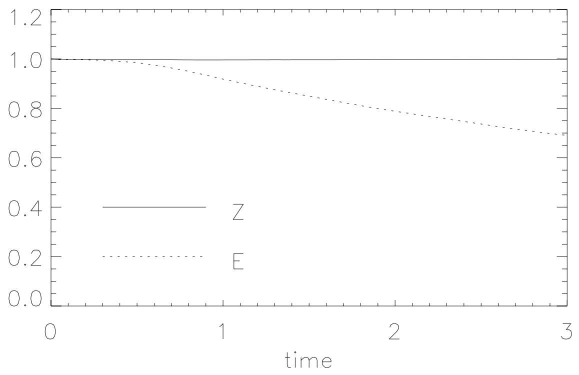

Figure A.7 Evolution of the total energy E and enstrophy Z for the freely decaying turbulence simulation of Figure 1.3. Both quantities have been normalised here by their initial values.

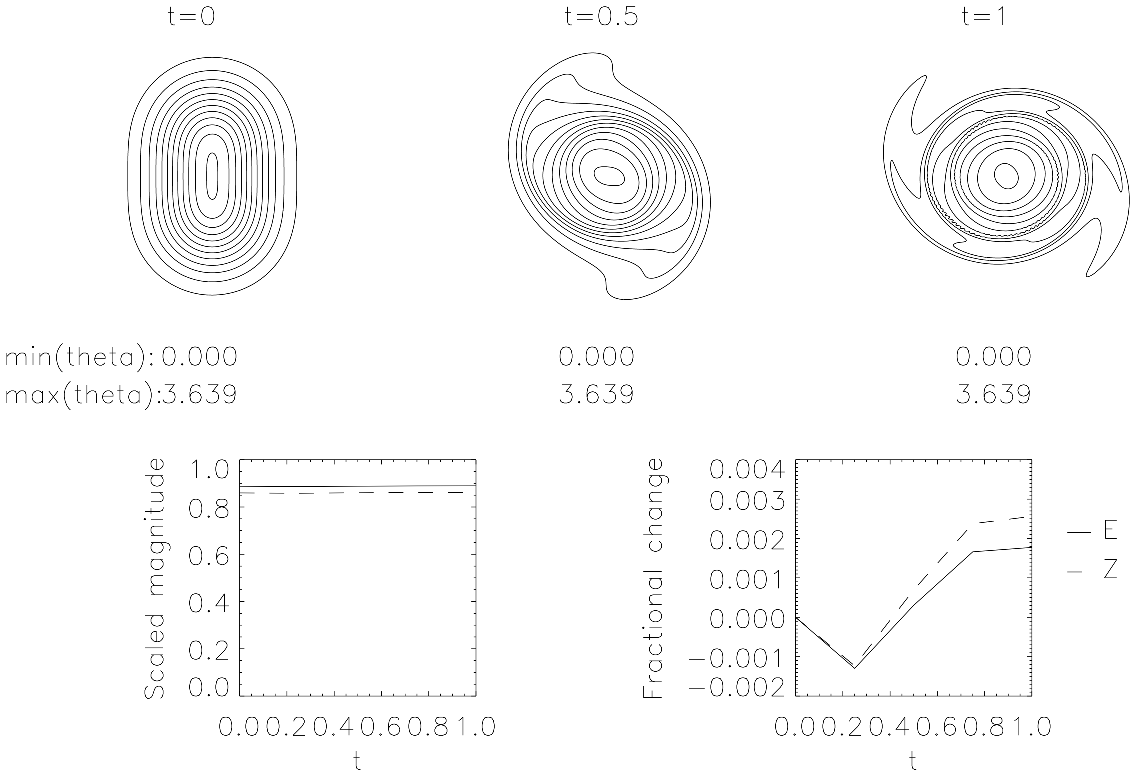

Figure A.8 Conservation properties test. Top panel shows evolution of temperature field and the values of the extrema in the θ field. Lower panels show the evolution of E and Z. The values of E here have been scaled by a factor of 10 for ease of comparison.

Appendix B:

ASYMPTOTICS OF THE FUNCTIONS E_n

Here we derive the two asymptotic results for the function E_1 which are referred to in Section 2.3, equations (2.38) and (2.39).

B.1 Small $|r/a - 1|$

The calculation of the dispersion relation in Section 2.3 shows that the leading order term of the singularity at $r = a$ is the same for each of the E_n. Here we show that E_0 is actually a complete elliptic integral of the first kind for which there are well known asymptotic results and then the result for E_1 follows. To do this we use the following integral definition of the Bessel functions which is suitable when n is an integer:

$$\mathrm{J}_n(\kappa) = \frac{1}{2\pi} \int_{-\pi}^{\pi} \mathrm{e}^{\mathrm{i}(\kappa \sin\theta - n\theta)}\, d\theta. \tag{B.1}$$

Substituting for J_0 in (2.36) gives

$$\mathrm{E}_0(\rho) = \frac{1}{4\pi^2} \int_{-\pi}^{\pi} \int_{-\pi}^{\pi} \int_0^{\infty} \mathrm{e}^{\mathrm{i}\kappa(\sin\theta + \rho\sin\phi)}\, d\kappa\, d\theta\, d\phi \tag{B.2}$$

where we have put $\rho = r/a$. Upon use of the identity

$$\int_0^{\infty} \mathrm{e}^{\mathrm{i}\kappa f(x)}\, d\kappa = \pi \sum_{\{x_i : f(x_i) = 0\}} \frac{\delta(x - x_i)}{|f'(x_i)|}, \tag{B.3}$$

the integral (B.2) can be written as

$$\mathrm{E}_0(\rho) = \frac{2}{\pi} \int_0^{\pi/2} \frac{d\phi}{(1 - \rho^2 \sin^2\phi)^{1/2}}. \tag{B.4}$$

This is a standard definition of the complete elliptic integral of the first kind. It therefore follows from a standard result (Gradshteyn & Ryzhic (2000)) that

$$\mathrm{E}_0(\rho) \approx \frac{2}{\pi}\left(-\frac{1}{2}\log|1-\rho^2| + 2\log 2\right) \tag{B.5}$$

near $\rho = 1$, and so, by rearranging (2.56) to find

$$\lim_{\rho\to 1}(\mathrm{E}_1(\rho) - \mathrm{E}_0(\rho)) = -\frac{2}{\pi}, \tag{B.6}$$

we arrive at

$$\mathrm{E}_1(\rho) \approx \frac{1}{\pi}(-\log|1-\rho^2| + 4\log 2 - 2). \tag{B.7}$$

B.2 Large r/a

The $n = 1$ version of (B.2) is

$$\mathrm{E}_1(\rho) = \frac{1}{4\pi^2}\int_{-\pi}^{\pi}\int_{-\pi}^{\pi}\int_0^{\infty} \mathrm{e}^{\mathrm{i}\kappa(\sin\theta+\rho\sin\phi)}\mathrm{e}^{-\mathrm{i}(\theta+\phi)}\,d\kappa\,d\theta\,d\phi. \tag{B.8}$$

With the aim of using (B.3) again, note that for large ρ the zeros of the first exponential occur at $\phi \approx -\rho^{-1}\sin\theta$ and $\phi \approx \pm\pi + \rho^{-1}\sin\theta$. On substituting into (B.8) and rearranging we arrive at

$$\mathrm{E}_1(\rho) \approx \frac{1}{2\pi}\int_{-\pi}^{\pi} \frac{\sin\theta\sin\left(\frac{\sin\theta}{\rho}\right)}{\rho|\cos\left(\frac{\sin\theta}{\rho}\right)|}\,d\theta \tag{B.9}$$

$$\approx \frac{1}{2\pi\rho^2}\int_{-\pi}^{\pi}\sin^2\theta\,d\theta \tag{B.10}$$

$$= \frac{1}{2\rho^2}. \tag{B.11}$$

Similarly it can be shown that $\mathrm{E}_n(\rho) \propto \rho^{-(n+1)}$ for large ρ.

REFERENCES

Ambaum, M. H. P. 2010 *Thermal Physics of the Atmosphere.* Wiley and Sons.

Ambaum, M. H. P. & Athanasiadis, P. J. 2007 The Response of a Uniform Horizontal Temperature Gradient to Heating. *J. Atmos. Sci.* **64**, pp. 3708–3716.

Ambaum, M. H. P. & Verkley, W. T. M. 1995 Orography in a contour dynamics model of large-scale atmospheric flow. *J. Atmos. Sci.* **52**, pp. 2643–2662.

Bishop, C. H. & Thorpe, A. J. 1994 Frontal Wave Stability during Moist Deformation Frontogenesis. Part I: Linear Wave Dynamics. *J. Atmos. Sci.* **51**, pp. 852–873.

Blumen, W. 1978 Uniform Potential Vorticity Flow: Part I. Theory of Wave Interactions and Two-Dimensional Turbulence. *J. Atmos. Sci.* **35**, pp. 774–783.

Bretherton, F. P. 1966a Baroclinic instability and the short wave cut-off in terms of potential vorticity. *Quart. J. Roy. Meteor. Soc.* **92**, pp. 335–345.

Bretherton, F. P. 1966b Critical layer instability in baroclinic flows. *Quart. J. Roy. Meteor. Soc.* **92**, pp. 325–334.

Capet, X., Klein, P., Hua, B. L., Lapeyre, G. & McWilliams, J. C. 2008 Surface kinetic energy transfer in surface quasi-geostrophic flows. *J. Fluid Mech.* **604**, pp. 165–174.

Carton, X. 2009 Instability of Surface Quasigeostrophic Vortices. *J. Atmos. Sci.* **66**, pp. 1051–1062.

Carton, X., Flierl, G. R., Perrot, X., Meunier, T. & Sokolovskiy, M. A. 2010 Explosive instability of geostrophic vortices. Part 1: baroclinic instability. *Theor. Comput. Fluid Dyn.* **24**, pp. 125–130.

Charney, J. G. 1947 The dynamics of long waves in a baroclinic westerly current. *Journal of Meteorology* **4**, pp. 136–162.

Charney, J. G. 1948 On the scale of atmospheric motions. *Geofys. Publ. Oslo* **17**, pp. 1–17.

Charney, J. G. 1971 Geostrophic Turbulence. *J. Atmos. Sci.* **28**, pp. 1087–1095.

Constantin, P., Nie, Q. & Sch ”orghofer, N. 1998 Nonsingular surface quasi-geostrophic flow. *Physics Letters A* **241**, pp. 168–172.

Dacre, H. F. & Gray, S. L. 2006 Life-cycle simulations of shallow frontal waves and the impact of deformation strain. *Quart. J. Roy. Meteor. Soc.* **132**, pp. 2171–2190.

Davies, H. C. & Bishop, C. H. 1994 Eady Edge Waves and Rapid Development. *J. Atmos. Sci.* **51**, pp. 1930–1946.

Deem, G. S. & Zabusky, N. J. 1978 Vortex waves: stationary "V-states", interactions, recurrance and breaking. *Phys. Rev. Lett.* **40**, pp. 859–862.

Dritschel, D. G. 1988a Contour surgery: a topological reconnection scheme for extended integrations using contour dynamics. *J. Comput. Phys.* **77**, pp. 240–266.

Dritschel, D. G. 1988b Nonlinear stability bounds for inviscid, two-dimensional, parralel or circular flows with monotonic vorticity, and the analogous three-dimensional quasi-geostrophic flows. *J. Fluid Mech.* **191**, pp. 575–581.

Dritschel, D. G. 1989 On the stabilization of a two-dimensional vortex strip by adverse shear. *J. Fluid Mech.* **206**, pp. 193–221.

Dritschel, D. G. 2011 An exact steadily rotating surface quasi-geostrophic elliptical vortex. *Geo. and Astr. Fluid Dyn.* **105**, pp. 368–376.

Dritschel, D. G., Haynes, P. H., Juckes, M. N. & Shepherd, T. G. 1991 The stability of two-dimensional vorticity filament under uniform strain. *J. Fluid Mech.* **230**, pp. 647–665.

Dritschel, D. G., Scott, C., R. K. Macaskill, Gottwald, G. A. & Tran, C. V. 2008 Unifying Scaling Theory for Vortex Dynamics in Two-Dimensional Turbulence. *Phys. Rev. Lett.* **101**.

Durran, D. R. 1999 *Numerical Methods for Wave Equations in Geophysical Fluid Dynamics*. Springer.

Eady, E. T. 1949 Long waves and cyclone waves. *Tellus* **1**, pp. 33–52.

Farrell, B. F. & Ioannou, P. J. 1996 Generalised Stability Theory. Part I: Autonomous Operators. *J. Atmos. Sci.* **53**, pp. 2025–2040.

Flierl, G. R. 1988 On the instability of geostrophic vortices. *J. Fluid Mech.* **197**, pp. 349–388.

Gradshteyn, I. S. & Ryzhic, I. M. 2000 *Table of Integrals, Series and Products*. Jeffrey, A. and Zwillinger, D. (eds), AP, 6th edition.

Harvey, B. J. & Ambaum, M. H. P. 2010 Instability of surface temperature filaments in strain and shear. *Quart. J. Roy. Meteor. Soc.* **136**, pp. 1506–1513.

Harvey, B. J. & Ambaum, M. H. P. 2011 Perturbed Rankine vortices in surface quasi-geostrophic dynamics. *Geophys. & Astro. Fluid Dyn.* **105**, pp. 377–391.

Harvey, B. J., Ambaum, M. H. P. & Carton, X. J. 2011 Instability of shielded surface temperature vortices. *J. Atmos. Sci.* **68**, pp. 964–971.

Heifetz, E., Bishop, C. H., Hoskins, B. J. & Methven, J. 2004a The counter-propagating Rossby-wave perspective on baroclinic instability. I: Mathematical basis. *Quart. J. Roy. Meteor. Soc.* **130**, pp. 211–231.

Heifetz, E. & Methven, J. 2005 Relating optimal growth to counterpropagating Rossby waves in shear instability. *Phys. Fluids* **17**.

Heifetz, E., Methven, J., Hoskins, B. J. & Bishop, C. H. 2004b The counter-propagating Rossby-wave perspective on baroclinic instability. II: Application to the Charney model. *Quart. J. Roy. Meteor. Soc.* **130**, pp. 233–258.

Held, I. M., Pierrehumbert, R. T., Garner, S. T. & Swanson, K. L. 1995 Surface quasi-geostrophic dynamics. *J. Fluid Mech.* **282**, pp. 1–20.

Holton, J. 2004 *An introduction to dynamic meteorology*. Academic press.

Hoskins, B. J. 1982 The mathemtical theory of frontogenesis. *Ann. Rev. Fluid Mech.* **14**, pp. 131–151.

Hoskins, B. J., McIntyre, M. E. & Robertson, A. W. 1985 On the use and significance of isentropic potential vorticity maps. *Quart. J. Roy. Meteor. Soc.* **111**, pp. 877–946.

Joly, A. & Thorpe, A. J. 1990 Frontal instability generated by tropospheric potential vorticity anomalies. *Quart. J. Roy. Meteor. Soc.* **116**, pp. 525–560.

Juckes, M. 1994 Quasigeostrophic dynamics of the tropopause. *J. Atmos. Sci.* **51**, pp. 2756–2768.

Juckes, M. 1995 Instability of Surface and Upper-Tropospheric Shear Lines. *J. Atmos. Sci.* **52**, pp. 3247–3262.

Juckes, M. 1998 Baroclinic instability of semi-geostrophic fronts with uniform potential vorticity. I: An analytic solution. *Quart. J. Roy. Meteor. Soc.* **124**, pp. 2227–2257.

Juckes, M. 1999 The structure of idealised upper-tropospheric shear lines. *J. Atmos. Sci.* **56**, pp. 2830–2845.

Juckes, M. & McIntyre, M. E. 1987 A high-resolution one-layer model of breaking planetary waves in the stratosphere. *Nature* **328**, pp. 590–596.

Kevlahan, N. K.-R. & Farge, M. 1997 Vorticity filaments in two-dimensional turbulence: creation, stability and effect. *J. Fluid Mech.* **346**, pp. 49–76.

Klein, P., Hua, B. L., Lapeyre, L., Capet, X., Le Gentil, S. & Sasaki, H. 2008 Upper Ocean Turbulence from High-Resolution 3D Simulations. *J. Phys. Ocean.* **38**, pp. 1748–1763.

Lamb, H. 1932 *Hydrodynamics*. Cambridge University Press, 6th edition.

Lapeyre, G. & Klein, P. 2006 Dynamics of the upper oceanic layers in terms of surface quasigeostrophy theory. *J. Phys. Ocean.* **36**, pp. 165–176.

Legras, B. & Dritschel, D. 1993 Vortex stripping and the generation of high vorticity gradients in two-dimensional flows. *Appl. Sci. Res.* **51**, pp. 445–455.

Majda, A. J. & Tabak, E. G. 1996 A two-dimensional model for quasigeostrophic flow: comparison with the two-dimensional Euler flow. *Physica D* **98**, pp. 515–522.

Mariotti, A., Legras, B. & Dritschel, D. 1994 Vortex stripping and the erosion of coherent structures in two-dimensional flows. *Phys. Fluids* **6**, pp. 3954–3962.

Meacham, S. P. 1992 Quasigeostrophic, ellipsoidal vortices in a stratified fluid. *Dyn. Atmos. Oceans* **16**, pp. 189–223.

Methven, J., Heifetz, E., Hoskins, B. & Bishop, C. 2005a The counter-propagating Rossby-wave perspective on baroclinic instability. Part III: Primitive-equation disturbances on the sphere. *Quart. J. Roy. Meteor. Soc.* **131**, pp. 1393–1424.

Methven, J., Hoskins, B., Heifetz, E. & Bishop, C. 2005b The counter-propagating Rossby-wave perspective on baroclinic instability. Part IV: Nonlinear life cycles. *Quart. J. Roy. Meteor. Soc.* **131**, pp. 1425–1440.

Nastrom, G. D. & Gage, K. S. 1985 A Climatology of Atmospheric Wavenumber Spectra of Wind and Temperature observed by Commercial Aircraft. *J. Atmos. Sci.* **42**, pp. 950–960.

Pedlosky, J. 1987 *Geophysical fluid dynamics*. Springer.

Pierrehumbert, R. T., Held, I. M. & Swanson, K. L. 1994 Spectra of Local and Nonlocal Two-dimensional Turbulence. *Chaos, Solitons and Fractals* **4**, pp. 1111–1116.

Polvani, L. M. & Dritschel, D. G. 1993 Wave and vortex dynamics on the surface of a sphere. *J. Fluid Mech.* **255**, pp. 35–64.

Pullin, D. I. 1992 Contour dynamics methods. *Ann. Rev. Fluid Mech.* **24**, pp. 89–115.

Rayleigh, L. 1880 On the stability or instability of certain fluid motions. *Proc. Lond. Maths. Soc.* **11**, pp. 57–70.

Rodrigo, J. L. 2005 On the evolution of sharp fronts for the quasi-geostrophic equation. *Comm. Pure Appl. Math* **58**, pp. 821–866.

Saffman, P. G. 1995 *Vortex Dynamics*. CUP.

Scott, R. K. & Dritschel, D. G. 2005 Quasi-geostrophic vortices in compressible atmospheres. *J. Fluid Mech.* **530**, pp. 305–325.

Shepherd, T. G. 2003 Hamiltonian Dynamics. In Holton, J. R., editor, *Encyclopedia of the Atmospheric Sciences*. AP, 2nd edition, pp. 929–938.

Simmons, A. J. & Hoskins, B. J. 1978 The Life Cycles of Some Nonlinear Baroclinic Waves. *J. Atmos. Sci.* **35**, pp. 414–432.

Smy, L. A. & Scott, R. K. 2009 The influence of stratospheric potential vorticity on baroclinic instability. *Quart. J. Roy. Meteor. Soc.* **135**, pp. 1673–1683.

Thorncroft, C. D., Hoskins, B. J. & McIntyre, M. E. 1993 Two paradigms of baroclinic-wave life-cycle behaviour. *Quart. J. Roy. Meteor. Soc.* **119**, pp. 17–55.

Tulloch, R. & Smith, K. S. 2006 A Theory for the atmospheric energy spectrum: Depth-limited temperature anomalies at the tropopause. *Proc. Natl. Acad. Sci. USA* **103**, pp.

690–694.

Vallis, G. K. 2006 *Atmospheric and Oceanic Fluid Dynamics*. Cambridge University Press.

Verkley, W. T. M. 1994 Tropopause dynamics and planetary waves. *J. Atmos. Sci.* **51**, pp. 509–529.

Williams, R. T. & Plotkin, J. 1968 Quasi-Geostrophic Frontogenesis. *J. Atmos. Sci.* **25**, pp. 201–206.

Zabusky, N. J., Hughes, M. H. & Roberts, K. V. 1979 Contour dynamics of the Euler equations in two dimensions. *J. Comput. Phys.* **30**, pp. 96–106.

Zhmur, V. V. & Shchepetkin, A. F. 1991 Evolution of an ellipsoidal vortex in a stratified ocean: survivability of the vortex in flow with vertical shear. *Izv. AN SSSR Phys. Atmos. Ocean* **27**, pp. 492–503.